Universidad Politécnica de Cartagena

VNIVERSITAT DE VALÈNCIA

Universidad Politécnica de Cartagena

Escuela Técnica Superior de Ingeniería de Telecomunicaciones

Investigations on Radio-Frequency Components and the Multipactor Phenomenon in High-Power Space Applications

Doctoral Thesis

Author

Manuel F. Jiménez Nogales

Supervisors

Dr. Alejandro Alvarez Melcón
Dr. Fernando Quesada Pereira
Dr. Benito Gimeno Martínez

Cartagena, España, 2012

It seems to be one of the fundamental features of nature that fundamental physical laws are described in terms of a mathematical theory of great beauty and power, needing quite a high standard of mathematics for one to understand it.

Paul Dirac (1902 - 1984)

Contents

List of Acronyms

BI-RME Boundary integral-resonant mode expansion

BPF Band-pass filter

DC Direct current

DUT Device under test

EM Electromagnetic

ESA European Space Agency

HPA High power amplifier

HPF High-pass filter

LNA Low noise amplifier

LPF Low-pass filter

PIC Particle-In-Cell

PRF Pulse repetition frequency

PW Pulse width

RBW Resolution bandwidth

RF Radio frequency

SA Spectrum analyser

SEY Secondary electron yield

SNR Signal to noise ratio

SWT Sweep time

TE Transverse electric

TM Transverse magnetic

TWTA Travelling wave tube amplifier

VBW Video bandwidth

Chapter 1

Introduction

This document is intended to give a description of the main research activities executed by the PhD candidate Manuel Jiménez Nogales. The present doctorate falls under the umbrella of the Networking/Partnering Initiative (NPI) program of the European Space Agency (ESA) and has been co-funded with the University of Cartagena, Spain. The PhD student joined the Information and Communications Technologies research department in September 2007 under the supervision of Professor A. Alvarez Melcón. He took a PhD Master on the subject of Integral Equation and Method of Moments techniques, and in September 2008 he joined the NPI in the topics of Multipactor and Radio frequency (RF)-breakdown phenomena. Since then, the student has combined academic stays at the University of Valencia, Spain and at ESA/ESTEC center in Noordwijk, The Netherlands. In Valencia, he studied RF-breakdown phenomena from a theoretical point of view at the Applied Physics department, under the supervision of Professor B. Gimeno Martínez. The student was introduced to multipactor testing on real RF components at the High Power RF Laboratory of the Payload System Division at ESA/ESTEC center, under the supervision of Mr. D. Raboso and Mr. C. Miquel-España.

The objective of this work is to study the electromagnetic radiation of charged particles within waveguides. The main motivations of this research are the prediction of the multipactor effect within waveguide components for space applications, and the study of the electromagnetic fields created by moving charges for particle accelerators.

The electromagnetic radiation of a charge particle as well as a charge distribution within a waveguide region or a resonator cavity has been extensively treated in the literature. Several authors have investigated the radiation of electron beams in metallic waveguides and cavities for the study of RF photo-injectors [1, 2]. Other classical problem related with this topic is the evaluation of the wake-fields generated by particles moving linearly at constant velocity [3, 4, 5, 6, 7, 8, 9, 10, 11, 12, 13, 14]. The study of the radiated fields left behind by a charged particle is particularly important because they influence the motion of the charged particles that follow them. The rigorous analysis of the wake-fields is a non-trivial issue, and critically depends on the geometry and materials of the accelerator structure. In most of the current models found in the technical literature, the particles move linearly at constant velocity [4, 5, 6, 7, 8, 9, 11, 12, 14].

Another physical phenomenon directly related with the radiation of electrons moving within an RF waveguide passive component is the multipactor effect. Multipactor discharge is a non-linear effect that may occur in high power microwave devices at very low pressures, especially in satellite subsystems [15, 16, 17, 18, 19, 20, 21, 22, 23, 24, 25] and particle accelerators [26, 27, 28, 29, 30, 31,

32, 33, 34, 35, 36, 37, 38]. However, the interaction of a multipactor discharge occurring within a realistic waveguide component has not been studied so far in detail.

Basically, multipactor is an electron avalanche in synchronism with the existing RF field caused by secondary emission multiplication on the device walls: primary electrons accelerated by the RF fields impact on a surface releasing a larger number of secondary electrons, which may in turn be accelerated by the RF fields striking successively against the other surface, then extracting more and more electrons, and so on. The discharge, which is normally undesired, can occur for a wide range of frequencies (from MHz to tens of GHz) and in a wide set of geometries. In microwave devices for space communications, its effects range from the signal degradation to the complete destruction of the component. In accelerating structures, multipactor causes serious problems during accelerator operation due to reflections, and can generate dielectric window breakdown on the vacuum side.

The starting point for the study of electromagnetic radiations in an enclosure scenario is the formulation of the electric and magnetic Green's function [39, 40, 41, 42, 43, 44]. In this sense, an expression for the dyadic Green's function for waveguide regions is derived in Chapter 2. The formulation is undertaken in the context of Modal Analysis of waveguides [45, 46, 47, 48]. The problem of multipactor is tackled in the following chapters. An introduction to the multipactor effect is given in Chapter 3, including a description of the phenomenon and a review of classical models. Chapter 4 reports the Thesis proposal for the analysis and prediction of multipactoring within waveguide components. The chapter can be divided into two parts: in the first one the multipactor experiments carried out at ESA/ESTEC laboratories are reported; the theory for the simulation of multipactor within RF components is explained in the second part of this chapter. Chapter 5 is devoted to the study of the radiation of travelling charges within waveguides for particle accelerators applications. Formulation details are given in Appendix, as well as a summary of publications contributed by the PhD candidate during his doctorate period.

Chapter 2

Radiation of a time-harmonic electric current within a microwave waveguide

2.1 Introduction

Maxwell's equations are a set of differential equations that describe the behaviour of electromagnetic fields in connexion with their sources. They form the basic laws that underlie Electromagnetism. Their solution for a given problem is a function of the boundary conditions at the surface of the structure. In this sense, it is well known that for a uniform, lossless waveguide region, the electromagnetic fields can be found using the modal function formalism [45, 46, 47, 49]. From a general point of view, modal analysis is the study of the system dynamics under vibrational excitation. Modal analysis relies on representing the solution of a system of linear equations in a vectorial space. The solution appears as the linear combination of its bases, known as modes. This method has been traditionally applied to Electromagnetism. Maxwell's equations are separated into transverse and longitudinal parts. The transverse part of the resulting equations can be expressed as a series of normal modes[46]. Transverse modes occur because of boundary conditions imposed on the electromagnetic fields by the lateral walls of the waveguide. Then, it is shown that the longitudinal part of the electromagnetic fields can be reduced to the well known transmission-line equations.

The dyadic Green's function is defined as the fields produced by a unit dipole within the structure under study [42]. The study of Green's function arising in electromagnetic problems is a primary subject extensively treated in the technical literature [39, 40, 41, 42, 43, 47]. Here we present a modal formulation of Green's functions for uniform, lossless waveguides.

2.2 Maxwell's equations

The behavior of electromagnetic fields in any arbitrary medium is governed by the well known Maxwell's equations. This set of equations describe how electric charges and currents act as sources for the electric and magnetic fields. Further on, it describes how a time varying electric field generates

a time varying magnetic field and vice versa:

$$\nabla \cdot \vec{\mathcal{D}}(\vec{r},t) = \rho(\vec{r},t) \qquad \text{(Gauss Law)} \tag{2.1a}$$

$$\nabla \cdot \vec{\mathcal{B}}(\vec{r},t) = 0 \qquad \text{(Gauss Law for Magnetism)} \tag{2.1b}$$

$$\nabla \times \vec{\mathcal{E}}(\vec{r},t) = -\frac{\partial \vec{\mathcal{B}}(\vec{r},t)}{\partial t} \qquad \text{(Maxwell-Faraday's Law)} \tag{2.1c}$$

$$\nabla \times \vec{\mathcal{H}}(\vec{r},t) = \frac{\partial \vec{\mathcal{D}}(\vec{r},t)}{\partial t} + \vec{\mathcal{J}}(\vec{r},t) \qquad \text{(Ampere's Law)} \tag{2.1d}$$

where $\vec{\mathcal{E}}$ and $\vec{\mathcal{H}}$ are the electric and magnetic field intensities in the time-domain, respectively; ρ stands for the charge density and $\vec{\mathcal{J}}$ for electric current density. The vector $\vec{r}$ indicates the position where the fields are calculated. Finally, $\vec{\mathcal{D}}$ and $\vec{\mathcal{B}}$ are the electric and magnetic flux densities, respectively, which characterize the medium where the field exists by means of the constitutive relationships:

$$\vec{\mathcal{D}}(\vec{r},t) = \varepsilon \vec{\mathcal{E}}(\vec{r},t) \tag{2.2a}$$

$$\vec{\mathcal{B}}(\vec{r},t) = \mu \vec{\mathcal{H}}(\vec{r},t) \tag{2.2b}$$

ε being the complex permittivity of the medium and μ the complex permeability of the medium. Matter is often classified according to these parameters. The complex permittivity and permeability of the medium are often expressed as a function of those quantities in free space, ε_0 and μ_0, in the following way:

$$\varepsilon = \varepsilon_r \varepsilon_0 \tag{2.3a}$$

$$\mu = \mu_r \mu_0 \tag{2.3b}$$

where ε_r is called the complex relative permittivity (or dielectric constant) of the medium, and μ_r the complex relative permeability of the medium; ε_0 and μ_0 are the vacuum permittivity and permeability, respectively. If only time-harmonic signals are considered, Fourier transformation (see Appendix B.1) allows to express the time-domain equations (2.1) into the frequency-domain as [49]:

$$\nabla \cdot \vec{D}(\vec{r},\omega) = \rho(\vec{r},\omega) \tag{2.4a}$$

$$\nabla \cdot \vec{B}(\vec{r},\omega) = 0 \tag{2.4b}$$

$$\nabla \times \vec{E}(\vec{r},\omega) = -i\omega \vec{B}(\vec{r},\omega) \tag{2.4c}$$

$$\nabla \times \vec{H}(\vec{r},\omega) = i\omega \vec{D}(\vec{r},\omega) + \vec{J}(\vec{r},\omega) \tag{2.4d}$$

i being the imaginary unit ($i = \sqrt{-1}$) and ω the angular frequency ($\omega = 2\pi f$). Equations (2.4) form the basic equations needed for determining complex electromagnetic fields in the presence of electric currents. Obviously, the constitutive relationships in the frequency-domain are:

$$\vec{D}(\vec{r},\omega) = \varepsilon \vec{E}(\vec{r},\omega) \tag{2.5a}$$

$$\vec{B}(\vec{r},\omega) = \mu \vec{H}(\vec{r},\omega) \tag{2.5b}$$

In the original Maxwell's equations (2.1) and (2.4) only electric current and electric charge densities are considered. The field sources are represented by ρ and $\vec{J}$, connected by the continuity equation:

$$\nabla \cdot \vec{J} + i\,\omega\,\rho = 0 \tag{2.6}$$

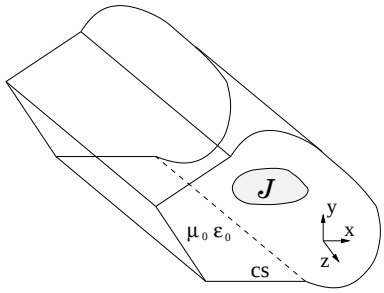

Figure 2.1: Waveguide with arbitrary cross-section CS.

In the above equations all fields are vector complex quantities, called phasors. The time dependence of the fields can always be recovered through the following standard relation between a sinusoidal function and the complex exponential function:

$$\vec{\mathcal{E}}(\vec{r},t) = \mathcal{R}e\left\{\vec{E}(\vec{r})\ e^{i\omega t}\right\} \tag{2.7}$$

2.3 Electromagnetic fields within a waveguide region

The following analysis is restricted to waveguide regions, in which vacuum medium is assumed and the geometry is easily decomposed into transverse and longitudinal components, as depicted in Fig. 2.1. In this sense, the operator ∇ and the position vector $\vec{r}$ can be expressed as $\nabla = \nabla_\perp + \frac{\partial}{\partial z}\hat{z}$ and $\vec{r} = \vec{r}_\perp + r_z\hat{z}$. The transversal and axial components of fields and sources will be studied separately too:

$$\vec{J} = \vec{J}_\perp + J_z\hat{z} \tag{2.8a}$$
$$\vec{E} = \vec{E}_\perp + E_z\hat{z} \tag{2.8b}$$
$$\vec{H} = \vec{H}_\perp + H_z\hat{z} \tag{2.8c}$$

In a waveguide region, the transverse components of the fields can be easily expressed in terms of transverse modal functions [46]. In consequence, the analysis will be greatly simplified by avoiding working with the longitudinal components of the fields. A standard vectorial analysis of (2.4) leads to two equations in which only transverse components of the fields are involved [47, 48, 49]. Such

operational procedure can be outlined in the next steps:

$$\nabla_\perp \vec{E}_\perp + \frac{\partial E_z}{\partial z} = \frac{\rho}{\varepsilon_0}$$
$$\nabla_\perp \vec{H}_\perp + \frac{\partial H_z}{\partial z} = 0$$
$$\nabla_\perp \times \vec{E}_\perp = -i\,\omega\,\mu_0\,H_z\,\hat{z}$$
$$\frac{\partial \vec{E}_\perp}{\partial z} - \nabla_\perp E_z = -i\,\omega\,\mu_0\,\vec{H}_\perp \times \hat{z}$$
$$\nabla_\perp \times \vec{H}_\perp = i\,\omega\,\varepsilon_0\,E_z\,\hat{z} + J_z\,\hat{z}$$
$$\frac{\partial \vec{H}_\perp}{\partial z} - \nabla_\perp H_z = -i\,\omega\,\varepsilon_0\,\hat{z} \times \vec{E}_\perp - \hat{z} \times \vec{J}_\perp$$

To finally obtain:

$$\frac{\partial \vec{E}_\perp}{\partial z} = -i\,\omega\,\mu_0\,\vec{H}_\perp \times \hat{z} + \frac{1}{i\,\omega\,\varepsilon_0}\nabla_\perp\left(\nabla_\perp \cdot \left(\vec{H}_\perp \times \hat{z}\right) - J_z\right) \tag{2.9a}$$
$$\frac{\partial \vec{H}_\perp}{\partial z} = -i\,\omega\,\varepsilon_0\,\hat{z} \times \vec{E}_\perp + \frac{1}{i\,\omega\,\mu_0}\nabla_\perp\left(\nabla_\perp \cdot \left(\hat{z} \times \vec{E}_\perp\right)\right) - \hat{z} \times \vec{J}_\perp \tag{2.9b}$$

At this point, it is interesting to continue the analysis omitting the sources ($\vec{J} = 0$):

$$\frac{\partial \vec{E}_\perp}{\partial z} = -i\omega\,\mu_0\,\vec{H}_\perp \times \hat{z} + \frac{1}{i\,\omega\,\varepsilon_0}\nabla_\perp\left(\nabla_\perp \cdot \left(\vec{H}_\perp \times \hat{z}\right)\right) \tag{2.10a}$$
$$\frac{\partial \vec{H}_\perp}{\partial z} = -i\omega\,\varepsilon_0\,\hat{z} \times \vec{E}_\perp + \frac{1}{i\,\omega\,\mu_0}\nabla_\perp\left(\nabla_\perp \cdot \left(\hat{z} \times \vec{E}_\perp\right)\right) \tag{2.10b}$$

and

$$i\,\omega\,\varepsilon_0\,\vec{E}_z = \nabla_\perp\left(\vec{H}_\perp \times \hat{z}\right) \tag{2.11a}$$
$$i\,\omega\,\mu_0\,\vec{H}_z = \nabla_\perp\left(\hat{z} \times \vec{H}_\perp\right) \tag{2.11b}$$

Here, the fields are described from their transverse components. A solution of (2.10) should obey the Helmholtz wave equation:

$$\nabla_\perp^2\phi + k_t^2\phi = 0 \tag{2.12}$$

Impossing boundary conditions at the contour of the waveguide, there are two possible families of solutions for the potential function ϕ, also known as modes of the waveguide: Transverse electric (TE) and Transverse magnetic (TM) modes. The potential functions are solutions of homogeneous Helmholtz equations, subject to the appropriate boundary conditions on the cross-section CS:

$$\nabla_\perp^2\,\phi_m + k_{t_m}^2\,\phi_m = 0 \tag{2.13a}$$
$$\phi_m^{TM}\big|_{CS} = 0 \tag{2.13b}$$
$$\left.\frac{\partial\,\phi_m^{TE}}{\partial\,n}\right|_{CS} = 0 \qquad \hat{n} \perp CS \tag{2.13c}$$

It is usually preferable to express the electromagnetic fields as a function of vector modal functions instead of scalar potentials ϕ. The relationship between both parameters is [46]:

$$\vec{e}_m^{\,TM}(\vec{r}_\perp) = -\nabla_\perp \phi_m^{TM} \tag{2.14a}$$

$$\vec{h}_m^{TM}(\vec{r}_\perp) = \hat{z} \times \vec{e}_m{}^{TM} \tag{2.14b}$$

$$\vec{e}_m^{\,TE}(\vec{r}_\perp) = \hat{z} \times \nabla_\perp \phi_m^{TE} \tag{2.14c}$$

$$\vec{h}_m^{TE}(\vec{r}_\perp) = \hat{z} \times \vec{e}_m^{\,TE} \tag{2.14d}$$

where $\vec{e}_m$ and $\vec{h}_m$ stand for electric and magnetic modal vectors. Vector modal functions are dependent only on the cross-section and they form a complete orthonormal set of functions inside the waveguide [46]:

$$\iint_{CS} \vec{e}_m \cdot \vec{e}_n^{\,*}\, d\,S = \iint_{CS} \vec{h}_m \cdot \vec{h}_n^{\,*}\, d\,S = \delta_{m,n} \tag{2.15}$$

where $\delta_{m,n}$ is the Kronecker delta function (see Appendix B.2) and the superscript $*$ denotes complex conjugate. Because of the orthonormal property of vector modal functions, any function can be expressed as a linear combination of the complete set. In consequence, we can express the electric and magnetic fields inside the waveguide as a series expansions of vector modal functions:

$$\vec{E}_\perp(\vec{r}) = \sum_m V_m(z)\vec{e}_m(\vec{r}_\perp) \tag{2.16a}$$

$$\vec{H}_\perp(\vec{r}) = \sum_m I_m(z)\vec{h}_m(\vec{r}_\perp) \tag{2.16b}$$

$$E_z(\vec{r}) = \frac{1}{i\,\omega\,\varepsilon_0} \sum_m I_m^{TM}(z) k_{t_m}^{2_{TM}} \phi_m^{TM}(\vec{r}_\perp) \tag{2.16c}$$

$$H_z(\vec{r}) = \frac{1}{i\,\omega\,\mu_0} \sum_m V_m^{TE}(z) k_{t_m}^{2_{TE}} \phi_m^{TE}(\vec{r}_\perp) \tag{2.16d}$$

the amplitudes V_m and I_m being the modal equivalent voltage and current. On the other hand, the transverse wavenumber k_{t_m} satisfies the dispersion relationship $k_0^2 = k_{t_m}^2 + k_{z_m}^2$, where $k_0 = \omega\sqrt{\mu_0\varepsilon_0}$ is the free space wavenumber and k_{z_m} the propagation factor. The modal amplitudes can be found applying (2.15) to (2.16):

$$V_m(z) = \iint_{CS} \vec{E}_\perp(\vec{r})\, \vec{e}_m{}^*(\vec{r}_\perp)\, d\,S \tag{2.17a}$$

$$I_m(z) = \iint_{CS} \vec{H}_\perp(\vec{r})\, \vec{h}_m^*(\vec{r}_\perp)\, d\,S \tag{2.17b}$$

The solution of V_m and I_m satisfies the following expressions:

$$\frac{dV_m}{dz} = -i\,Z_m\,k_{z_m}\,I_m \tag{2.18a}$$

$$\frac{dI_m}{dz} = -i\,Y_m\,k_{z_m}\,V_m \tag{2.18b}$$

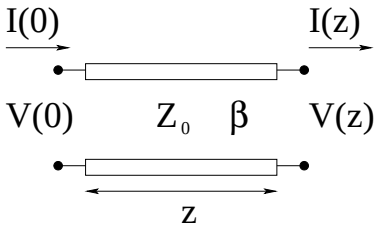

Figure 2.2: Transmission-line section of length z. The voltage and current at the output of the line are related with the input voltage and current by means of (2.21). $\beta \equiv k_{z_m}$

Or, equivalently

$$\frac{d^2 V_m}{dz^2} + k_{z_m}^2 \, V_m \; = \; 0 \tag{2.19a}$$

$$\frac{d^2 I_m}{dz^2} + k_{z_m}^2 \, I_m \; = \; 0 \tag{2.19b}$$

These expressions are known as the Telegrapher's equations. They are equivalent to the relations followed by the electric voltage and current in a transmission-line section. It means that modes propagate along a waveguide as electric voltage and current do in a transmission-line (see Fig. 2.2). At this point, it is necessary to introduce the modal characteristic impedance Z_m, which is the ratio of the amplitudes of a single pair of voltage and current waves propagating along a transmission-line in the absence of reflections (see Appendix A):

$$Z_m^{TE} \; = \; \frac{\omega \, \mu_0}{k_{z_m}} \tag{2.20a}$$

$$Z_m^{TM} \; = \; \frac{k_{z_m}}{\omega \, \varepsilon_0} \tag{2.20b}$$

The characteristic admittance Y_m is the inverse of the impedance $Y_m = 1/Z_m$. The solution of wave equations (2.19) is a plane wave with equal propagation speed in the forward and reverse directions:

$$V_m(z) \;\; = \;\; V_m^+ \; e^{-i \, k_{z_m} \, z} + V_m^- \; e^{+i \, k_{z_m} \, z} \tag{2.21a}$$

$$I_m(z) \;\; = \;\; I_m^+ \; e^{-i \, k_{z_m} \, z} - I_m^- \; e^{+i \, k_{z_m} \, z} \tag{2.21b}$$

where the paralelism between the modal amplitudes and circuital voltage and currents is more evident. This fact leads to the well known equivalent circuit per unit length of a transmission-line shown in Fig. 2.3.

A similar analysis is now derived for the case when field sources $\vec{J} \neq 0$ are considered. Starting from (2.9), we can write

$$\frac{\partial \vec{E}_\perp}{\partial z} \; = \; -i \, \omega \, \mu_0 \, \vec{H}_\perp \times \hat{z} + \frac{1}{i \, \omega \, \varepsilon_0} \nabla_\perp \left(\nabla_\perp \cdot \left(\vec{H}_\perp \times \hat{z} \right) \right) \; + \; \vec{M}_\perp \times \hat{z} \tag{2.22a}$$

$$\frac{\partial \vec{H}_\perp}{\partial z} \; = \; -i \, \omega \, \varepsilon_0 \, \hat{z} \times \vec{E}_\perp \; + \; \frac{1}{i \, \omega \, \mu_0} \nabla_\perp \left(\nabla_\perp \cdot \left(\hat{z} \times \vec{E}_\perp \right) \right) \; + \; \hat{z} \times \vec{J}_\perp \tag{2.22b}$$

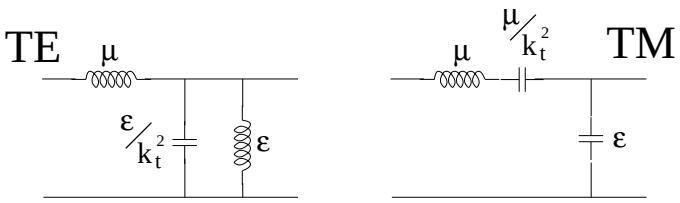

Figure 2.3: Equivalent circuits for the TE and TM modes of a lossless waveguide in the absence of field sources.

where the ficticious magnetic current density $\vec{M}$ has been introduced:

$$\vec{M}_\perp \;=\; -\frac{1}{i\,\omega\,\varepsilon_0}\,\nabla_\perp\,J_z \tag{2.23}$$

In the context of modal analysis, it is preferable to work with a transverse magnetic current density $M_\perp$ instead of a longitudinal electric current density J_z. The transverse magnetic current representation simplifies the analysis of the problem since it allows the direct representation of the source as a modal series. From the orthonormality property of vector modal functions (2.15), it is derived that the field sources can be expressed too as a linear combination of such functions:

$$\vec{E}_\perp(\vec{r}) \;=\; \sum_m V_m(z)\,\vec{e}_m(\vec{r}_\perp) \tag{2.24a}$$

$$\vec{H}_\perp(\vec{r}) \;=\; \sum_m I_m(z)\,\vec{h}_m(\vec{r}_\perp) \tag{2.24b}$$

$$\vec{J}_\perp(\vec{r}) \;=\; \sum_m \chi_m(z)\,\vec{e}_m(\vec{r}_\perp) \tag{2.24c}$$

$$\vec{M}_\perp(\vec{r}) \;=\; \sum_m \xi_m(z)\,\vec{h}_m(\vec{r}_\perp) \tag{2.24d}$$

In the last expressions modal amplitudes χ_m and ξ_m for the field sources have been introduced. These modal amplitudes obviously satisfy the following expressions because of the orthonormality property of vector modal functions:

$$V_m(z) \;=\; \iint_{CS} \vec{E}_\perp(\vec{r})\,\vec{e}_m{}^*(\vec{r}_\perp)\;d\;S \tag{2.25a}$$

$$I_m(z) \;=\; \iint_{CS} \vec{H}_\perp(\vec{r})\,\vec{h}_m^*(\vec{r}_\perp)\;d\;S \tag{2.25b}$$

$$\chi_m(z) \;=\; \iint_{CS} \vec{J}_\perp(\vec{r})\,\vec{e}_m{}^*(\vec{r}_\perp)\;d\;S \tag{2.25c}$$

$$\xi_m(z) \;=\; \iint_{CS} \vec{M}_\perp(\vec{r})\,\vec{h}_m^*(\vec{r}_\perp)\;d\;S \tag{2.25d}$$

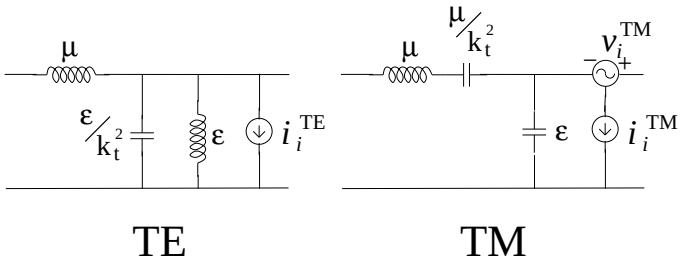

Figure 2.4: Equivalent circuits for the TE and TM modes of a lossless waveguide in the presence of field sources.

Following the same procedure as in the first case, the next equations can be derived:

$$\frac{dV_m^{TM}}{dz} = -i\,Z_m\,k_{z_m}\,I_m^{TM} + \xi_m^{TM} \tag{2.26a}$$

$$\frac{dI_m^{TM}}{dz} = -i\,Y_m\,k_{z_m}\,V_m^{TM} + \chi_m^{TM} \tag{2.26b}$$

$$\frac{dV_m^{TE}}{dz} = -i\,Z_m\,k_{z_m}\,I_m^{TE} \tag{2.26c}$$

$$\frac{dI_m^{TE}}{dz} = -i\,Y_m\,k_{z_m}\,V_m^{TE} + \chi_m^{TE} \tag{2.26d}$$

This last system of differential equations is similar to the Telegrapher's equations, but modified by the action of field sources. The equivalen circuit of these expressions is shown in Fig. 2.4, where the amplitude of the voltage and current generators is:

$$i_m^{TE} = -\chi_m^{TE} \tag{2.27a}$$

$$i_m^{TM} = -\chi_m^{TM} \tag{2.27b}$$

$$v_m^{TM} = -\xi_m^{TM} \tag{2.27c}$$

The presence of sources is represented by the voltage and current generators in the equivalent circuit. The combination of the circuits shown in Fig. 2.3 and 2.4 leads to a mixed representation of transmission-line section with circuital generators, depicted in Fig. 2.5. In this figure, the presence of a source within the waveguide is represented by circuital generators into the transmission lines model at the longitudinal point where the source is located.

2.4 Green's function of a uniform waveguide

The evaluation of Green's functions is a classical problem of the Electromagnetic theory, which has been extensively treated in the technical literature [39, 41, 42, 46, 47, 50]. The dyadic Green's functions of an infinite waveguide with uniform cross-section represents the electric and magnetic fields radiated by a time-harmonic unit impulse current source placed in an arbitrary location given by the vector position $\vec{r}\,'$. Hence, the Green's function appears as the impulse response of the waveguide

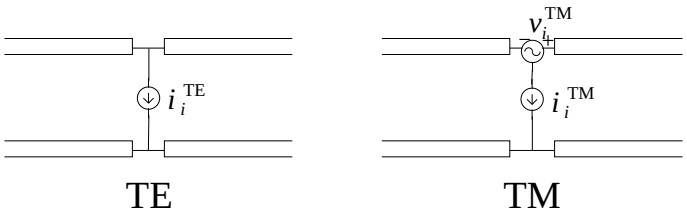

Figure 2.5: Transmission-lines model for the TE and TM modes of a lossless waveguide in the presence of field sources.

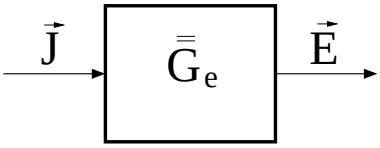

Figure 2.6: Block diagram of the Green's function for the electric field.

system to electromagnetic sources, as depicted in Fig. 2.6. The electromagnetic fields within such system are derived by the convolution of the Green's function with the sources:

$$\vec{E}(\vec{r}) \;=\; \int_V \overline{\overline{G}}_e(\vec{r},\vec{r}\,') \cdot \vec{J}(\vec{r}\,')dV' \tag{2.28a}$$

$$\vec{H}(\vec{r}) \;=\; \int_V \overline{\overline{G}}_h(\vec{r},\vec{r}\,') \cdot \vec{J}(\vec{r}\,')dV' \tag{2.28b}$$

where $\overline{\overline{G}}_e$ and $\overline{\overline{G}}_h$ are the Green's function for electric and magnetic fields, respectively; the integration volume V includes the waveguide region. The source element $\vec{J}$ can be oriented in any direction. This allows to study non-uniform current problems, like the multipactor discharges analyzed in Sec 4.5. We can deduce the Green's function studying impulse sources oriented in the transverse and longitudinal directions. The different components of the Green's function thus deduced will be finally combined to obtain the response of the system to an aribitrarily oriented current density, it is:

$$\overline{\overline{G}}_e(\vec{r},\vec{r}\,') \cdot \hat{a} \;=\; \vec{E}(\vec{r})\Big|_{\vec{J}(\vec{r}\,')=\delta(\vec{r}\,')\hat{a}} \tag{2.29a}$$

$$\overline{\overline{G}}_h(\vec{r},\vec{r}\,') \cdot \hat{a} \;=\; \vec{H}(\vec{r})\Big|_{\vec{J}(\vec{r}\,')=\delta(\vec{r}\,')\hat{a}} \tag{2.29b}$$

where the unitary vector $\hat{a}$ indicates any direction and δ stands for Dirac delta. A description of Dirac delta is given in Appendix B.2. The analysis starts with an unitary electric current oriented in a transverse direction $w = \{x, y\}$:

$$\vec{J}(\vec{r},\vec{r}\,') \;=\; 1\;\delta(\vec{r}_\perp - \vec{r}_\perp{}')\,\delta(z-z')\,\hat{w} \tag{2.30}$$

This transverse current can be expressed in terms of the normalized electric and magnetic TE and TM vector modal functions following (2.24c). The electric current modal amplitudes χ in this series expression are found using the current element (2.30) into the integral (2.25c), what gives:

$$\chi_m^{(w)}(z) \;=\; e^*_{m_w}(\vec{r}_\perp{}')\,\delta(z-z') \tag{2.31}$$

where the superscript (w) indicates a transverse oriented source. Such electric current modal amplitudes, and assuming $\xi^{(w)} = 0$ due to the absence of magnetic currents, modify the set of equations (2.26), resulting into:

$$\frac{dV_m^{(w)}(z,\vec{r}')}{dz} \;=\; -i\,Z_m\,k_{z_m}\,I_m^{(w)}(z,\vec{r}') \tag{2.32a}$$

$$\frac{dI_m^{(w)}(z,\vec{r}')}{dz} \;=\; -i\,Y_m\,k_{z_m}\,V_m^{(w)}(z,\vec{r}') \;+\; e^*_{m_w}(\vec{r}_\perp{}')\,\delta(z-z') \tag{2.32b}$$

The solution of this system of equations is:

$$V_m^{(w)}(z,\vec{r}') \;=\; -\frac{1}{2}\,Z_m\,e^*_{m_w}(\vec{r}_\perp{}')\;\; e^{-ik_{z_m}|z-z'|} \tag{2.33a}$$

$$I_m^{(w)}(z,\vec{r}') \;=\; -\frac{1}{2}\,u(z-z')\,e^*_{m_w}(\vec{r}_\perp{}')\;\; e^{-ik_{z_m}|z-z'|} \tag{2.33b}$$

where u denotes the Heaviside step function, analyzed in Appendix B.2. Infinite waveguide has been assumed in (2.33), as can be noted by the absence of a reflected wave in the negative z-direction. An expression for the electromagnetic fields in modal expansion is directly found after introducing (2.33) into (2.16):

$$\vec{E}_\perp^{(w)}(\vec{r},\vec{r}',\omega) \;=\; -\frac{1}{2}\sum_m Z_m\,e_{m_w}(\vec{r}_\perp)\,\vec{e}_m{}^*(\vec{r}_\perp{}')\;\; e^{-ik_{z_m}|z-z'|} \tag{2.34a}$$

$$\vec{H}_\perp^{(w)}(\vec{r},\vec{r}',\omega) \;=\; -\frac{u(z-z')}{2}\sum_m e_{m_w}(\vec{r}_\perp)\,\vec{h}_m{}^*(\vec{r}_\perp{}')\;\; e^{-ik_{z_m}|z-z'|} \tag{2.34b}$$

$$E_z^{(w)}(\vec{r},\vec{r}',\omega) \;=\; -\frac{u(z-z')}{i\,2\,\omega\,\varepsilon_0}\sum_m k_{t_m}^{2_{TM}}\,e_{m_w}(\vec{r}_\perp)\,\phi_m^{*TM}(\vec{r}_\perp{}')\;\; e^{-ik_{z_m}|z-z'|} \tag{2.34c}$$

$$H_z^{(w)}(\vec{r},\vec{r}',\omega) \;=\; -\frac{1}{i\,2\,\omega\,\mu_0}\sum_m Z_m^{TE}\,k_{t_m}^{2_{TE}}\vec{e}_m(\vec{r}_\perp)\,\phi_m^{*TE}(\vec{r}_\perp{}')\;\; e^{-ik_{z_m}|z-z'|} \tag{2.34d}$$

The case of an unit impulse excitation in the longitudinal direction is analyzed next. Lets consider a elementary electric current like:

$$\vec{J} \;=\; 1\;\delta(\vec{r}_\perp-\vec{r}_\perp{}')\,\delta(z-z')\,\hat{z} \tag{2.35}$$

In this case, $\chi = 0$ because there is no transverse electric current. It is necessary to make use of the transverse magnetic current definition (2.23). Thus, the modal amplitudes for the magnetic current are:

$$\xi_m(z) \;=\; -\frac{k_{t_m}^2}{i\,\omega\,\varepsilon_0}\,\phi_m^{*TM}(\vec{r}_\perp{}')\,\delta(z-z') \tag{2.36}$$

Note that in the last expression only TM modes are involved. This means that a longitudinal source only excites the TM modes of the waveguide. This time, the system of equations (2.26) simplifies to:

$$\frac{dV_m^{TM}}{dz}(\vec{r},\vec{r}') = -i\,Z_m\,k_{z_m}\,I_m^{TM}(\vec{r},\vec{r}') - \frac{k_{t_m}^2}{i\,\omega\,\varepsilon_0}\,\phi_m^{*TM}(\vec{r}_\perp{}')\,\delta(z-z') \tag{2.37a}$$

$$\frac{dI_m^{TM}}{dz}(\vec{r},\vec{r}') = -i\,Y_m\,k_{z_m}\,V_m^{TM}(\vec{r},\vec{r}') \tag{2.37b}$$

$$\tag{2.37c}$$

whose solution is given by

$$V_m^{(z)}(z,z') = -\frac{1}{2}\,u(z-z')\,\xi_m^{TM}(z)\;\; e^{-ik_{z_m}|z-z'|} \tag{2.38a}$$

$$I_m^{(z)}(z,z') = -\frac{1}{2}\,Y_m^{TM}\,\xi_m^{TM}(z)\;\; e^{-ik_{z_m}|z-z'|} \tag{2.38b}$$

This time, the superscript (z) denotes a lengthwise oriented source. Infinite waveguide is also assumed in this solution, as in (2.33) for transverse sources. These modal amplitudes lead to the following electromagnetic fields:

$$\vec{E}_{\perp_m}^{(z)} = -\frac{1}{2}\,u(z-z')\sum_m \vec{e}_m(\vec{r}_\perp)\,e_{m_z}^{*TM}(\vec{r}_\perp{}')\;\; e^{-ik_{z_m}|z-z'|} \tag{2.39a}$$

$$\vec{H}_{\perp_m}^{(z)} = -\frac{1}{2}\sum_m Y_m^{TM}\,\vec{h}_m(\vec{r}_\perp)\,e_{m_z}^{*TM}(\vec{r}_\perp{}')\;\; e^{-ik_{z_m}|z-z'|} \tag{2.39b}$$

$$E_z^{(z)} = -\frac{1}{i\,2\,\omega\,\varepsilon_0}\sum_m k_{t_m}^2\,\vec{e}_{m_z}^{TM}(\vec{r}_\perp)\,\phi_m^{*TM}(\vec{r}_\perp{}')\;\; e^{-ik_{z_m}|z-z'|} - \frac{1}{i\,2\,\omega\,\varepsilon_0}\,\delta(\vec{r}_\perp-\vec{r}_\perp{}') \tag{2.39c}$$

$$H_z^{(z)} = 0 \tag{2.39d}$$

At this point, usign the following notation for the dyadic Green's function:

$$\begin{aligned}\overline{\overline{G}}_e =& G_{e_{xx}}\hat{x}\hat{x} + G_{e_{xy}}\hat{x}\hat{y} + G_{e_{xz}}\hat{x}\hat{z} + G_{e_{yx}}\hat{y}\hat{x} + G_{e_{yy}}\hat{y}\hat{y} + G_{e_{yz}}\hat{y}\hat{z} \\ &+ G_{e_{zx}}\hat{z}\hat{x} + G_{e_{zy}}\hat{z}\hat{y} + G_{e_{zz}}\hat{z}\hat{z}\end{aligned} \tag{2.40a}$$

$$\begin{aligned}\overline{\overline{G}}_h =& G_{h_{xx}}\hat{x}\hat{x} + G_{h_{xy}}\hat{x}\hat{y} + G_{h_{xz}}\hat{x}\hat{z} + G_{h_{yx}}\hat{y}\hat{x} + G_{h_{yy}}\hat{y}\hat{y} + G_{h_{yz}}\hat{y}\hat{z} \\ &+ G_{h_{zx}}\hat{z}\hat{x} + G_{h_{zy}}\hat{z}\hat{y} + G_{h_{zz}}\hat{z}\hat{z}\end{aligned} \tag{2.40b}$$

and from the definition of the Green's function as an impulse response (2.29), we can write:

$$G_{e_{xx}}(\vec{r},\vec{r}') = -\frac{1}{2}\sum_m Z_m\, e_{m_x}(\vec{r}_\perp)\, {e_{m_x}}^*(\vec{r}_\perp{}')\ e^{-i\,k_{z_m}\,|z-z'|} \tag{2.41a}$$

$$G_{e_{xy}}(\vec{r},\vec{r}') = -\frac{1}{2}\sum_m Z_m\, e_{m_x}(\vec{r}_\perp)\, {e_{m_y}}^*(\vec{r}_\perp{}')\ e^{-i\,k_{z_m}\,|z-z'|} \tag{2.41b}$$

$$G_{e_{xz}}(\vec{r},\vec{r}') = -\frac{u(z-z')}{2}\sum_m e^{TM}_{m_x}(\vec{r}_\perp)\, {e_{m_z}}^{*TM}(\vec{r}_\perp{}')\ e^{-i\,k_{z_m}\,|z-z'|} \tag{2.41c}$$

$$G_{e_{yx}}(\vec{r},\vec{r}') = -\frac{1}{2}\sum_m Z_m\, e_{m_y}(\vec{r}_\perp)\, {e_{m_x}}^*(\vec{r}_\perp{}')\ e^{-i\,k_{z_m}\,|z-z'|} \tag{2.41d}$$

$$G_{e_{yy}}(\vec{r},\vec{r}') = -\frac{1}{2}\sum_m Z_m\, e_{m_y}(\vec{r}_\perp)\, {e_{m_y}}^*(\vec{r}_\perp{}')\ e^{-i\,k_{z_m}\,|z-z'|} \tag{2.41e}$$

$$G_{e_{yz}}(\vec{r},\vec{r}') = -\frac{u(z-z')}{2}\sum_m e^{TM}_{m_y}(\vec{r}_\perp)\, {e_{m_z}}^{*TM}(\vec{r}_\perp{}')\ e^{-i\,k_{z_m}\,|z-z'|} \tag{2.41f}$$

$$G_{e_{zx}}(\vec{r},\vec{r}') = -\frac{u(z-z')}{2}\sum_m e^{TM}_{m_x}(\vec{r}_\perp)\, {e_{m_z}}^{*TM}(\vec{r}_\perp{}')\ e^{-i\,k_{z_m}\,|z-z'|} \tag{2.41g}$$

$$G_{e_{zy}}(\vec{r},\vec{r}') = -\frac{u(z-z')}{2}\sum_m e^{TM}_{m_y}(\vec{r}_\perp)\, {e_{m_z}}^{*TM}(\vec{r}_\perp{}')\ e^{-i\,k_{z_m}\,|z-z'|} \tag{2.41h}$$

$$G_{e_{zz}}(\vec{r},\vec{r}') = -\frac{1}{2}\sum_m Y^{TM}_m\, e^{TM}_{m_z}(\vec{r}_\perp)\, {e_{m_z}}^{*TM}(\vec{r}_\perp{}')\ e^{-i\,k_{z_m}\,|z-z'|} \tag{2.41i}$$

Moreover, the intrinsic singularity of the electric field at the source position [42] makes necessary to add a last term to $\overline{\overline{G}}_e$, thus resulting:

$$\overline{\overline{G}}_e^{\,\text{Total}} = \overline{\overline{G}}_e - \frac{\delta(\vec{r}-\vec{r}')}{i\,\omega\,\varepsilon_0} \tag{2.42}$$

Finally, the elements of the magnetic field Green's function are:

$$G_{h_{xx}}(\vec{r},\vec{r}') = -\frac{u(z-z')}{2}\sum_m e_{m_x}(\vec{r}_\perp)\, h^*_{m_x}(\vec{r}_\perp{}')\ e^{-i\,k_{z_m}\,|z-z'|} \tag{2.43a}$$

$$G_{h_{xy}}(\vec{r},\vec{r}') = -\frac{u(z-z')}{2}\sum_m e_{m_x}(\vec{r}_\perp)\, h^*_{m_y}(\vec{r}_\perp{}')\ e^{-i\,k_{z_m}\,|z-z'|} \tag{2.43b}$$

$$G_{h_{xz}}(\vec{r},\vec{r}') = -\frac{1}{2}\sum_m Z_m^{TE}\, e^{TE}_{m_x}(\vec{r}_\perp)\, h^{*TE}_{m_z}(\vec{r}_\perp{}')\ e^{-i\,k_{z_m}\,|z-z'|} \tag{2.43c}$$

$$G_{h_{yx}}(\vec{r},\vec{r}') = -\frac{u(z-z')}{2}\sum_m e_{m_y}(\vec{r}_\perp)\, h^*_{m_x}(\vec{r}_\perp{}')\ e^{-i\,k_{z_m}\,|z-z'|} \tag{2.43d}$$

$$G_{h_{yy}}(\vec{r},\vec{r}') = -\frac{u(z-z')}{2}\sum_m e_{m_y}(\vec{r}_\perp)\, h^*_{m_y}(\vec{r}_\perp{}')\ e^{-i\,k_{z_m}\,|z-z'|} \tag{2.43e}$$

$$G_{h_{yz}}(\vec{r},\vec{r}') = -\frac{1}{2}\sum_m Z_m^{TE}\, e^{TE}_{m_y}(\vec{r}_\perp)\, h^{*TE}_{m_z}(\vec{r}_\perp{}')\ e^{-i\,k_{z_m}\,|z-z'|} \tag{2.43f}$$

$$G_{h_{zx}}(\vec{r},\vec{r}') = -\frac{1}{2}\sum_m Y_m^{TE}\, e^{TE}_{m_z}(\vec{r}_\perp)\, h^{*TE}_{m_x}(\vec{r}_\perp{}')\ e^{-i\,k_{z_m}\,|z-z'|} \tag{2.43g}$$

$$G_{h_{zy}}(\vec{r},\vec{r}') = -\frac{1}{2}\sum_m Y_m^{TE}\, e^{TE}_{m_z}(\vec{r}_\perp)\, h^{*TE}_{m_y}(\vec{r}_\perp{}')\ e^{-i\,k_{z_m}\,|z-z'|} \tag{2.43h}$$

$$G_{h_{zz}}(\vec{r},\vec{r}') = 0 \tag{2.43i}$$

Chapter 3

Multipactor Basics

3.1 Introduction

Multipactor discharges consist of electron multipaction on one or more material surfaces in resonance with an alternating electric field. The discharge is sustained by electron multiplication from secondary electron emission. Multipactor discharges have many detrimental effects on high-power RF systems operating in vacuum conditions, like the communication systems embeded in satellites and spacecrafts. These systems are difficult or even impossible to repair after launch. Multipactor generates excess heat, which can lead to melting, cracking, outgassing and damage of temperature-sensitive components. Moreover, the discharges change the impedance of transmission lines. This later effect detunes the RF circuit, what leads to a decrease of the transmitted power and an increase, in the same proportion, of the reflected power to the RF source. In extreme multipactor conditions the component might be partially destroyed.

Certain conditions on the RF signal and the geometry of microwave components must be fulfilled in order to have the electron multipaction above mentioned [15, 16]. First, there must be synchronism between the electron impacts and the alternating field. Second, the number of electrons involved in the multipaction process has to be increased at each new impact to generate a significant discharge. The first condition is a function of the RF frequency and amplitude, as well as the gap size the electrons cross in their path between successive impacts. On the other hand, for the electron generation, the secondary emission coefficient of the component walls must be greater than unity for the impact energies of most electrons.

Microwave components for operating in space are designed to avoid multipactor processes, or at least minimize them. In this sense, susceptibility charts give a correct estimation about frequency, power and gap size for different materials [15, 51, 52]. Susceptibility charts are based on the parallel plates theory [15, 16, 53]. They have been experimentally verified using rectangular waveguides, which can be approached to the parallel plates geometry under certain excitations [52]. The use of different techniques is still necessary for the satisfactory design of many RF components and more elaborate geometries. It is common to use computer simulations of electron tracking, but testing of prototypes on an RF laboratory is still required nowadays. On the other hand, it is worth to mention multipactor prevention techniques based on DC biasing and surface treatments. DC biasing involves suppressing the electron motion across a gap by applying a large DC electric field bias between

the electrodes [34]. Finally, surface roughening can be used to lower the secondary emission yield [54]. The reabsorption probability of released electrons is increased in the vicinity of peaks on a rough surface. Unfortunately, this technique presents some drawbacks, such as the degradation of the surface treatment with exposure time and the increment of transmission losses on the device [55].

3.2 Secondary electron emission

When an electron impacts a surface, it is possible for this electron to cause the emission of more electrons from the surface, called secondary electrons. Secondary emission depends of the primary electron energy, impact angle, and the surface material [16, 52, 56].

The most important aspect of secondary electron emission in regards to multipactor discharges is the Secondary electron yield (SEY) or secondary electron coefficient δ. This parameter represents an average number of secondary electrons emitted as a function of the energy of the primary electron impacting on the surface. The SEY function follows a curve similar to the one shown in Fig. 3.1 for most of materials. The first and second crossover points (E_1 and E_2 in the plot, respectively) delimit the energy interval for which the SEY is greater than unity. This interval defines the band of energy sensitive to multipactor. Clearly, the impact energies must focus in this range to produce a rising of the multipacting electron population. The threshold primary energy E_0 represents the minimum impact energy necessary for the emission of secondary electrons; primary electrons hitting below this threshold bounce back due to electric repulsion or are absorbed by the material. All these parameters, as well as the maximum SEY $\delta(E_m) = \delta_{max}$, vary for different materials (see Table 3.1). A portion of the electrons emitted from a surface after the incidence of primaries consists of primary electrons themselves, which are either elastically or inelastically reflected instead of being absorbed.

On the other hand, the emission angle of secondary electrons follows a distribution similar to the cosine distribution with respect to the normal to the surface, regardless of the incidence angle of the primary electron.

Material	E_1 (eV)	E_2 (eV)	E_m (eV)	δ_{max}
Aluminium	30	5000	805	2.98
Silver	30	5000	165	2.22
Gold	150	4000	1000	1.79

Table 3.1: Secondary emission characteristics for some materials.

3.3 Parallel Plates Theory

The motion of electrons in vacuum due to an electromagnetic field is governed by the Lorentz force. The influence of the magnetic force can be neglected for non-relativistic electrons, because its intensity is around c times less than the electric force (c meaning the speed of light in vacuum). Thus, in a simple model the problem is reduced to one dimension, since there are no significant transverse forces. The classical theory of multipactor follows this assumption in the well-known parallel plates multipactor theory [15, 16, 23, 56].

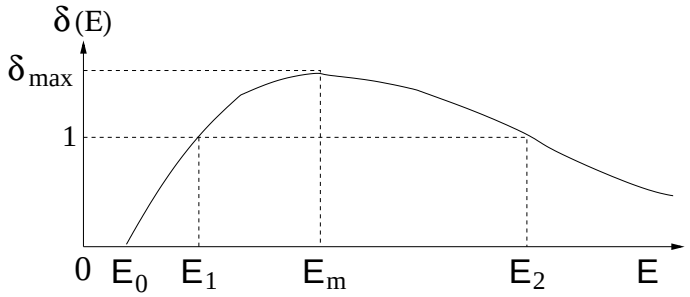

Figure 3.1: Secondary emission yield and main characteristics.

Classical multipactor theory and formulation is based on the parallel plates problem [15, 16, 56]. In this scenario there is an RF single carrier applied to the region between two conducting parallel surfaces (see Fig. 3.2(a)). The walls are considered as infinite planes compared with the gap d and vacuum condition is assumed between the plates. The electric field is:

$$E_y(t) \;=\; \frac{V_{RF}}{d}\cos(\omega\, t) \tag{3.1}$$

where V_{RF} is the electric voltage applied between plates and $\omega = 2\pi f_{RF} = 2\pi/T$ is the angular frequency, T being the period of the signal. When an electron gets into the vacuum region, it will eventually hit a plate. The effects of such collision depend on the impact energy as well as other parameters. If the energy of the impact is very low, the particle will be absorbed by the wall. On the other hand, if the energy is very high, there are two possibilities: the particle bounces or penetrates into the wall. Finally, with the appropriate energy, one or more electrons are released from the conducting surface. The released electrons are given different energy values as a consequence of the impact. It results in different velocities of launching. The simple parallel plates model considers only one particle, which concetrates all the charge and mass of such electrons. This electron is launched into the gap region with initial velocity v_{e0} (depending on the SEY), as seen in Fig. 3.2(b). Moreover, released electrons spread in different trajectories following the cosine distribution; the trajectory given to the electron in the present model is the perpendicular to the surface (it is $\hat{y}$) because this is the only one of interest in an infinite plates scenario. The electron will be accelerated and decelerated according to the sinusoidal electric field until it hits a wall, thus repeating the situation of the first impact (see Fig. 3.2(c)). Having secondary electrons is more probable for certain values of impact time and velocity. When such circumstances repeat, the population of released electrons increases and the multipaction becomes a discharge.

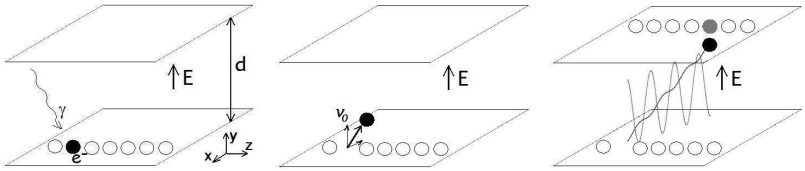

(a) An electron hits a wall. (b) An electron is released from the wall as a consequence of the impact. (c) The electron is trapped in the RF field and, eventually, hits the wall releasing a secondary electron.

Figure 3.2: Parallel plates multipactor ignition process.

The conditions that lead an electron to multipactoring are derived next. When an electron moves in an external electromagnetic field the following two laws apply:

$$\vec{F} = e\left(\vec{E} + \vec{v_e} \times \vec{B}\right) \quad \text{(Lorentz's force Law)} \tag{3.2a}$$

$$\vec{F} = m\,\vec{a} = m\,\frac{d\,\vec{v_e}}{d\,t} \quad \text{(Newton's second Law)} \tag{3.2b}$$

where e and m_e stand for the charge and mass of the electron. For the particular case of motion in the y direction and neglecting the influence of the magnetic field, these expressions simplify to

$$\frac{d\,v_e(t)}{d\,t} = \frac{d^2\,y(t)}{d\,t^2} = \frac{e\,E_y}{m_e} \tag{3.3}$$

We are going to apply this equation to a single electron released from $y = 0$ at $t = t_0$, with initial velocity v_{e0}. The analytical solution of the motion equation is easily found by integration:

$$v_e(t) = v_{e0} + K\Big[\sin(\omega\,t) - \sin(\omega\,t_0)\Big] \tag{3.4a}$$

$$y(t) = v_{e0}(t - t_0) + \frac{K}{\omega}\Big[-\cos(\omega\,t) + \cos(\omega\,t_0) - \omega(t - t_0)\sin(\omega\,t_0)\Big] \tag{3.4b}$$

where the electric field given in eq. (3.1) has been used. The constant K is

$$K = \frac{e\,V_{RF}}{m_e\,\omega\,d} \tag{3.5}$$

Assuming that v_{e0} is the same for every electron [56], the transit time between plates that leads to a synchronous motion of electrons has to be an odd number of RF half-periods, it is

$$y(t_0 + \tfrac{NT}{2}) = d, \;\; N = 1, 3, 5\ldots \tag{3.6}$$

The integer N is called the order of multipactor. The electric voltage between plates satisfying this condition is

$$V_{RF} = \frac{m_e\,\omega\,d\,(\omega\,d - N\pi v_{e0})}{e\big(2\cos(\omega\,t_0) - N\pi\sin(\omega\,t_0)\big)} \tag{3.7}$$

Finally, the velocity of an electron in synchronism with the RF field is

$$v_e(t) \;=\; \begin{cases} v_{e0} + K\Big(\sin(\omega\, t_0) - \sin(\omega\, t)\Big), & t\,\epsilon\,\big[t_0, t_0 + \frac{N\,T}{2}\big] \\ -v_{e0} - K\Big(\sin(\omega\, t_0) + \sin(\omega\, t)\Big), & t\,\epsilon\,\big[t_0 + \frac{N\,T}{2}, t_0 + N\,T\big] \end{cases} \tag{3.8}$$

Eq. (3.8) describes the motion of the electron from one wall to the opposite (in the first interval of the expression) and the backward path (second interval). Two examples of such motion are shown in Fig. 3.3 for different parameters.

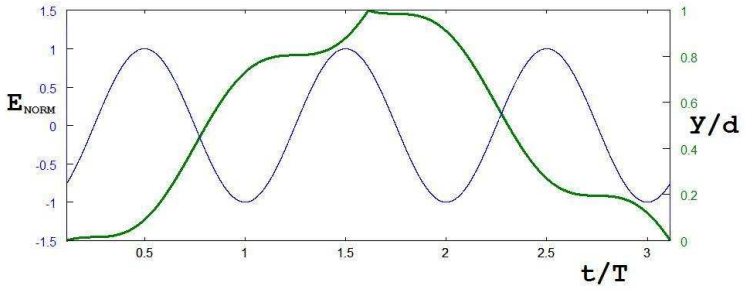

(a) Multipactor of order $N = 3$.

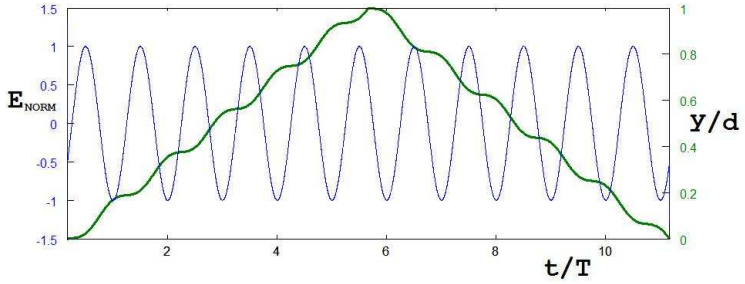

(b) Multipactor of order $N = 11$.

Figure 3.3: Resonant motion of an electron (thick line) in a parallel plates region for different orders of multipactor. The electron leaves the plate $y = 0$ at $t = 0$; it reaches the other plate $y = d$ at $t = \frac{NT}{2}$ and travels back to the first plate. The thin line stands for the normalized electric field intensity E_{NORM}.

Under resonant conditions and impact energies focused in the range of large electron gain, the number of electrons would grow infinitely. But there are several mechanism which lead the electron cloud to saturation. On one hand, the multipactor detunes the RF circuit; this detuning changes the field intensity E_y and, consequently, the resonant conditions. On the other hand, the loss of electrons from the walls turns them into positively charged, increasing the attraction the walls exert on surrounding electrons. Similarly, the electron cloud suffers a space charge effect because of the mutual culombian repulsion between electrons.

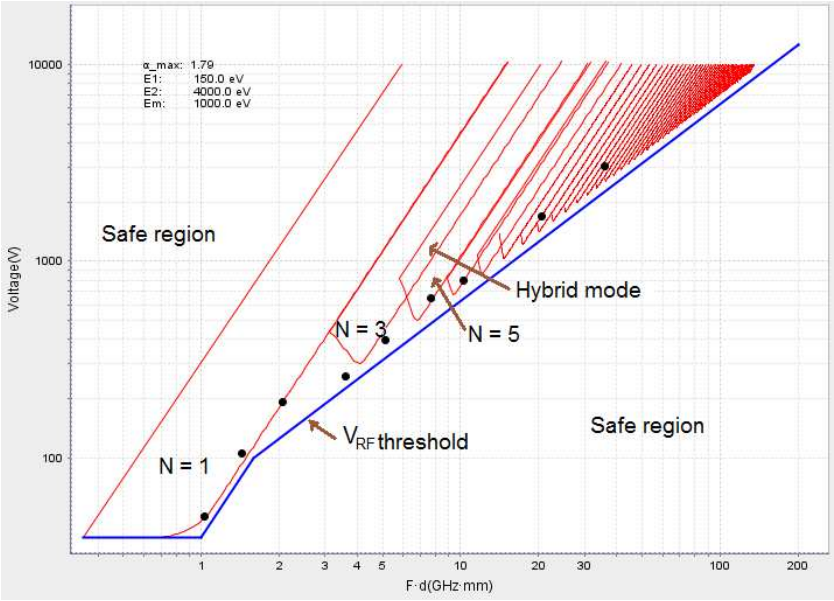

Figure 3.4: Susceptibility chart of gold obtained with the model [58].

Because of the variation in timing and energy of secondary emission, there is a range of voltages over which multipactor can occur for a given frequency and gap. Susceptibility charts plot such ranges as a function of the product of frequency and distance. Susceptibility curves are computed for different materials and geometries [15, 52]. A curve fitting process is followed to match with real measurements. It is also possible to exceed the multipactor sensitive band to higher voltages where the resonance conditions do not fulfill. Fig. 3.4 shows the susceptibility chart for a parallel plates geometry fabricated with gold. In this figure, the single points mark experimental voltage thresholds for different pairs of frequency-gap values; theoretical regions of multipactor are delimited by the continuous lines; the order of multipactor N has been calculated from (3.7). It is observed the overlapping of different multipactor order regions. This is because it is possible to have different orders satisfying above equations for the same product frequency-gap. Such situation indicates the coexistence in a discharge of electrons multipacting under different resonances, phenomenom known as hybrid modes of multipactor [33, 56, 57].

3.4 Analysis of the electromagnetic radiation of a multipactor discharge

Electric current is defined as charges in motion. In this sense, the above analysis has been applied to model the electric current of an electron under resonance conditions [59]. The following formulation can be applied to an effective electron, which concentrates the charge and mass of the electron population.

We start from the electric current density, which can be described as follows:

$$J_y(y,t) \;=\; -e\, v_e(t)\, \delta\left(y - y(t)\right) \tag{3.9}$$

The Dirac's delta δ in the previous equation remarks the concentration of the density of charge on the actual electron position. For a far-field analysis, we can consider that the charge is uniformly distributed on a thin wire along the gap. This approach allows to define an equivalent electric current as the spatial average of the density of charge:

$$I(t) \;=\; -\frac{e}{d} v_e(t) \tag{3.10}$$

The electric current inherits periodicity from the velocity (see (3.8)), so the Fourier series transformation is possible:

$$I(t) \;=\; -\frac{e}{d} \sum_{m=1}^{\infty} c_m \cos\left(\frac{m\omega t}{N} + \psi_m\right) \tag{3.11}$$

where module and phase of the Fourier expansion coefficients are, respectively,

$$c_m \;=\; \sqrt{a_m^2 + b_m^2} \tag{3.12a}$$

$$\psi_m \;=\; -\tan^{-1}\left(\frac{b_m}{a_m}\right) \tag{3.12b}$$

being

$$a_m \;=\; -\frac{2(1-(-1)^m)}{m\pi}\left(v_{e0} + K\sin(\omega\, t_0)\right)\sin\left(\frac{m\omega\, t_0}{N}\right) \tag{3.13a}$$

$$b_m \;=\; \frac{2(1-(-1)^m)}{m\pi}\left(v_{e0} + K\sin(\omega\, t_0)\right)\cos\left(\frac{m\omega\, t_0}{N}\right) + K\delta_{m,N} \tag{3.13b}$$

a_m and b_m are zero for m even. The Kronecker's delta $\delta_{m,N}$ term is active only for $m = N$ and comes from (3.8). and (3.11) describes the multipactor discharge in time domain. A representation in the frequency domain can be directly obtained as a train of deltas at the frequencies $m\omega/N$; c_m and ψ_m being the amplitude and phase of the deltas, respectively.

3.5 Multipactor testing

Multipactor testing of RF components before launching to space is usually recommended. In this sense, ESA has developed a standard procedure to assist the space industry of the telecommunication sector. The procedure is to determine the RF power margin between the operation conditions of the component and the multipactor RF power threshold found either theoretically or experimentally. Depending on such margin, the prototype component is considered safe or submitted to a laboratory for a real test. The component is supplied with RF power under simulated space conditions (vacuum, temperature, exposure to radiations) in the laboratory to detect the existence of multipactor events. Obviously, if a component fails these proofs, it has to be redesigned and reconstructed.

Components are classified into three types following ESA standard [58]. Type I include well vented, standard geometry components, and made of a metal whose SEY is well known. Multipactor

prediction is very accurate for this kind of components, so a margin of 3-8 dB (depending on testing) is considered safe. When the component also contains dielectrics with well established multipactor properties, it is considered as Type II. Acceptance margin for Type II is 3-10 dB. All other components are classified as Type III and the design margins range from 4-12 dB. However, common multipactor prediction tools are based on the parallel plates model, which provides a conservative prediction on the RF power threshold for more complex geometries.

The target of multipactor tests in the laboratory is to determine if the RF power threshold for multipactor is higher enough than the operating power range for the component of interest. Several multipactor detection methods have been developed for this purpose [52]. These are classified as global and local methods. Local methods have to be used close to the location of the discharge; on the other hand, global methods trigger when a multipactor event occurs anywhere in the test-bed. When performing systems tests on flight hardware, it is important to avoid multipactor in the entire RF system; consequently, a global method is preferred. Global methods can be applied without modifying the component. If otherwise the component is modified, its electromagnetic response would change and it migth result in wrong measurements. When we are interested in knowing where the discharge is taking place within a system, local methods are more useful. However, the use of several methods of detection minimizes the risk for misinterpretations. In this sense, ESA standard prescribes the use of at least two methods of detection, one of them should be global. The different detection methods are described below, starting from local methods:

- **Optical detection**: this method relies on the emission of photons during a multipactor event. Photons are released either from the component walls or from residual gas molecules, which electrons strike in their travel between surfaces. An optical fibre is placed as close as possible to the gap where the multipactor migth occur. This approaching is generally undertaken through the venting holes of a waveguide. It is recommended to have some venting holes in the waveguide path inside the vacuum chamber to facilitate the outgassing of the component. A photo-multiplier connected to the other end of the fibre allows to obtain a readable output.

- **Electron monitoring**: is similar to the optical detection. With this method, a thin conducting wire takes released electrons from the multipactor area, then an electron meter is used to monitor them; in order to attract the emitted electrons, the wire is positively polarized.

Global methods are summarized next:

- **Third harmonic**: in Sec 3.4 and (3.11) it is shown that a multipactor discharge generates harmonics at the odd multiples of f/N. Thus, indepently on the order of multipactor N, the harmonic $m = 3N$ which resonates at $3f$ is always present. On the other hand, high power amplifiers (HPA) used to supply test-beds are non-linear; they generate RF power at the natural harmonics of the main carrier. This fact causes the presence of an RF tone at $3f$ throughout the test duration [60]. The coincidence in frequency of this tone with the multipactor harmonic $m = 3N$ is the basis of the third harmonic detection system. A Spectrum analyser (SA) is used to monitor the HPA tone at the frequency $3f$ and display the variations produced by multipactor. It is a very reliable and fast method of detection. This makes it the preferred option when studying multipactor events that are short-lived.

- **Reflected power**: multipactor is known to be able to detune high Q-value components. The return loss of these components is a very stable value until the component is detuned. However, for low Q-value components or badly matched systems, the sensitivity of the method is low.

- **Nulling of Forward/Reverse Power**: multipactor detection system based on the comparison of incident and reflected signals. A small part of the incident and reflected power through the circuit is diverted to a equalizer system. Both signals are given equal amplitude but opposite phase, and their sum is displayed on a SA. The resulting signal shall remain constant unless the power ratio gets modified. This system is very sensitive to any alteration in the reflected power, such as those produced by multipactor.
- **Noise floor**: multipactor increases the noise floor close to the carrier frequency. This method requires the use of narrow bandwidth filters able to detect noise increments and reject the high power carrier, which could overload the measurement instrument.

3.6 Electron seeding

The presence of free electrons in the vacuum gap of the component is a necessary condition to have a multipactor discharge. There are multiple sources of electrons in space, such as the Van Allen belts and the solar wind [61]. Moreover, during the launch process, a satellite may travel through the ionosphere, where the concentration of electrons is high due to the solar activity. On the other hand, electrons can be released from the walls of the payload because of the action of a strong electromagnetic field; or just escape from a molecule of residual gas within the RF system. Finally, there is the possibility of an external radiation or particle impacts on the surface of a component and release electrons from it. This last method is the one followed in the laboratory to have a favorable population of free electrons traveling through the RF system inside the vacuum chamber. The excitation of electrons with radiation implies the usage of a radioactive source, like Strontium-90. The manipulation of radioactive materials requires the observance of a very strict protocol and special qualification is mandatory for the laboratory staff. For these reasons, and with the aim of avoiding health risks, radioactive sources are being replaced with ultraviolet lamps [62]. Photons in the ultraviolet range can extract electrons from a material by means of the photoelectric effect. The lamp provides a flux of photons, which are injected into the waveguide cavity using an optical fibre. These photons will hit the walls of the guide and release the primary electrons necessary to initiate the multipactor process.

Chapter 4

Electromagnetic radiation of a single-carrier multipactor discharge

4.1 Introduction

Satellites and spacecrafts are exposed to a constant bombardment of high-energy particles in space. The strikes of these particles on metallic components release electrons, which, under certain conditions, ignite the multipactor process. Multipactoring is considered harmful for the proper operation of an RF subsystem, some of its consequences being the heating of waveguides, outgassing, noise on communications and power dissipation. Several studies have contributed to the development of numerical tools capable of simulating multipactor in different scenarios [16, 20, 23].

The propagation of the electromagnetic energy radiated by a multipactor discharge in a passive microwave waveguide component is studied in this chapter. A fullwave formulation for the radiation of a multipactor discharge is presented in the context of the microwave multimode network theory [45]. An equivalent circuital network for the discharge based on distributed elements is derived. The combination of such circuit with the transmission-lines network of a microwave component provides a generalized representation of the multipactor event. A multipactor simulation following the Particle-In-Cell (PIC) code [63] has been used to generate the current that excitates the lumped circuit. Experimental measurements of the spectrum generated by a discharge are compared with theoretical results, obtaining good agreement. A preliminary work of this technique in single-mode analysis can be found in [64].

The RF High Power Laboratories at ESA/ESTEC facilities supported a multipactor test campaign to validate the present theory. A total of ten tests were performed. The RF power at the frequencies of two intermediate harmonics was observed throughout the tests. Notable disturbances on the power at such frequencies were detected during multipactor events for five times. A description of procedures and results is reported in this chapter.

This chapter is divided into five sections, besides the introduction. Sec. 4.2 is devoted to the microwave component used for testing; a detailed description of the test-bed, including design process and functionality, is given in Sec. 4.3. Sec. 4.4 summarizes the procedure and results of the test developed in the laboratory. The theoretical characterization of multipactor discharges within an RF component is given in Sec 4.5; finally, in Sec 4.6, this method is applied to study the power spectrum

Id	**Description**	**Ports size**	**Surface recovery**	**Gap** (mm)	**Frequency** (GHz)	**Order of multipactor**	**Power threshold** (W)
1	Transformer	WR-75	Au	0.15	12.5	1	1255-1460
2	Transformer	WR-75	Ag	0.32	12.5	3	1940-2450
4	BPF	WR-75	Ag	5.00	12.0	31-43	983-3870
5	LPF	WR-75	Ag	0.30	12.0	3	618-770
7	LPF	WR-90	Ag	2.13	10.5	13-15	6430-10500
8	Transformer	WR-90	Ag	1.25	10.5	9-11	5450-7600

Table 4.1: Basic description of the 6 candidate samples available for testing.

radiated during a multipactor event in the component tested in the laboratory. A comparison of the theoretical results and the laboratory measurements is given at the end of the chapter.

4.2 Device under test

4.2.1 Introduction

The selection process of a microwave component suitable for running the multipactor test campaign, as well as a complete description of such component, are detailed in the present section.

4.2.2 Selection of a component for testing

The development of this research involves the comparison of theoretical and experimental results for a multipactor event occurring within a waveguide device. In this sense, the use of a component whose electromagnetic and multipactor properties are well known is required. In this docmuent, we focus on a set of 6 candidate components, designed for multipactor research. These devices are structures based on rectangular waveguides for operating in the microwave Ku-band. Accurate and very realistic models of the components have been built on the software package FEST3D. FEST3D is a software tool for the electromagnetic analysis of passive components, which among other capabilities, provides a multipactor prediction module. For this purpose, a length measurement study of all the pieces was performed and used to design the software models. A basic summary of the candidate devices and multipactor parameters is shown in Table 4.1. Predictions on the order of multipactor and power threshold using FEST3D and ECSS MP-tool are given in the table. These parameters vary with the frequency of excitation. The frequency has been chosen considering the scattering paratemeters of the components within the operational range of frequencies of the test-bed (this operational range is between $10.5 - 12.5$ GHz as will be shown in Sec 4.3.1). The column named Gap refers to the smallest waveguide height, which can be considered as the region most sensitive to multipactor. Fig. 4.1 shows the susceptibility chart of the components in this bandwidth.

The following samples have been discarded because of limitations:

- Sample 1: Multipactor order $N = 1$ in the operational range. The sample is discarded since a discharge of order $N = 1$ does not generate intermediate harmonics.

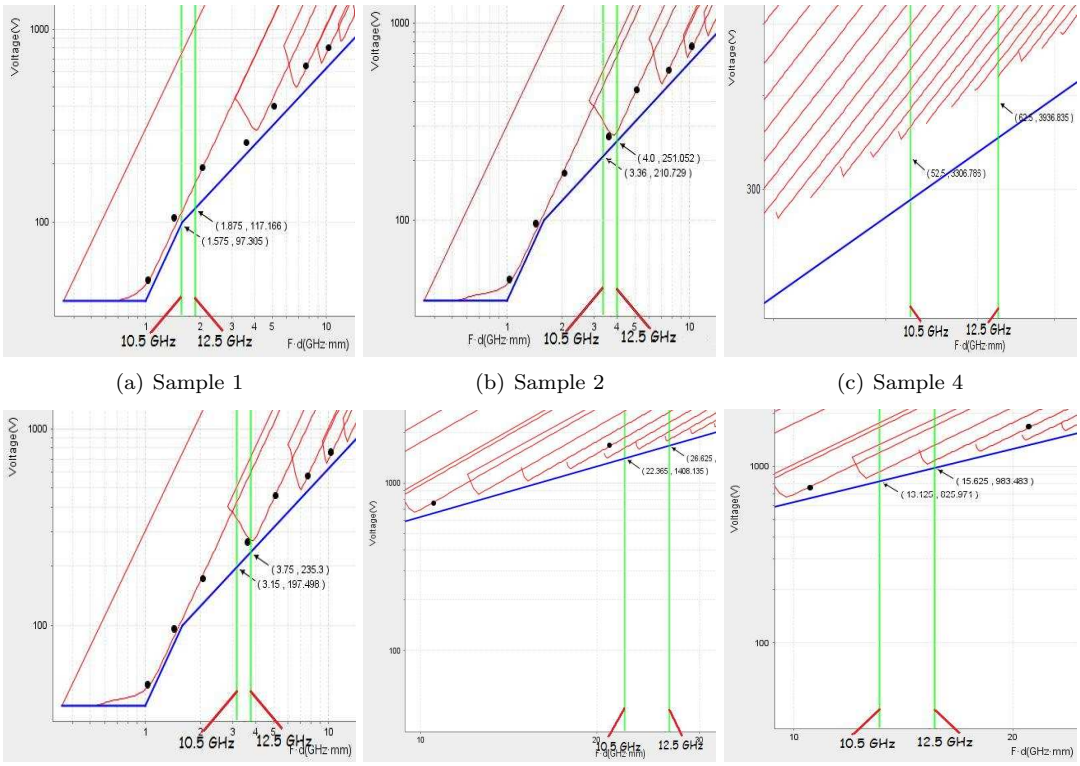

(a) Sample 1 (b) Sample 2 (c) Sample 4

(d) Sample 5 (e) Sample 7 (f) Sample 8

Figure 4.1: Multipactor susceptibility charts for the 6 candidate samples.

Multipactor harmonic	$m = 3$	$m = 5$
Range of frequencies (GHz)	$17.5 - 20.833$	$24.5 - 29.167$

Table 4.2: Available bandwidths for multipactor harmonics $m = 3$ and $m = 5$ for a discharge of order $N = 3$. $10.5 < f < 12.5$ GHz.

- Sample 4: Multipactor order very high and unstable. The susceptibility regions of succesive orders are very close in power for this component (see Fig 4.1(c)). This can cause variations in the order during the test campaign; the occurrence of hybrid order events is another handicap. Finally, actual simulations of high order discharges do not guarantee the accuracy required.
- Sample 7: Multipactor threshold very high for the test-bed.
- Sample 8: Multipactor threshold very high for the test-bed.

Thus there are two components preselected: samples 2 and 5. The multipactor order in the operational range of the test-bed is $N = 3$ for both components. Due to the cut-off frequency of the waveguide (7.8 GHz), the two lower harmonics of a multipactor discharge that can propagate through the WR-75 ports of these components are $m = 5$ and $m = 7$ (besides the harmonic $m = 3$, which coincides with the excitation). The frequency of these signals will be finally fixed by the running frequency of the test; Table 4.2 shows the bandwidth where such resonances might occur.

The third harmonic detection system [60] analyses disturbances on the power at the third natural harmonic $3f$. High-power amplifiers used for multipactor testing generate an RF tone at this frequency as a consequence of non-linear effects in the power amplification process. Such signal has a high Signal to noise ratio (SNR) and can be easily followed in a SA during the test. A multipactor discharge shall produce quick power variations at this frequency, which are displayed in the SA as spikes on the signal envelope. In this work, an novel and alternative method of detection of multipactor is proposed. It is the detection of intermediate harmonics. As shown in (3.11), a multipactor discharge of order $N = 3$ generates intermediate harmonics at $m = 5, 7$; and the third harmonic resonates at $m = 3N = 9$. The principle of operation of the intermediate harmonics detection method is the same as stated for the third harmonic detection system. The main difference between both methods relies on the fact that the test-bed does not provide any tone at the resonant frequency of intermediate harmonics. These harmonics will resonate below the noise floor, where multipactor spikes are more difficult to recognize. This situation will get worse if resonances are attenuated through the Device under test (DUT) waveguide. For this reason, it is important to select the work frequency based on the frequency response of the DUT. In order to avoid attenuation, the multipactor intermediate harmonics must appear within the band-pass of the DUT, or else at a spurious band. On the other hand, test-beds also introduce restrictions to the work frequency. The response of the different components in the test-bed can cause excessive losses and reflections at certain frequency bands. Thus, a trade-off must be achieved between the two criteria when deciding the operational frequency of the test. Moreover, a fine filtering and amplification of the resonant frequencies of harmonics is required in order to ensure a satisfactory detection of multipactor spikes at the moment of a discharge.

A series of multipactor tests were initially performed using the sample 5 as DUT. No power was registered on the intermediate harmonic detection system during multipactor events in all the tests. However, the discharges were satisfactorly detected on the traditional detection systems also implemented in the measuring set-up: optical detection, pressure monitoring, third harmonic and

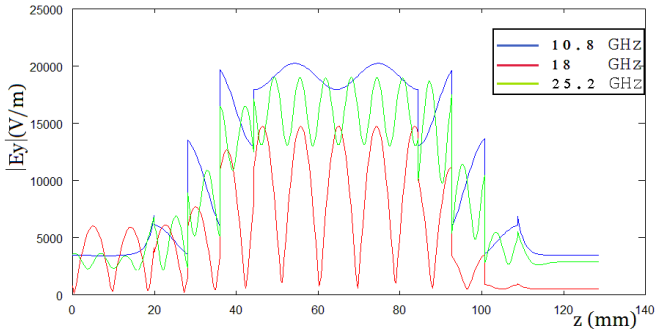

(a) Sample 2.

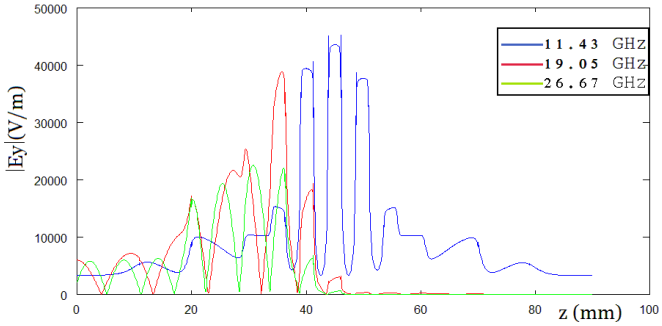

(b) Sample 5.

Figure 4.2: Electric field distribution on the z axix at the frequencies of interest. $x = a/2$ and $y = b/2$.

nulling of forward/reverse power. An explanation of these false-negative results is given in Fig. 4.2(b). The high attenuation at the resonant frequency of the intermediate harmonics avoids their correct detection in a SA. On the other hand, the presence of spurious bands in the response of sample 2 allows to transmit such harmonics to the detection system, as can be seen in Fig. 4.2(a). This result illustrates the importance of selecting a suitable work frequency well adapted to the DUT.

The frequency response of the sample 2 is shown in Fig. 4.3 for the frequency bands of interest. It is observed that the band-pass is too narrow to include any intermediate harmonic. Two spurious bands suitable for the transmission of the $m = 5$ harmonic are identified around 17.68 and 20.05 GHz. Consequently, the work frequency should be either 10.61 or 12.03 GHz. The test-bed was checked at both frequencies and around a bandwidth of 60 MHz. This bandwidth is closed to the 100 MHz 3dB-bandwidth of the spurious bands. Both options, although being ideal under the point of view of the DUT, were finally rejected because of the bad response of the test-bed. The frequency 10.8 GHz was instead selected to be the work frequency for testing, because of the good response of the DUT as well as the test-bed.

The test campaign was performed using as DUT the sample 2. A deeper description of this device is given in the following section.

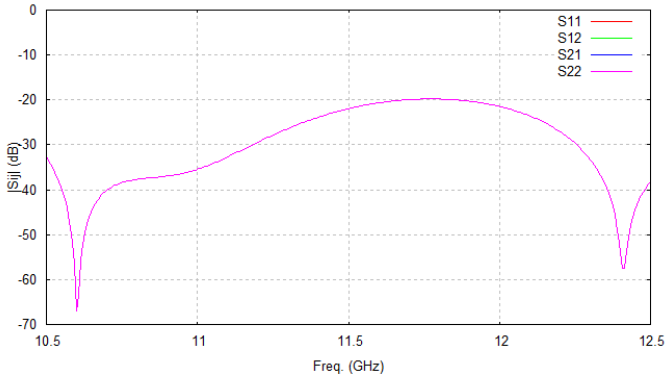

(a) Frequency range for the input signal $f \in (10.5, 12.5)$ GHz

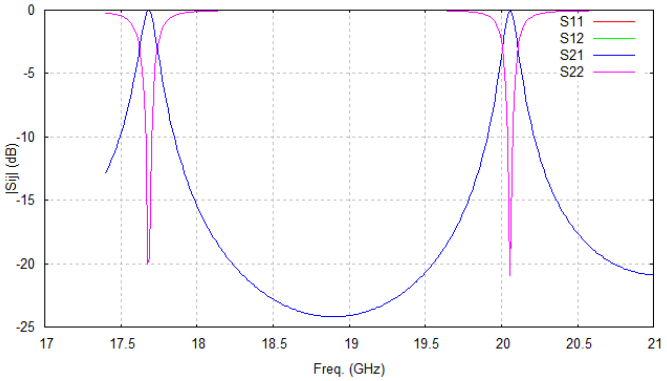

(b) Frequency range for the harmonic $^5/_3 f \in (17.5, 20.83)$ GHz

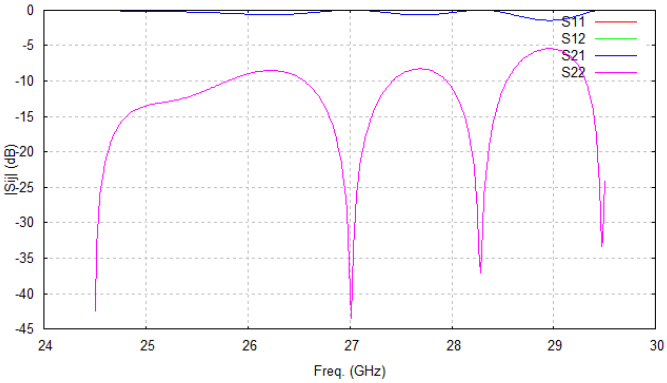

(c) Frequency range for the harmonic $^7/_3 f \in (24.5, 29.16)$ GHz

Figure 4.3: Scattering parameters for the sample 2 in the frequency bands of interest.

(a) Open. (b) Close.

Figure 4.4: Photograph of the device under test (sample 2).

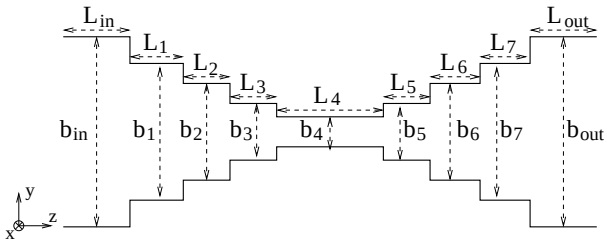

Figure 4.5: Scheme of the DUT.

4.2.3 Selected test sample

The device under test is an E-plane, silver-plated waveguide transformer, with input/output ports in standard WR-75. A picture of this component is shown in Fig. 4.4. It has been designed with a long and narrow central section (0.32 mm gap) prone to multipactor discharges. The dimension of the waveguides conforming the component are summarized in Table 4.3. The order of multipactor discharges within this component at $f = 10.8$ GHz may be $N = 3$. Table 4.4 shows the resonant frequencies of the five lower harmonics generated by such discharges. Note that the first harmonic $m = 1$ cannot propagate through the WR-75 guide. The harmonic $m = 3$ coincides with the high-power input signal, meanwhile $m = 9$ is analysed in the third harmonic detection system. Thus, the multipactor intermediate harmonics detection system has been tuned to study the harmonics $m = 5$ and $m = 7$ during the test campaign.

WG Section	1	2	3	4	5	6	7
L_i (mm)	8.11	8.03	8.24	40.04	8.24	8.03	8.11
b_i (mm)	5.46	1.44	0.44	0.32	0.44	1.44	5.46

Table 4.3: Dimensions of the DUT. The ports are standard WR-75 waveguides ($a = 19.05\,mm$, $b_{in} = b_{out} = 9.525\,mm$)

m	1	3	5	7	9
$(m/N)f$	3.6	10.8	18.0	25.2	32.4

Table 4.4: Frequency (in GHz) of the harmonics of a multipactor discharge of order $N = 3$ at $f = 10.8$ GHz.

4.3 Test-bed

4.3.1 Description of the test-bed

A descritpion of the test-bed used for the intermediate multipactor harmonics is detailed in the this section. A schematic of the test-bed is shown in Fig. 4.6. The DUT is to be placed inside the vacuum chamber under low pressure ($P \approx 2 \cdot 10^{-7}$ mbar). The test-bed can be divided into three parts. The input part supplies the DUT with a high power RF pulsed tone at f and collects control data; the output part includes the multipactor harmonics measurement systems and is entrusted with the output power dissipation; finally, the vacuum chamber itself, where the DUT is assembled between the input and output parts of the test-bed. Traditional multipactor detection systems are also implemented in the test-bed. The components included in these three parts are summarized next.

Input section

- **Signal Generator**: it provides a small-signal single carrier at f to the high-power amplifier and controls its amplitude. During test, the power is increased in several steps until a discharge

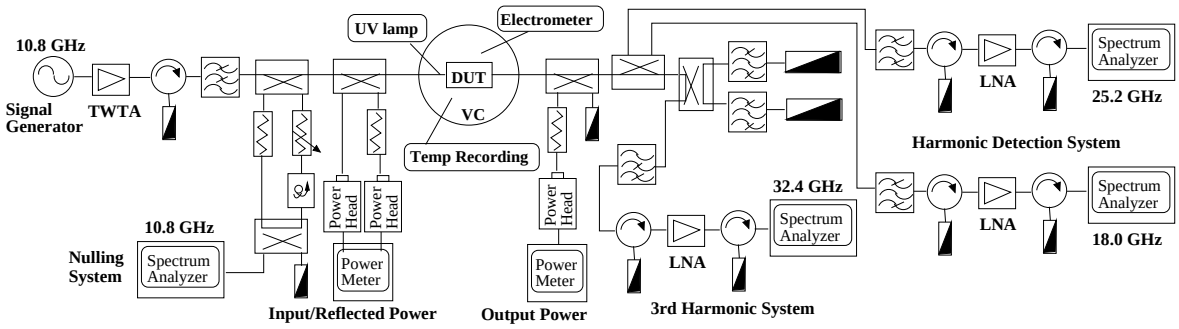

Figure 4.6: Test-bed schematic.

is detected.

- **Pulse Generator**: it defines the pulses for the high-power signal modulation. It is set up to give 1000 pulses per second with a duration of 20 μs each: $PRF = 1$ KHz, $PW = 20$ μs, $DC = 2\%$ (Duty Cycle). This signal is also used to trigger the power meters. For the satisfactory development of multipactor testing, the duration of pulses has to be long enough to allow the formation of a notable multipactor discharge. Using the present configuration, there are 214 thousand periods per pulse for $f = 10.8$ GHz.
- **High-Power Amplifier**: also known as Travelling wave tube amplifier (TWTA). It supplies the circuit with RF high power pulses. This kind of high power sources introduce tones at the fundamental harmonics of the operating frequency f due to a non-linear effect in the power amplification process. Such signals will not interfere in the properties of multipactor because of their relative low amplitude and high frequency. On the other hand, the signal at $3f$ allows to enable the third harmonic detection system. The amplifier operates in the band $10.5 - 12.5$ GHz and can provide up to 9 kW output power.
- **Isolator**: a high power isolator is used to avoid reflected power from damaging the amplifier.
- **Low Pass Filter**: reduces noise level and undesirable harmonics.
- **Bi-directional Couplers**: two couplers are used to extract low-level samples of incident and reflected power from the main RF path. Such signals are necessary for the implementation of the nulling detection system and for power readings at power meters.
- **Power Meter**: the incident and reflected power levels at the DUT input port are constantly monitored at two power meters. Two power heads connect them to the RF circuit. The calibration procedure followed for these instruments is detailed in Sec 4.3.3. Attenuators are used to lower the RF power to the appropiate level.
- **Nulling of Forward/Reverse Power Detection System**: multipactor detection system based on the comparison of the incident and rejected RF signals (see Sec 3.5). It is made up of a variable attenuator, a variable phase shifter and a 3dB-hybrid. These components are used to manually equalize both signals in amplitude and opposite phase. The resulting signal is then shown on a SA.

Vacuum chamber

The DUT is placed inside a vacuum chamber. The input and output parts of the test-bed are connected to the DUT through two flanges. An optical fibre injects photons from an ultraviolet lamp to the input port of the DUT through a venting hole in the waveguide section placed just prior to the DUT. The photons are used to obtain primary electrons within the waveguide region by means of the photoelectric effect (see Sec 3.6 for more details). The lamp used is a $44 \cdot 10^6$ e^-/s Hg lamp. A set of sensors check pressure and temperature close to the DUT during the test running.

Output section

- **Transmitted power measurement system**: a small portion of the RF power that exits the DUT is redirected from a coupler to a power head. Then a power meter is used to read the transmitted power level.

Frequency (GHz)	WR-75	WR-62	WR-51	WR-42
$f = 10.8$	0.15	0.29	756.65	1637.04
$5/3f = 18.0$	0.11	0.15	0.23	0.44
$7/3f = 25.2$	0.11	0.15	0.20	0.33

Table 4.5: Attenuation Rate in dB/m for standard rectangular waveguides.

- **Isolator**: during the test-bed preparation, it was noted that the reflected power level was high and could damage the RF source. An isolator was put to improve the performance of the test-bed.

- **Multipactor intermediate harmonics detection system**: the present test campaign is devoted to the characterization of the harmonics of a multipactor discharge. In this sense, the intermediate harmonic detection system is the most important circuit in the test-bed. It has been designed for providing 3 different harmonics to spectrum analysers. The high power fundamental carrier at f and the natural harmonics introduced by the TWTA have to be rejected before they enter into the spectrum analysers. A bi-directional coupler in combination with a 3dB-hybrid are used to divide the RF power flow into different paths, from where the required frequencies are filtered. Filtering is made by waveguide narrowing followed by standard Band-pass filters (BPFs). The cut-off frequency of a waveguide rises as the cross-section size is reduced. The power at f will suffer a hard attenuation if the hollow is narrowed enough. Attenuation rates for different rectangular waveguides are shown in Table 4.5 at the frequencies of interest. The rejection of the main carrier, without a significant attenuation of the multipactor harmonics, is done by narrowing from WR-75 to WR-51; a 20 cm long WR-51 thru completes the high-pass filtering. Then, the BPFs select the harmonic of interest for each path. A set of Low noise amplifiers (LNAs) adjust the signal level of the multipactor harmonics to the right input level of the spectrum analysers. Several isolators have been placed on the caution of protecting the sensitive LNAs against power reflections.

- **Third harmonic detection system**: the third harmonic is shown on a spectrum analyzer following the same procedure as for the intermediate harmonics. This time, the signal is not coming from a coupler, but from a 3dB-hybrid.

- **3dB-Hybrid**: it splits the RF flow into two paths for power dissipation at the end of the circuit. The 3dB-hybrid is also used to deliver the harmonics back to the multipactor harmonics detection systems.

- **Band Pass Filter**: two band-pass filters are set at the output of the 3dB-hybrid to let the power at f to dissipate in the high-power loads, meanwhile the harmonics are reflected for their analysis.

- **High-power Loads**: dissipate the main RF power at the end of the circuit.

Spectrum Analyser	**Frequency center**(GHz)	**Span** (KHz)	**RBW** (KHz)	**VBW** (KHz)	**SWT** (ms)	**Atten** (dB)	**Ref Level** (dBm)	**dB/div**
F/R Nulling	10.8	200	3	3	67	10	-19.4	10
$^5/_3 f$ Harmonic	18.0	60	3	10	100	5	-40	10
$^7/_3 f$ Harmonic	25.2	80	3	10	100	10	-20	10
3^{rd} Harmonic	32.4	300	3	3	84	10	0	10

Table 4.6: SA configuration parameters. A description of these parameters can be found in [65, 66].

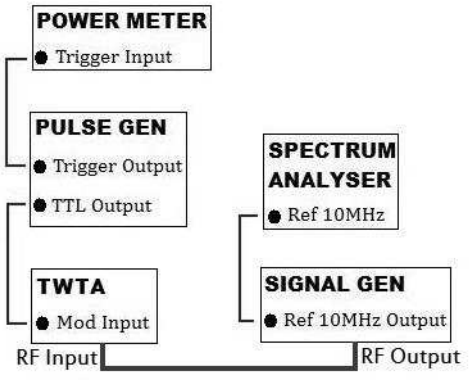

Figure 4.7: Diagram of interconnection of the laboratory instruments used in the test-bed for the configuration of the local-oscillator reference and trigger signals.

4.3.2 Configuration of the laboratory instruments

The laboratory equipment used during the running of the tests requires of certain configuration, giving special attention to synchronism (see Fig. 4.7). The configuration details are given next:

- The pulses generator will provide 5 V amplitude pulses series to the High power amplifier (HPA) as modulation signal.
- The power meters are set to measure the RF power only during the pulses time on. The rising edge of the pulses is used to trigger the power meters for this reason.
- The spectrum analysers may take all the same reference oscillator to increase the precision and stability on their lectures. The signal generator will provide the reference signal. Additional configuration parameters for the spectrum analysers are given in Table 4.6.

4.3.3 Test-bed calibration

A satisfactory test-bed design requires the prediction of the RF power that would load any component during the operation of the system. It is specially important for sensitive points, such as

the interfaces of measurement instruments. Usually it is enough to ensure that the power loading a component would be under its safety limit. For this purpose, a quick estimation of power is right enough. Other times an accurate prediction of power is mandatory, either because it is the target of the test-bed to measure the power at such point, or because there is risk of exceeding the equipment power limit and cause severe damages. Moreover, test-beds usually have points where power should be measured despite they are not physically accessible. Then, the power at that point has to be related to the measure done in a more accesible point. This process is known as calibration. The former point is called the reference point, meanwhile the later is the measurement point. The reference point can be inaccessible to a measurement instrument due to physical restrictions (e.g. components placed inside a vacuum vessel) or because the expected power level would overload it. Furthermore, measuring procedures imply to connect a probe to the target point, what would interfere with the proper operation of the system. Thus, power measurements are usually given by means of couplers placed in the circuit. Such couplers allow the user to extract a small sample of energy without disrupting the operation of the test-bed. Calibration processes consist on the comparison of the power readings at two different points for the same input signal. Assuming linearity, the difference between both readings should remain constant at different input power values; on the other hand, when non-lineal devices are involved, we need more reading pairs to make a matching curve. Calibrations should be repeated at each frequency of interest.

The maximum input power specified for a measurement instrument should never be exceeded to avoid malfunction and serious damage. For this reason, it is important to execute a power budget of the set-up. A power budget gives the power difference (in dB) between any point in the circuit and the input. The nominal losses and/or gains of components can be used to make an approximate power budget, from where the sensitive points of the circuit are determined. This calculation gives an idea of where is recommended to put attenuators and amplifiers. These components are necessary in order to have the outputs of the circuit within the dynamic range of the reading instruments.

The calibration techniques used in the preparation of the test-bed are described next. The target here is to know the RF power flux at the DUT of the multipactor experiment. The experiment requires to measure the incident, reflected and transmitted power of the DUT during a multipactor event. Fig. 4.8(a) shows a schemme of the input section of the test-bed, from the power source to the input of the DUT, this later named the reference point. There are two reading points that will be used to monitor the incident and reflected power. A bi-directional coupler is dedicated to this purpose. The first step in the calibration is to fix the origin of the measurement system with the power level measured at the reference point. A power head is connected to the reference point and the system is supplied with power according to the power budget (see Fig. 4.8(b)). The lecture of the power meter is set to 0 dB or calibration reference; note that the coupler output ports should be matched during the operation. Once the calibration reference is settled, the incident and reflected powers are calibrated following Fig. 4.8(c) and 4.8(d), respectively. The short circuit in 4.8(d) is used to reflect the power at the reference point. On the other hand, the calibration of the transmitted signal is described in Fig. 4.9: the reference level is obtained by connecting the power head to the RF source, then the same power level is used to supply the output part of the test-bed as in Fig. 4.9(b).

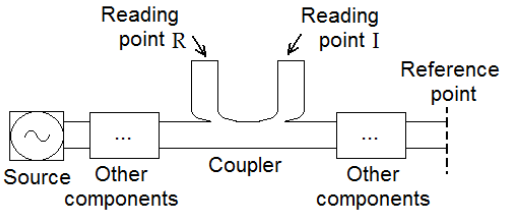

(a) Characteristic points for the calibration of the incident and reflected power at the DUT input.

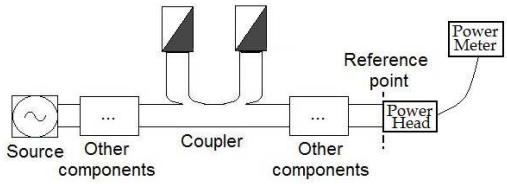

(b) Reference level set at the DUT input-port. The coupler exits must be matched.

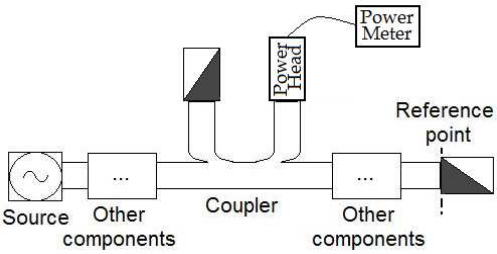

(c) Incident power calibration. The reference point must be matched.

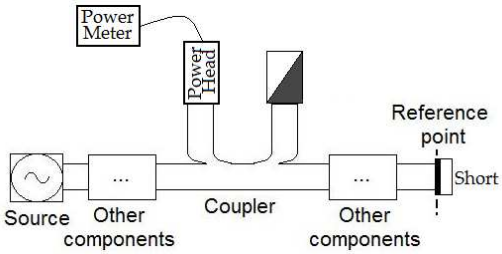

(d) Reflected power calibration. The short circuit at the reference point reflects the incident power.

Figure 4.8: Calibration process of the input section of the test-bed.

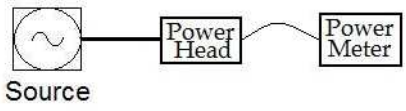

(a) Reference level set at the source port.

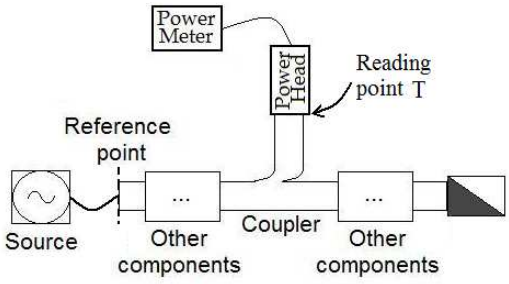

(b) Measurement of the power difference from the source to the reading point T

Figure 4.9: Calibration process of the transmitted power of the DUT output.

4.4 Development of laboratory test

4.4.1 Introduction

In this section, the procedure followed during the development of the multipactor test is outlined. The output of the different detection systems implemented in the test-bed are also shown.

4.4.2 Multipactor thru evaluation test procedure

The test-bed was checked using a WR-75 thru instead of the DUT to show the absence of discharges up to 6600 W inside the waveguide. All the multipactor detection systems implemented in the test-bed were continuously used during this operation. No breakdown events were observed.

4.4.3 Multipactor test parameters

- Frequency: 10.8 GHz
- Pressure: $< 10^{-6}$ mbar
- Temperature: $+21.3 \pm 0.1$ °C
- PW: 20 μs
- PRF: 1 KHz

4.4.4 Test results

Fig. 4.10 shows the power levels and pressure at the DUT during the test running. A multipactor event was detected after 1 minute of exposure at 3150 W incident power. The discharge was noticed on the multipactor detection systems implemented in the test-bed. The pressure sensor registered a raise from $5.2 \cdot 10^{-8}$ up to $2.1 \cdot 10^{-7}$ mbar. The discharge produced a sudden fluctuation in the power at the DUT:

- Incident power: 18 W or 0.3%
- Transmitted power: 291 W or 10%
- Reflected power: 18 W or 18%

The display of the spectrum analysers used in the test-bed is given in Fig. 4.11. Table 4.7 shows the power levels of the main peaks registered on the intermediate harmonic spectrum analysers. The value of these peaks will be used in comparison to theoretical and experimental results in Sec. 4.6.4.

4.5 Characterization of multipactor discharges occurring within passive components

4.5.1 Introduction

A procedure for the characterization of microwave components affected by multipactor discharges is proposed in this section. Our aim is to study the propagation of the electromagnetic fields radiated

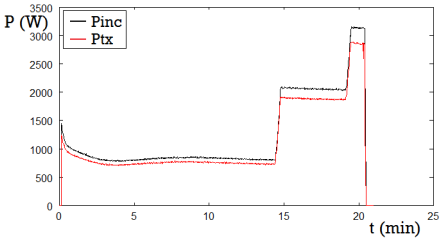

(a) Incident and transmitted power (W).

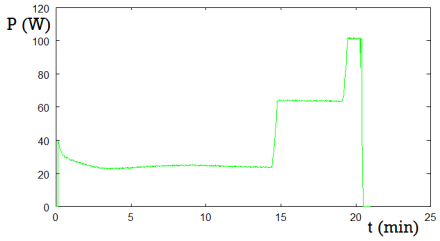

(b) Reflected power (W).

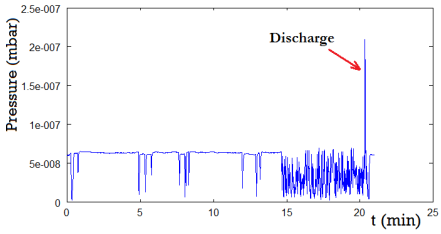

(c) Pressure (mbar).

Figure 4.10: Evolution of the power and the pressure during the test.

Spectrum Analyser	**Frequency** (GHz)	**Peak Power at SA** (dBm)		**Peak Power at DUT** (dBm)	
$^{5}/_{3}f$ Harmonic	18.0	-73.73	-77.34	-61.83	-65.44
$^{7}/_{3}f$ Harmonic	25.2	-49	-50	-45	-46

Table 4.7: Peaks of power detected on the intermediate harmonic spectrum analysers.

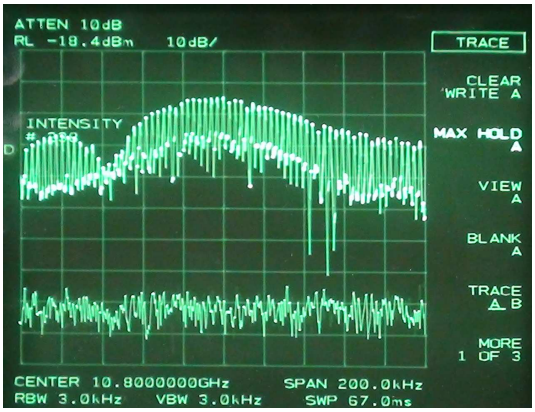

(a) Forward/Reverse Nulling system.

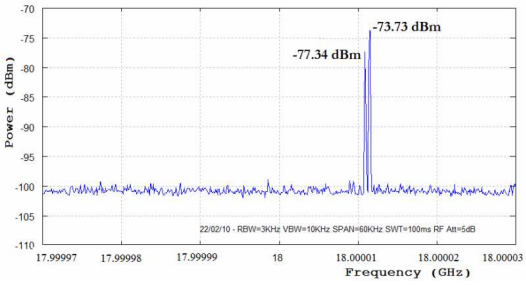

(b) $m = 5$ intermediate harmonic detection system.

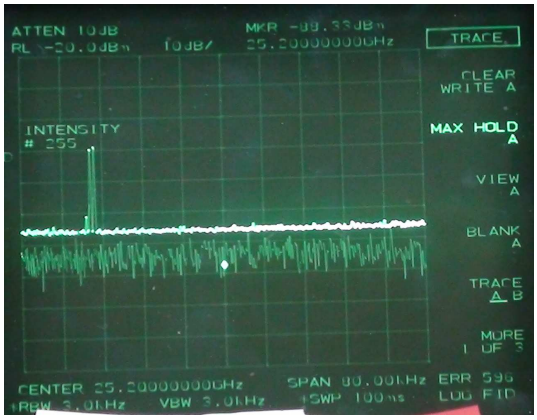

(c) $m = 7$ intermediate harmonic detection system.

Figure 4.11: Display of the spectrum analysers after the discharge. The two traces displayed in (a) and (c) are Max-Hold and Normal lectures. The former one records the maximum level, which is obtained during the multipactor event; the last one is taken after the discharge. In (b) only the Max-Hold lecture is shown.

throughout a passive component as a consequence of a multipactor episode. A multimode network for common passive components as well as an equivalent circuit which characterizes multipactor currents will be developed in the following sections. The coupling procedure of such networks used to obtain the electromagnetic energy radiated by the multipactor event is also presented. Moreover, we undertake an application example using a software model of the DUT used in the previous section, it is an E-plane transformer implemented in rectangular waveguide.

4.5.2 Full-wave characterization of a passive component

The basic procedure for obtaining field solutions of a time-harmonic excited waveguide component utilizes the representation of field variables and their sources in terms of a complete set of orthonormal vector eigenfunctions [45]. A representation by means of TE and TM modes is usually followed in bounded regions, like a perfectly conducting waveguide. The orthogonality properties of eigenfunctions over the cross-section of the waveguide involve only transverse field components, meanwhile the longitudinal fields are therefrom derived. A network schematic of the component and the field sources based on transmission-line theory transforms the steady-state Maxwell vector field equations into scalar transmission-line equations. The analysis of such a network gives us transmission-line voltages and currents, which represent the amplitude coefficients in the modal expansion of the transverse electric and magnetic fields, respectively.

The equivalent network of a passive component used for the study of the multipactor effect is given in Fig. 4.12. The different parts in which the component is divided for its analysis are shown in this figure. These parts are on one hand the waveguide section where the multipactor discharge will take place, and on the other hand the rest of the device, including other waveguide sections and discontinuities. The distribution of the electric field intensity within the aforementioned waveguide allows to predict the most probable location for the ignition of multipactor processes. Then, the waveguide is splited in two sections at this point, the sum of their lengths equaling the length of the original waveguide. This division will allow to introduce the circuital representation of the discharge at the point of interest, as will be explained in Sec. 4.5.4. The resulting two waveguide sections are characterized by the impedance matrices $[Z_{X_L}]$ and $[Z_{X_R}]$. The analytical representation of such matrices is trivial, since they represent a waveguide without discontinuities (see Fig. 4.13(b)). On the other hand, the rest of the component, where other waveguide sections and discontinuities are included, can be characterized via full-wave software. The result of such computations are the matrices $[Z_L]$ and $[Z_R]$ for the left and right sides of the multipactor waveguide, respectively. In this way, the part of the component covering from the input-port to the begining of the multipactor waveguide is characterized by $[Z_L]$; meanwhile the matrix $[Z_R]$ represents the side of the component from the end of the multipactor waveguide to the output-port of the component. It is true that the two sections of the splitted waveguide could be included in the software computations of $[Z_L]$ and $[Z_R]$; but the separate treatment of the matrices $[Z_{X_L}]$ and $[Z_{X_R}]$ allows to acomplish quick corrections on the location of the discharge.

Fig. 4.12 also shows other elements necessary for the characterization of the problem. These elements are the rest of the microwave system and the RF signal which supplies the component. A perfect coupling is assumed between the components of the microwave system, in order to avoid power reflections; thus, the line and the ports of the component are given the same impedance, here represented by the matrices $[Z_0]$ (see Fig. 4.13(a)). Finally, the incident RF signal has been characterized by a time-harmonic voltage source of frequency $f = \omega/(2\pi)$ and amplitude V_g. A time dependence $e^{j\omega t}$ is assumed throughout this work. There is only one voltage source in the multimode

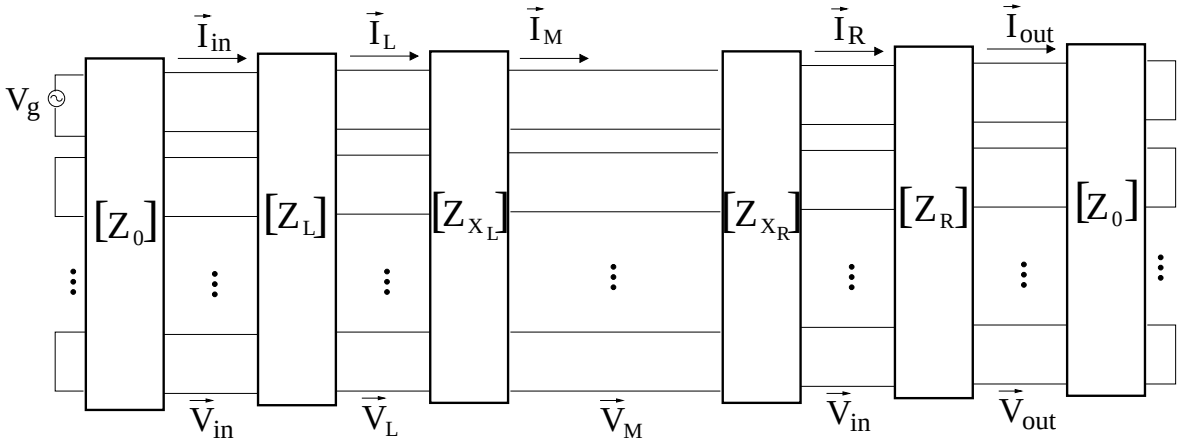

Figure 4.12: Multimode network of a passive waveguide component under single-mode excitation. $\vec{I}_M$ and $\vec{V}_M$ are the modal currents and voltages at the waveguide section where multipaction occurs.

network because the propagation of the incident signal is supposed to be single-mode at the work frequency.

The modal voltages and currents in the system shown in Fig. 4.12 are each other related by means of the following expressions:

$$V_{in}^{(k)} = V_{exc}^{(k)} - Z_0^{(k)} I_{in}^{(k)} \tag{4.1}$$

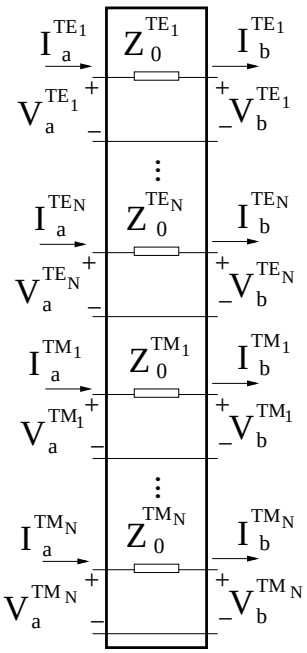

(a) Schematic of the matrix (Z_0), used to denote the perfect coupling of the component within the microwave system.

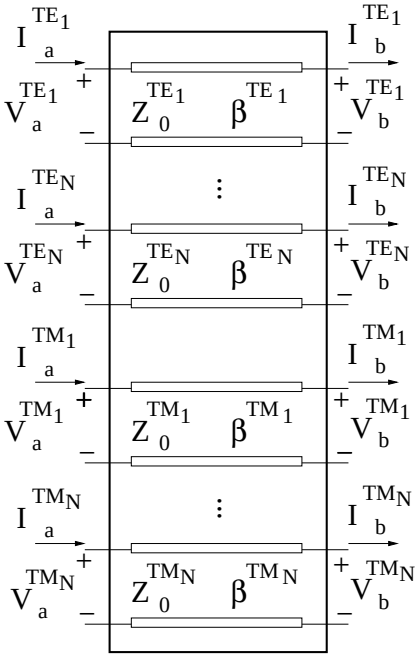

(b) An homogeneous section of waveguide, as the ones represented by the matrices (Z_{X_L}) and (Z_{X_R}).

Figure 4.13: Fullwave schematics of some matrices used in the network representation of the system.

$$V_{in}^{(k)} = \sum_{i=1}^{N} \left(Z_{\substack{ik \\ 11}}^{L} \, I_{in}^{(i)} - Z_{\substack{ik \\ 12}}^{L} \, I_{L}^{(i)} \right) \tag{4.2a}$$

$$V_{L}^{(k)} = \sum_{i=1}^{N} \left(Z_{\substack{ik \\ 21}}^{L} \, I_{in}^{(i)} - Z_{\substack{ik \\ 22}}^{L} \, I_{L}^{(i)} \right) \tag{4.2b}$$

$$V_{L}^{(k)} = \sum_{i=1}^{N} \left(Z_{\substack{ik \\ 11}}^{X_L} \, I_{L}^{(i)} - Z_{\substack{ik \\ 12}}^{X_L} \, I_{M}^{(i)} \right) \tag{4.2c}$$

$$V_{M}^{(k)} = \sum_{i=1}^{N} \left(Z_{\substack{ik \\ 21}}^{X_L} \, I_{L}^{(i)} - Z_{\substack{ik \\ 22}}^{X_L} \, I_{M}^{(i)} \right) \tag{4.2d}$$

$$V_{M}^{(k)} = \sum_{i=1}^{N} \left(Z_{\substack{ik \\ 11}}^{X_R} \, I_{M}^{(i)} - Z_{\substack{ik \\ 12}}^{X_R} \, I_{R}^{(i)} \right) \tag{4.2e}$$

$$V_{R}^{(k)} = \sum_{i=1}^{N} \left(Z_{\substack{ik \\ 21}}^{X_R} \, I_{M}^{(i)} - Z_{\substack{ik \\ 22}}^{X_R} \, I_{R}^{(i)} \right) \tag{4.2f}$$

$$V_{R}^{(k)} = \sum_{i=1}^{N} \left(Z_{\substack{ik \\ 11}}^{R} \, I_{R}^{(i)} - Z_{\substack{ik \\ 12}}^{R} \, I_{out}^{(i)} \right) \tag{4.2g}$$

$$V_{out}^{(k)} = \sum_{i=1}^{N} \left(Z_{\substack{ik \\ 12}}^{R} \, I_{R}^{(i)} - Z_{\substack{ik \\ 22}}^{R} \, I_{out}^{(i)} \right) \tag{4.2h}$$

$$V_{out}^{(k)} = Z_{0}^{(k)} \, I_{out}^{(k)} \tag{4.3}$$

In these expressions, the indexes i and k represent the modes of the waveguide ($k = 1 \dots N$). See Appendix A for a description of the indexing of matrices. The excitation of the system is given by the vector

$$\vec{V}_{exc} = [V_g \; 0 \; \dots \; 0] \tag{4.4}$$

where a single-mode RF input signal has been used. This set of equations constitutes a linear system of equations, which can be represented in terms of matrices as follows:

$$\begin{pmatrix} \vec{V}_{exc} \\ \vec{0} \\ \vec{0} \\ \vec{0} \\ \vec{0} \end{pmatrix} = \begin{pmatrix} \vec{I}_{in} \\ \vec{I}_{L} \\ \vec{I}_{M} \\ \vec{I}_{R} \\ \vec{I}_{out} \end{pmatrix} \cdot \begin{pmatrix} [Z_0] + [Z]_{11}^{L} & -[Z]_{12}^{L} & 0 & 0 & 0 \\ -[Z]_{21}^{L} & [Z]_{22}^{L} + [Z]_{11}^{X_L} & -[Z]_{12}^{X_L} & 0 & 0 \\ 0 & -[Z]_{21}^{X_L} & [Z]_{22}^{X_L} + [Z]_{11}^{X_R} & -[Z]_{12}^{X_R} & 0 \\ 0 & 0 & -[Z]_{21}^{X_R} & [Z]_{22}^{X_R} + [Z]_{11}^{R} & -[Z]_{12}^{R} \\ 0 & 0 & 0 & -[Z]_{21}^{R} & [Z]_{22}^{R} + [Z_0] \end{pmatrix}^{\top} \tag{4.5}$$

On the other hand, the matrix $[Z_0]$, which is represented in Fig. 4.13(a), can be defined as

$$[Z_0] = \vec{Z}_0 \cdot [U] \tag{4.6}$$

$[U]$ being the unitary matrix and $\vec{Z}$ a vector containing all the modal characteristic impedances. The solution of (4.5) are the modal currents of the equivalent circuit, from which the modal voltages can be directly derived using (4.1), (4.2) and (4.3).

4.5.3 Equivalent circuit of a multipactor discharge within an infinite waveguide

The motion of the electrons of a multipactor current occurring within a microwave component is governed by the RF electric and magnetic field (Lorentz's force), resulting in three-dimensional trajectories. For the case of a rectangular waveguide excited by the fundamental TE_{10} mode, the main electric current component is oriented in the direction of the electric field [23]. In the present approach of the problem, only such contribution is considered. Thus, the multipactor discharge can be treated as a current-filament oriented in the direction of the fundamental mode electric field, like in Sec. 3.4. This technique is independent of the model used to describe the multipactor wire-current. Simple analytical as well as more realistic stochastic models can be considered in the frame of this procedure.

On the other hand, a Fourier analysis of the multipactor wire-current allows to obtain an equivalent representation of the discharge in terms of time-harmonic current-filaments, despite the stochastic nature of the multipactor phenomenon. In the context of the classical microwave network theory, a time-harmonic current-filament radiating within an infinite waveguide can be modelled as a set of current and voltage sources [46], as shown in Fig. 4.14. The introduction of these sources into the equivalent multimode network of a microwave structure will allow to study the propagation of the electromagnetic energy radiated by a multipactor discharge in such structure. The equations of the circuit shown in Fig. 4.14 are:

$$V_b^{TE_k} = V_a^{TE_k} \tag{4.7a}$$

$$V_b^{TM_k} = V_a^{TM_k} + v^{TM_k} \tag{4.7b}$$

$$I_b^{TE_k} = I_a^{TE_k} - i^{TE_k} \tag{4.7c}$$

$$I_b^{TM_k} = I_a^{TM_k} - i^{TM_k} \tag{4.7d}$$

4.5.4 Introduction of the multipactor discharge in the component

The combination of the networks shown in Figs. 4.12 and 4.14 allows to study the electromagnetic radiation of a time-harmonic wire-current throughout a microwave passive component. A representation of the resulting multimode network is given in Fig. 4.15. In this figure, the modal voltage $\vec{V}_M$ has been replaced with $\vec{V}_{M_L}$ and $\vec{V}_{M_R}$ due to the voltage generators of TM modes in the wire-current element. A system of linear equations describing the problem can be derived by using (4.1), (4.2), (4.3) and (4.7). This procedure is undertaken for the particular case studied in the following section, without losing generality.

4.6 Application example

4.6.1 Introduction

The preceeding technique is now applied to the study of the multipactor effect within the RF component used in the laboratory test campaign. It is an E-plane rectangular waveguide transfomer, already described in Sec. 4.2.3.

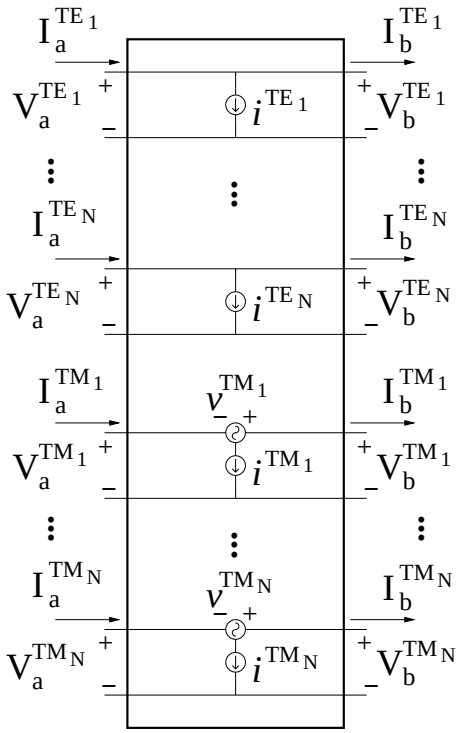

Figure 4.14: Fullwave representation of a time-harmonic transverse wire-current within an uniform cross-section waveguide. An equivalent circuit is obtained as a set of time-harmonic current and voltage sources.

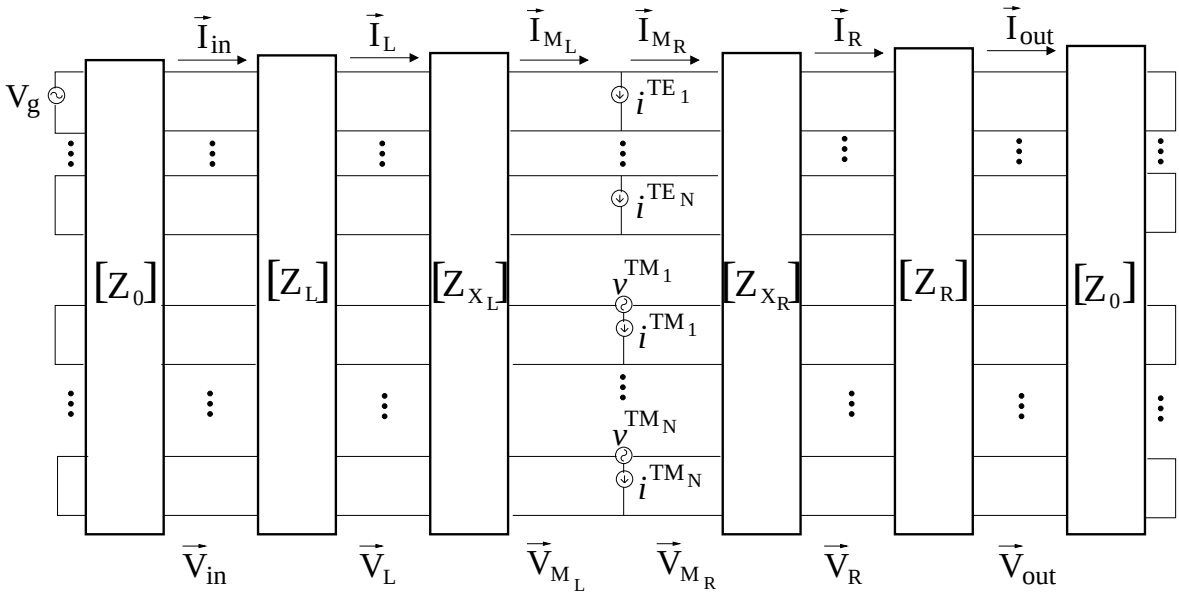

Figure 4.15: Fullwave representation of a time-harmonic transverse wire-current within a microwave passive component under single-mode excitation.

4.6.2 Full-wave characterization of the problem

The waveguide section L_4 (see Fig 4.5) can be considered the area of the component most susceptible to suffer from multipactor discharges due to the reduced height of the guide. The distribution of the electric field in this waveguide section has been analyzed, concluding that the maximum intensity will be located on the axis $x = a/2$, under the excitation of the fundamental mode TE_{10}. In this component, $a = 19.05$ mm. The electric field intensity on this axis has been computed at the work frequency (see Fig. 4.16) in order to determine the point of maximum intensity, here named z'. Based on multipactor physics, discharges should take place around this point.

Following the above considerations, a multipactor discharge radiating within the RF transformer can be considered as a uniform current-filament centered on the x-axis and pointed in the y-direction (see Fig 4.5). A possible expression for the current-filament element $\vec{J}$ in the frequency-domain is:

$$\vec{J}(x,y,z,f) \;=\; \tilde{I}_{MP}(f)\;\delta\left(x-\frac{a}{2}\right)\;\delta(z-z')\;\hat{y} \tag{4.8}$$

where $\tilde{I}_{MP}(f)$ is the frequency-domain multipactor current intensity, which will be analyzed in Sec. 4.6.3. The representation of a source current distribution like $\vec{J}$ contained in a bounded region in terms of a complete set of electric modes reduces the description of the source to the determination of the modal current amplitudes, χ_{mn} [46]:

$$\vec{J} = \sum_m \sum_n \chi_{mn}^{TE}\;\vec{e}_{mn}^{TE} \;+\; \chi_{mn}^{TM}\;\vec{e}_{mn}^{TM} \tag{4.9}$$

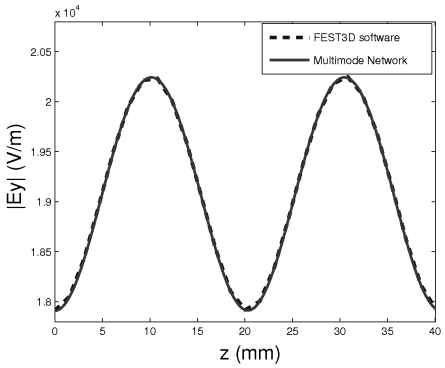

Figure 4.16: Electric field intensity $|E_y|$ along the length of the waveguide section 4 at $x = a/2$ and $y = b/2$ (see Fig 4.5). Plot computed with FEST3D and based on the transmission lines circuit.

where mn stand for modal index pairs ($k = (mn)$); $\vec{e}_{mn}$ are the well-known normalized electric vector modal functions of the rectangular waveguide [46]. The modal amplitudes are found out after applying orthogonality conditions in (4.9) for the particular case of the multipactor current given by (4.8)

$$\chi_{mn}^{TE} = \sqrt{\frac{2b}{a}} \sin\left(\frac{m\pi}{2}\right) \delta(n)\, \tilde{I}_{MP}(f) \tag{4.10a}$$

$$\chi_{mn}^{TM} = 0 \tag{4.10b}$$

An equivalent circuit for field sources within waveguides was presented in Sec. 4.5.3. For the present case, the amplitude of the voltage and current generators in that circuit are

$$i_k^{TE} = \chi_k^{TE} \tag{4.11a}$$

$$i_k^{TM} = \chi_k^{TM} \tag{4.11b}$$

$$v_k^{TM} = 0 \tag{4.11c}$$

Note that the amplitude of the TM generators is zero, what simplifies the characterization of multipactor discharges to a set of shunt current generators at TE modes. Thus, the set of equations

(4.2) should be modified to include the effect of such generators, as

$$V_{in}^{(k)} = \sum_{i=1}^{N} \left(Z_{\substack{ik \\ 11}}^{L} I_{in}^{(i)} - Z_{\substack{ik \\ 12}}^{L} I_{L}^{(i)} \right) \tag{4.12a}$$

$$V_{L}^{(k)} = \sum_{i=1}^{N} \left(Z_{\substack{ik \\ 21}}^{L} I_{in}^{(i)} - Z_{\substack{ik \\ 22}}^{L} I_{L}^{(i)} \right) \tag{4.12b}$$

$$V_{L}^{(k)} = \sum_{i=1}^{N} \left(Z_{\substack{ik \\ 11}}^{X_L} I_{L}^{(i)} - Z_{\substack{ik \\ 12}}^{X_L} I_{M_L}^{(i)} \right) \tag{4.12c}$$

$$V_{M}^{(k)} = \sum_{i=1}^{N} \left(Z_{\substack{ik \\ 21}}^{X_L} I_{L}^{(i)} - Z_{\substack{ik \\ 22}}^{X_L} I_{M_L}^{(i)} \right) \tag{4.12d}$$

$$V_{M}^{(k)} = \sum_{i=1}^{N} \left(Z_{\substack{ik \\ 11}}^{X_R} I_{M_R}^{(i)} - Z_{\substack{ik \\ 12}}^{X_R} I_{R}^{(i)} \right) \tag{4.12e}$$

$$V_{R}^{(k)} = \sum_{i=1}^{N} \left(Z_{\substack{ik \\ 21}}^{X_R} I_{M_R}^{(i)} - Z_{\substack{ik \\ 22}}^{X_R} I_{R}^{(i)} \right) \tag{4.12f}$$

$$V_{R}^{(k)} = \sum_{i=1}^{N} \left(Z_{\substack{ik \\ 11}}^{R} I_{R}^{(i)} - Z_{\substack{ik \\ 12}}^{R} I_{out}^{(i)} \right) \tag{4.12g}$$

$$V_{out}^{(k)} = \sum_{i=1}^{N} \left(Z_{\substack{ik \\ 12}}^{R} I_{R}^{(i)} - Z_{\substack{ik \\ 22}}^{R} I_{out}^{(i)} \right) \tag{4.12h}$$

$$i_k = I_{M_L}^{(k)} - I_{M_R}^{(k)} \tag{4.13}$$

Or, equivalently, by the next system of equations

$$\begin{pmatrix} \vec{V}_{exc} \\ \vec{0} \\ \vec{0} \\ \vec{0} \\ \vec{0} \\ \vec{I}_{MP} \end{pmatrix} = \begin{pmatrix} \vec{I}_{in} \\ \vec{I}_{L} \\ \vec{I}_{M_L} \\ \vec{I}_{M_R} \\ \vec{I}_{R} \\ \vec{I}_{out} \end{pmatrix} \cdot \begin{pmatrix} [Z_0] + [Z]_{11}^{L} & -[Z]_{12}^{L} & 0 & 0 & 0 & 0 \\ -[Z]_{21}^{L} & [Z]_{22}^{L} + [Z]_{11}^{X_L} & -[Z]_{12}^{X_L} & 0 & 0 & \\ 0 & -[Z]_{21}^{X_L} & [Z]_{22}^{X_L} & [Z]_{11}^{X_R} & -[Z]_{12}^{X_R} & 0 \\ 0 & 0 & 0 & -[Z]_{21}^{X_R} & [Z]_{22}^{X_R} + [Z]_{11}^{R} & -[Z]_{12}^{R} \\ 0 & 0 & 0 & 0 & -[Z]_{21}^{R} & [Z]_{22}^{R} + [Z_0] \\ 0 & 0 & \vec{1} & -\vec{1} & 0 & 0 \end{pmatrix}^{\top} \tag{4.14}$$

where the vector $\vec{I}_{MP}$ is defined as

$$\vec{I}_{MP} = \left[i_1^{TE} \ \ldots \ i_N^{TE} \ i_1^{TM} \ \ldots \ i_N^{TM} \right] \tag{4.15}$$

and $\vec{1} = \left[1 \ \ldots \ 1 \right]$.

4.6.3 Simulation

A simulation of a multipactor discharge ocurring within a rectangular waveguide was performed following the model proposed in [63]. The main physical effects involved in a multipactor event are

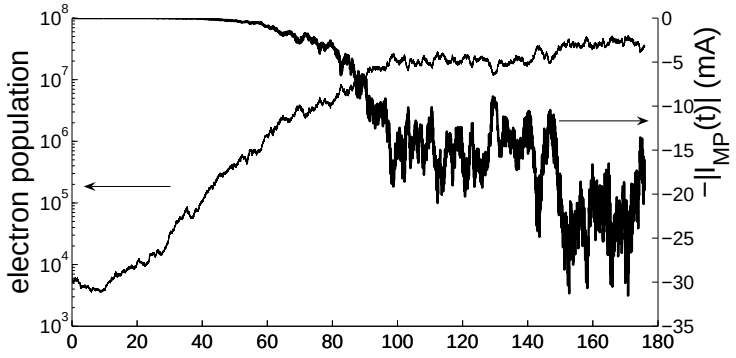

Figure 4.17: PIC simulation of the time-domain evolution of the electron population and current intensity for a multipactor discharge inside the central section of the transformer. The saturation of the discharge produced by the space charge is reached after 150 ns.

simulated in this PIC model, finally obtaining a representation in the time-domain of the discharge. In Fig. 4.17, a computation of the time evolution of electrons population during the multipactor discharge, as well as the time-domain multipactor current $I_{MP}(t)$, are shown. The spectrum is afterwards computed by a standard Fourier transform algorithm, obtaining $\tilde{I}_{MP}(f)$.

On the other hand, the microwave structure has been rigurously characterized as a multi-port circuit following the technique previously presented. The electromagnetic software tool FEST3D was used to obtain the generalized impedance matrices $[Z_L]$ and $[Z_R]$, involving 100 accesible modes, 1200 localized modes, and 200 basis functions in the computation (for more information about the meaning of these parameters, the reader is referred to [67]). The coherence of the network regarding power transfer and conservation has been satisfactorily checked following the principles exposed in Appendix A. Furthermore, a FEST3D model of the component was used to validate the scattering response of the network.

4.6.4 Comparison of results

An estimation of the power radiated by a multipactor discharge induced within the WR-75 transformer has been computed using the fullwave model presented above. On the other hand, the power radiated during a multipactor event was measured at different frequency points in the laboratory test. A comparison of both results is given in Fig 4.18. The agreement obtained in the results suggests that the present model is a suitable technique for the study of multipactor within RF components.

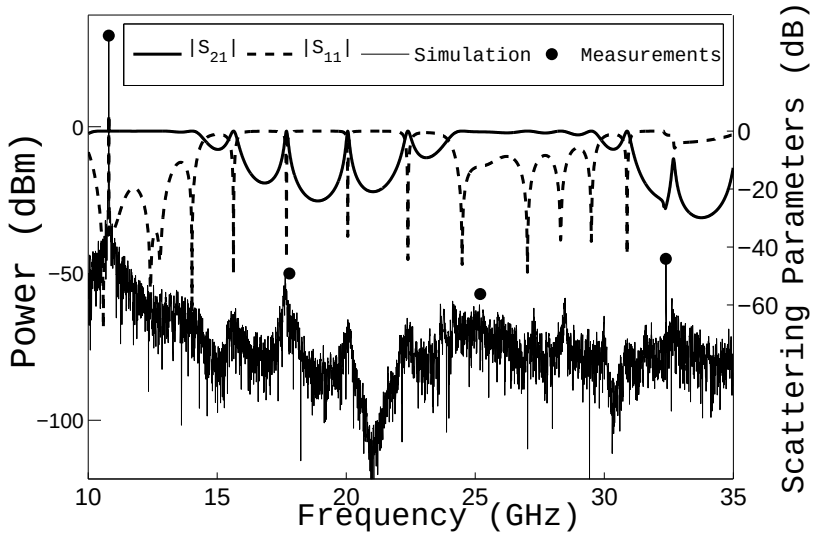

Figure 4.18: Power spectrum of the transmitted signal at the output-port of the transformer during a multipactor event. Comparison between experimental and theoretical results.

Chapter 5

Radiation of charges within an infinite waveguide for particle accelerators applications

5.1 Introduction

The electromagnetic radiation of a charge particle as well as a charge distribution within a waveguide region or a resonator cavity has been extensively treated in the literature. Thus, there are many articles focused on this area. Several authors have investigated the radiation of electron beams in metallic waveguides and cavities for the study of RF photo-injectors [1, 2]. Other classical problem related with this topic is the evaluation of the wakefields. The rigorous analysis of the wakefields is a non-trivial issue, and critically depends on the geometry and materials of the accelerator structure. In most of the current models found in the technical literature, the particles move linearly at constant velocity [3, 4, 5, 6, 7, 8, 9, 11, 12, 13, 14]. The study of the radiated fields left behind by a charged particle is particularly important because they influence the motion of the charged particles that follow them. Different techniques combining the solutions of Maxwell's equations in both time and frequency domains have been employed in the aforementioned contributions.

Most particle accelerators employ RF fields to accelerate the particles [68, 69, 70]. The beam in these cases consists of short bunches with a length that is small compared with the RF wavelength, in order to provide a constant impulse to the particles during the beam length. An electromagnetic field is then used to focus the beams for reducing the lost of particles due to spreading. Beams must travel in high vacuum to avoid the scattering of particles on the residual gas molecules. The vacuum chamber consists of a metallic pipe. Indeed, a metallic surface is preferred because it conducts electric field. Moreover, the high electron absorption rate of metals minimizes the formation of electron clouds in the surroundings of sensitive points. Charged particles generate electromagnetic fields in their travel throughout the waveguide. Such fields interact with travelling-behind particles, disturbing their motion and, consequently, the beam distribution. The transverse component of the field makes the beam aperture larger, what leads to particle losses and beam instabilities; on the other hand, the longitudinal field produces variations in the velocity of particles, affecting to the charges distribution.

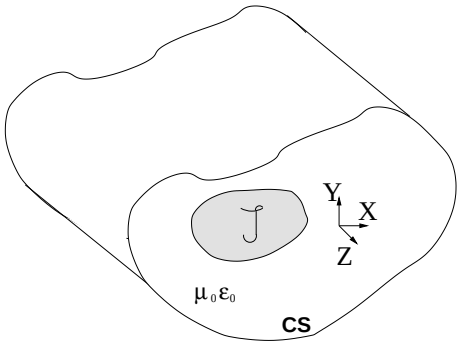

Figure 5.1: Schematic of an arbitrary charge distribution moving inside a uniform arbitrarily-shaped cross-section waveguide region.

This last effect is critical for the accelerating process of the machine, due to the high synchronization required between beams and the phase of the RF supply. This interaction of fields and particles can be characterized by wakefields and coupling impedances [3, 68, 69, 70, 71]. Both parameters are defined as the integral electromagnetic force along a particle trajectory, the former studying the problem in the time-domain and the second in the frequency-domain. Concerning the effects such fields produce on the vacuum chamber, it is of interest to mention the heating of the structure, which may damage some components as well as increase the levels of residual gas due to evaporation. As a consequence of the presence of lost particles in a vacuum enviroment that is being excited by an electromagnetic field, the multipactor effect can be ignited in particular regions of the structure. The wakefield problem has been traditionally studied for ultrarelativistic particles. In that case, the fields radiated by a particle are confined to the transverse plane [72, 73]; this fact allows to prevent wakefields within uniform waveguides by ensuring that the propagation time of the field from the beam to the walls and back is greater than the crossing time of the beam through such plane. Then it is more useful to study the wakefield effect in the presence of wall discontinuities, because they can turn off the electromagnetic field towards the beam. The formulation here presented can be applied to non-relativistic particles, and hence the wakefield effect is studied in the context of uniform waveguides.

A technique for the accurate computation of the time-domain electromagnetic fields radiated by a charged particle or an arbitrarily-shaped charged distribution moving within a waveguide region is presented. Based on the transformation (by means of the standard Fourier analysis) of the time-varying current density of the analyzed problem to the frequency domain one, the resulting frequency-domain equivalent current is further convolutioned with the dyadic electric and magnetic Green's functions. Finally, frequency-domain electric and magnetic fields are retransformed to the time-domain, just obtaining the total fields emitted by the charged distribution. Several examples of charged particles moving in the axial as well as transverse direction illustrate the presented algorithm.

5.2 Wakefield definition

The electromagnetic fields created by particles in motion induce surface charges and currents in the walls of the beampipe, which act back on particles and beams travelling behind. The trajectory and

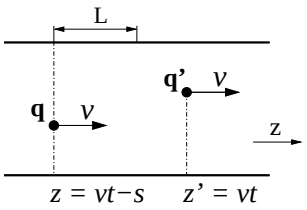

Figure 5.2: Two charges travelling at constant velocity $\vec{v}$ within a hollow waveguide. The charges are separated by a longitudinal length s.

the velocity of travelling particles are modified by the presence of such surface charges, thus resulting in bunch instabilities. It is a convention for relativistic electron beams to know these space forces as wakefields, although they also propagate in front of the source charge for $v < c$. The wakefield effect is analysed in the frame of the actual work by means of the definition of a δ-function wake potential. This function characterizes the net impulse delivered from a unit-strength source charge to a trailing charge along an homogeneous waveguide section of length L. Both charges travel at the same velocity v along the same or parallel trajectories, spaced in the axial direction by a distance s (s can be greater or smaller than L). The δ-function wake potential has been defined as in section 11.3 of [68], here adapted to particles with a velocity below the limit c and travelling within a lossless waveguide:

$$\vec{w}_\perp(\vec{r},\vec{r}',s) = \frac{1}{q}\int_0^L \vec{\mathcal{E}}_\perp\left(\vec{r},t=\frac{z+s}{v}\right)dz + \frac{v\,\mu_0}{q}\int_0^L \hat{z}\times\vec{\mathcal{H}}_\perp\left(\vec{r},t=\frac{z+s}{v}\right)dz \tag{5.1a}$$

$$w_z(\vec{r},\vec{r}',s) = -\frac{1}{q}\int_0^L \mathcal{E}_z\left(\vec{r},t=\frac{z+s}{v}\right)dz \tag{5.1b}$$

where w_z and $\vec{w}_\perp$ are the longitudinal and transverse δ-function wake potentials.

5.3 Analysis of arbitrarily shaped homogeneous waveguides by the BI-RME technique

In order to compute the electromagnetic fields inside hollow arbitrary waveguides, the Boundary integral-resonant mode expansion (BI-RME) method [45] has been used. This modal method efficiently characterizes such arbitrarily-shaped waveguides thanks to the solution of integral equations resulting into eigenvalue problems. The main advantage of this method is the use of an exact kernel defined by means of dyadic Green's functions expressed in terms of fast converging series. The classical implementation of the method consider an arbitrary profile CS, uniform in the longitudinal direction, composed of smaller straight arcs and completely enclosed within a rectangular waveguide of cross section Ω (see Fig. 5.3). Recently this method has been revisited and extended in order to cope with arbitrary profiles defined by the combination of linear, circular and/or elliptical segments [74]. In this section we only outline the basics of this extended technique.

The electric field at a generic observation point $\vec{r}$ inside Ω can be obtained by

$$\vec{E}(\vec{r},\omega) = -i\eta k\int_{CS}\overline{\overline{G}}^{\square}_{e}(\vec{r},\vec{s}',k)\cdot\vec{J}_{CS}(l')\,dl' \tag{5.2}$$

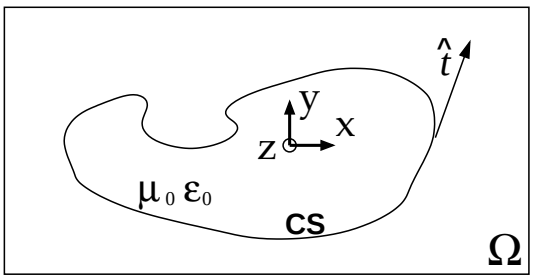

Figure 5.3: Geometry of the BI-RME problem. The arbitrary boundary CS is embedded in a rectangular domain Ω.

where $\vec{s}'$ indicates a source point on the arbitrary contour CS defined by the unitary tangent vector $\hat{t}$ and a suitable abscisa l', $\eta = \sqrt{\mu/\epsilon}$ is the characteristic impedance, $k = \omega\sqrt{\mu\epsilon}$ is the wavenumber, $\overline{\overline{G}}_e^{\,\square}$ is the two- dimensional dyadic Green's function of the electric type for the two-dimensional resonator of cross section Ω and $\vec{J}_{CS}$ is the current density on the contour CS. The general expression of $\overline{\overline{G}}^{\,\square}\,e$ for a rectangular cross section Ω is [75]

$$\begin{aligned}\overline{\overline{G}}^{\,\square}\,e\left(\vec{r},\vec{s}',k\right) &= -\frac{1}{k^2}\nabla\nabla' g\left(\vec{r},\vec{s}'\right) + \overline{\overline{G}}_{st}\left(\vec{r},\vec{s}'\right) + \sum_m \frac{k^2}{\left(k_{t_m}^{\square}\right)^2\left(\left(k_{t_m}^{\square}\right)^2 - k^2\right)}\vec{e}_m^{\,\square TE}\left(\vec{r}\right)\vec{e}_m^{\,\square TE}\left(\vec{s}'\right) \\ &+ \hat{z}\hat{z}g\left(\vec{r},\vec{s}'\right) + \hat{z}\hat{z}\sum_m \frac{k^2}{\left(k_{t_m}^{\square}\right)^2\left(\left(k_{t_m}^{\square}\right)^2 - k^2\right)}e_{z_m}^{\square TM}\left(\vec{r}\right)e_{z_m}^{\square TM}\left(\vec{s}'\right) \qquad (5.3)\end{aligned}$$

where g is the rapidly converging scalar two-dimensional Green's function satisfying Dirichlet's boundary condition; $\overline{\overline{G}}_{st}$ is the rapidly converging solenoidal dyadic normal to the boundary [45]; $k_{t_m}^{\square}$ and $\vec{e}_m^{\,\square TE}\left(\vec{r}\right)$ are the transverse wavenumber and the transverse modal vector of the mth TE mode of the rectangular waveguide Ω, respectively. Finally $e_{z_m}^{\square TM}$ is the axial component of the mth TM electric modal vector.

Splitting $\overline{\overline{G}}_e^{\,\square}$ and $\vec{J}_{CS}$ into its transverse and longitudinal components, and imposing the corresponding boundary conditions on CS for TE and TM modes, which are

$$\vec{E}_{\perp}^{TE}\left(\vec{r}\right)\cdot\hat{t}\left(l\right) = 0 \qquad (5.4a)$$

$$\vec{E}_z^{TM}\left(\vec{r}\right) = 0 \qquad (5.4b)$$

we obtain the next integral equations

$$\frac{1}{k^2}\frac{\partial}{\partial l}\int_{CS} g\left(\vec{r},\vec{s}'\right)\frac{\partial J_{\perp}\left(l'\right)}{\partial l'}dl' + \int_{CS}\hat{t}\left(l\right)\cdot\overline{\overline{G}}_{st}\left(\vec{r},\vec{s}'\right)\cdot\hat{t}\left(l'\right)J_{\perp}\left(l'\right)dl' + \sum_m \frac{\hat{t}\left(l\right)\cdot\vec{e}_m^{\,\square TE}\left(\vec{r}\right)}{\left(k_{t_m}^{\square}\right)^2}a_m = 0 \qquad (5.5a)$$

$$\int_{CS} g\left(\vec{r},\vec{s}'\right)\mathrm{J}_z\left(l'\right)dl' + \sum_m \frac{e_{z_m}^{\square TM}\left(\vec{r}\right)}{\left(k_{t_m}^{\square}\right)^2}a'_m = 0 \qquad (5.5b)$$

where the following amplitudes have been defined:

$$a_m = \frac{k^2}{\left(k_{t_m}^{\square}\right)^2 - k^2} \int_{CS} \vec{e}_m{}^{\square TE}\left(\vec{s}\,'\right) \cdot \hat{t}\left(l'\right) J_{\perp}\left(l'\right) dl' \tag{5.6a}$$

$$a'_m = \frac{k^2}{\left(k_{t_m}^{\square}\right)^2 - k^2} \int_{CS} e_{z_m}^{\square TM}\left(\vec{s}\,'\right) J_z\left(l'\right) dl' \tag{5.6b}$$

The next step in the BI-RME method is the discretization of the problem:

$$J_z\left(l'\right) = \sum_{n=1}^{N} b'_n u_n\left(l'\right) \tag{5.7a}$$

$$J_{\perp}\left(l'\right) = \sum_{n=1}^{N} b_n v_n\left(l'\right) \tag{5.7b}$$

where the basis (u and v) and testing (b and b') functions are chosen to be overlapping piece-wise parabolic splines. Applying the Galerkin approach of the Method of Moments [76], the following general eigenvalue problem is obtained for the TE case

$$\left\{ \begin{bmatrix} \mathbf{U} & \mathbf{0}^T \\ \mathbf{0} & \mathbf{C} \end{bmatrix} - k^2 \begin{bmatrix} \mathbf{D} & \vec{r}^{\,T} \\ \vec{r} & \mathbf{L} \end{bmatrix} \right\} \begin{bmatrix} \mathbf{a} \\ \mathbf{b} \end{bmatrix} = \mathbf{0} \tag{5.8}$$

and the following standard eigenvalue problem can be formulated for the TM case

$$\begin{aligned} \left(\mathbf{D}' - \mathbf{R}'^{T} \cdot \mathbf{L}'^{-1} \cdot \mathbf{R}'\right) \mathbf{a}' &= k'^{-2} \mathbf{a}' \\ \mathbf{b}' &= -\mathbf{L}'^{-1} \cdot \mathbf{R}' \cdot \mathbf{a}' \end{aligned} \tag{5.9}$$

where the expression of the submatrices are detailed in [74]. The solution of (5.8) and (5.9) provides as eigenvalues the cut-off wavenumbers $k_{t_i}^{\square}$, and as eigenvectors the modal expansion coefficients defined as ($\mathbf{a}$, $\mathbf{a}'$) in (5.6) and the amplitudes of the transverse ($\mathbf{b}$) and longitudinal ($\mathbf{b}'$) components of the unknown current density $\vec{J}_{CS} = J_{\perp}\hat{t} + J_z\hat{z}$.

Once the TE and TM problems are solved, the electromagnetic fields of the qth TE mode inside the arbitrarily shaped waveguides are

$$\begin{aligned} \vec{e}_q^{\,TE}(\vec{r}) &= \frac{1}{k_{t_q}^{\square}} \sum_{n=1}^{N} b_n^q \nabla_{\perp} \int_{CS} g\left(\vec{r}, \vec{s}\,'\right) \frac{\partial v_n\left(l'\right)}{\partial l'} dl' \\ &+ k_{t_q}^{\square} \sum_{n=1}^{N} b_n^q \int_{CS} \overline{\overline{G}}_{st}\left(\vec{r}, \mathbf{s}'\right) \cdot \hat{t}\left(l'\right) v_n\left(l'\right) dl' + k_{t_q}^{\square} \sum_{m} \frac{\vec{e}_m{}^{\square TE}\left(\vec{r}\right)}{\left(k_{t_m}^{\square}\right)^2} a_m^q \end{aligned} \tag{5.10a}$$

$$\vec{h}_q^{\,TE}(\vec{r}) = \hat{z} \times \vec{e}_q^{\,TE}(\vec{r}) \tag{5.10b}$$

$$h_{zq}^{TE}(\vec{r}) = \frac{1}{k_{t_q}^{\square}} \nabla_{\perp} \cdot \left(\hat{z} \times \vec{e}_q^{\,TE}(\vec{r})\right) = \frac{1}{k_{t_q}^{\square}} \left(\frac{\partial\, e_{xq}^{TE}(\vec{r})}{\partial y} - \frac{\partial\, e_{yq}^{TE}(\vec{r})}{\partial x} \right) \tag{5.10c}$$

and the electromagnetic fields of the qth TM mode inside the arbitrarily shaped waveguides are

$$\vec{e}_q^{\,TM}(\vec{r}) = -\sum_{n=1}^{N} b_n^{'q} \int_{CS} \nabla_\perp g\left(\vec{r},\vec{s}\,'\right) u_n\left(l'\right) dl' + \sum_m \frac{a_m'^q}{\left(k_{t_m}^{\square}\right)^2} \vec{e}_m^{\,\square TM}(\vec{r}) \tag{5.11a}$$

$$\vec{h}_q^{\,TM}(\vec{r}) = \hat{z} \times \vec{e}_q^{\,TM}(\vec{r}) \tag{5.11b}$$

$$e_{zq}^{TM}(\vec{r}) = k_{t_q}^{\square} \sum_{n=1}^{N} b_n{}' q \int_{CS} g\left(\vec{r},\vec{s}\,'\right) u_n\left(l'\right) dl' + k_{t_q}^{\square} \sum_m \frac{e_{z_m}^{\square TM}(\vec{r})}{\left(k_{t_m}^{\square}\right)^2} a_m'^q \tag{5.11c}$$

5.4 Punctual charge travelling within an homogeneous infinite waveguide

5.4.1 Constant velocity motion

As already mentioned, a particle accelerator structure basically consistes of a waveguide circuit alternating accelerating cavities and thru-sections. The particles, packed in bunches, are injected into the structure and accelerated up to relativistic velocities by the action of the accelerating cavities. In the present section, the electromagnetics of such particles within the beampipe of a particle accelerator or within a generic homogeneous waveguide are discussed. Since the particles velocity is unchanged between successive accelerating cavities, this subject can be approached as the study of constant velocity particles travelling along an infinite homogeneous waveguide. Fig. 5.4 depicts this scenario. In the figure, the guide is uniform along the direction of propagation, which coincides with the z axis. Losses are not considered, and the guide is vacuum filled, ε_0 being the electric permittivity of free space and μ_0 the magnetic permeability of free space; speed of ligth is given by $c = 1/\sqrt{\mu_0 \varepsilon_0}$. There is a source particle carrying charge q uniformly moving in the z direction with constant velocity v; we assume that $v \geq 0$. The charge and current densities of this charge are represented by [13, 77]

$$\rho(\vec{r}\,',t) = q\,\delta(x'-x_0)\,\delta(y'-y_0)\,\delta(z'-v\,t) \tag{5.12a}$$

$$\vec{\mathcal{J}}(\vec{r}\,',t) = \rho(\vec{r}\,',t)\,v\,\hat{z} \tag{5.12b}$$

respectively, where the cartesian coordinates (x_0, y_0) define the transverse position of the particle. In this context, the vector position is divided in its transverse and axial components, $\vec{r} = \vec{r}_\perp + z\,\hat{z}$. Note that both densities are related by the continuity equation [73]. The Green's function formalism presented in Chapter 2 is a suitable tool for obtaining electromagnetic fields from their sources, expressed in the frequency-domain. Thus, it is necessary to evaluate the Fourier transform (see Appendix B.1) of the current density:

$$\vec{J}(\vec{r}\,',\omega) = q\,\delta(x'-x_0)\,\delta(y'-y_0)\;\; e^{-i\omega\,z'/v}\,\hat{z} \tag{5.13}$$

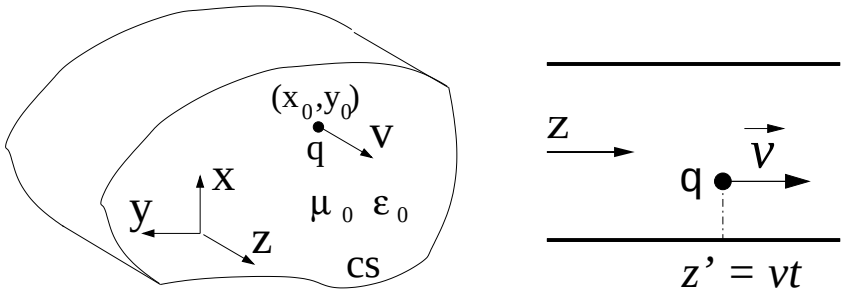

(a) Paraline drawing of the problem. (b) 2D-view of the problem.

Figure 5.4: Schematic of a point charge q travelling at constant velocity $\vec{v}$ throughout a vacuum-filled, hollow waveguide with arbitrary cross-section CS.

where (B.2e) and (B.3a) have been used. The frequency-domain electric $\vec{E}(\vec{r})$ and magnetic $\vec{H}(\vec{r})$ fields are derived applying (5.13) to (2.41):

$$\vec{E}_\perp(\vec{r},\omega) \;=\; -\frac{q\;\; e^{-i\omega\frac{z}{v}}}{v\,\varepsilon_0}\sum_{m=1}^{\infty}\frac{k_{t_m}^2}{k_{z_m}^2-\left(\frac{\omega}{v}\right)^2}\,\vec{e}_{\perp_m}^{TM}(\vec{r}_\perp)\,\phi_m^{TM}(x_0,y_0) \tag{5.14a}$$

$$\vec{E}_z(\vec{r},\omega) \;=\; \frac{q\;\; e^{-i\omega\frac{z}{v}}}{i\,\omega\,\varepsilon_0}\sum_{m=1}^{\infty}\frac{k_{t_m}^4}{k_{z_m}^2-\left(\frac{\omega}{v}\right)^2}\phi_m^{TM}(\vec{r}_\perp)\,\phi_m^{TM}(x_0,y_0)\,\hat{z} \tag{5.14b}$$

$$\vec{H}_\perp(\vec{r},\omega) \;=\; -q\;\; e^{-i\omega\frac{z}{v}}\sum_{m=1}^{\infty}\frac{k_{t_m}^2}{k_{z_m}^2-\left(\frac{\omega}{v}\right)^2}\,\vec{h}_{\perp_m}^{TM}(\vec{r}_\perp)\,\phi_m^{TM}(x_0,y_0) \tag{5.14c}$$

$$\vec{H}_z(\vec{r},\omega) \;=\; 0 \tag{5.14d}$$

The potentials ϕ are defined following (2.13). The Appendix C.1 details the derivation of (5.14). Finally, the time-domain electric and magnetic fields are obtained by means of the standard inverse Fourier transform:

$$\vec{\mathcal{E}}_\perp(\vec{r},t) \;=\; \frac{q\,\gamma}{2\,\varepsilon_0}\sum_{m=1}^{\infty}k_{t_m}\,\vec{e}_{\perp_m}^{TM}(\vec{r}_\perp)\,\phi_m^{TM}(x_0,y_0)\;\; e^{-v\,\gamma\,k_{t_m}|t-z/v|} \tag{5.15a}$$

$$\vec{\mathcal{E}}_z(\vec{r},t) \;=\; -u(t-z/v)\frac{q}{2\,\varepsilon_0}\sum_{m=1}^{\infty}k_{t_m}^2\,\phi_m^{TM}(\vec{r}_\perp)\,\phi_m^{TM}(x_0,y_0)\;\; e^{-v\,\gamma\,k_{t_m}|t-z/v|}\,\hat{z} \tag{5.15b}$$

$$\vec{\mathcal{H}}_\perp(\vec{r},t) \;=\; \frac{q\,v\,\gamma}{2}\sum_{m=1}^{\infty}k_{t_m}\,\vec{h}_{\perp_m}^{TM}(\vec{r}_\perp)\,\phi_m^{TM}(x_0,y_0)\;\; e^{-v\,\gamma\,k_{t_m}|t-z/v|} \tag{5.15c}$$

$$\vec{\mathcal{H}}_z(\vec{r}) \;=\; 0 \tag{5.15d}$$

where $\gamma \equiv 1/\sqrt{1-\beta^2}$ is the relativistic factor (also named Lorentz's factor), $\beta \equiv v/c$ being the velocity in terms of the speed of light in vacuum.

Fig. 5.5 shows the transverse fields (5.15) created by a point charge within a rectangular waveguide. It is worth to analyse these expressions in the case that the particle velocity approaches to the speed

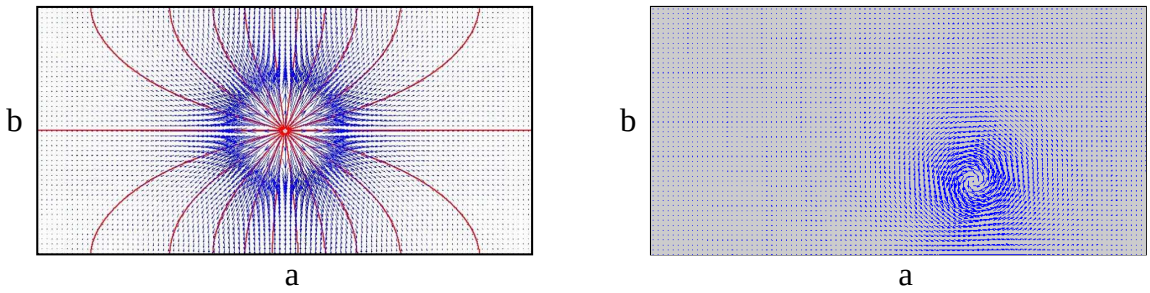

(a) Electric field. (b) Magnetic field.

Figure 5.5: Transverse fields produced by a point charge travelling along a rectangular waveguide at constant velocity.

of light limit. Then, the field power concentrates on a cross-plane comoving with the charge. The transverse components of the fields tend to a Dirac-delta, meanwhile the longitudinal field vanishes:

$$\lim_{v\to c^-} \vec{\mathcal{E}}_\perp(\vec{r}) = \frac{q}{2\ c\ \varepsilon_0}\delta\left(t-\frac{z}{c}\right)\sum_m \frac{\vec{e}_m^{TM}(\vec{r}_\perp)\phi_m^{TM}(x_0,y_0)}{k_{t_m}} \tag{5.16a}$$

$$\lim_{v\to c^-} \vec{\mathcal{E}}_z(\vec{r}) = 0 \tag{5.16b}$$

$$\lim_{v\to c^-} \vec{\mathcal{H}}_\perp(\vec{r}) = \frac{q}{2}\delta\left(t-\frac{z}{c}\right)\sum_m \frac{\vec{h}_m^{TM}(\vec{r}_\perp)\phi_m^{TM}(x_0,y_0)}{k_{t_m}} \tag{5.16c}$$

$$\lim_{v\to c^-} \vec{\mathcal{H}}_z(\vec{r}) = 0 \tag{5.16d}$$

The concentration of fields on the cross-plane shown in (5.16) is a consequence of Lorentz's transformation, which is a determinant factor in relativistic systems. The radiation pattern of a moving charge suffers an aberrating effect related with the velocity of the charge. Following Lorentz's principles such effect is explained by length contraction, and is the cause that the radiation of a free-space moving charge is not a sphere, but a spheroid. Similarly, for waveguide regions, the velocity produces changes on the radiation pattern, as can be seen in Fig. 5.6.

The wakefield of a charge in constant velocity are obtained after applying the definiton given in (5.1) to the field expressions (5.15):

$$\vec{w}_\perp(\vec{r},\vec{r}',s) = \frac{L}{2\ \gamma\ \varepsilon_0}\sum_m k_{t_m}\vec{e}_m^{TM}(\vec{r}_\perp)\phi_m^{TM}(\vec{r}_\perp{}')\ e^{-k_{t_m}\gamma s} \tag{5.17a}$$

$$w_z(\vec{r},\vec{r}',s) = \frac{L}{2\ \varepsilon_0}\sum_m k_{t_m}^2\phi_m^{TM}(\vec{r}_\perp)\phi_m^{TM}(\vec{r}_\perp{}')\ e^{-k_{t_m}\gamma s} \tag{5.17b}$$

Note that last expressions are zero at the physical limit $v \to c^-$ for any separation between charges $s \neq 0$. It means that no wakefield is present in a lossless homogeneous waveguide for charges travelling at the speed of light. In fact, the wakefields appear as a consequence of wall discontinuities, a finite

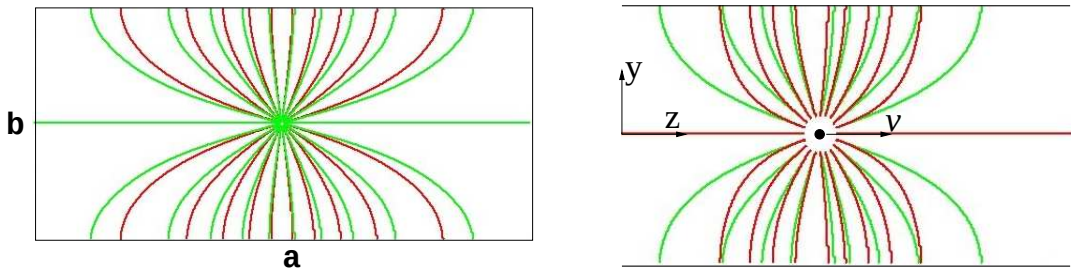

(a) Transverse plane XY.

(b) Longitudinal plane YZ.

Figure 5.6: Effect of charge velocity on the distribution of radiated fields. Electric field lines of a charged particle travelling within a rectangular waveguide of cross-section (a, b) at constant velocity. Results given for two different velocities: $\beta = 0.7$ (green line) and $\beta = 0.9$ (red line).

conductivity of the walls and for velocities less than the ultrarelativistic limit. The expression (5.17) represents the wakefield of a single point charge, therefore it represents the δ-function wake potential. The integrated effect over a finite distribution of charged particles is described by the wake potential. The wake potential of a complete bunch on a single charge can be determined by the convolution of the δ-function wake potential with the charge distribution of the bunch, as will be shown in the next section. Finally, it is also worthly to comment that the effect of the integration length L is trivial in the lossless homogeneous waveguide here considered, due to the lack of variations on the cross-section of the structure. Hence, this parameter appears as a scale factor in (5.17).

The convergence of an expression in infinite series like (5.17) is dominated by the exponential part; the larger the exponent is, the faster the series converges to a realistic solution. This effect is shown in Fig. 5.7, where the wake potential in a waveguide example is approached by different number of terms in the summation expression. The convergence of the series (5.17) is also guaranteed in the limit s approaches to zero, as is demonstrated in [44].

5.5 Bunches of particles

5.5.1 Introduction

As seen in Sec. 5.1, the particles travelling in an accelerator are usually packed into bunches, hence conforming a charge distribution. The punctual charge analysis developed in the previous section is here enlarged to study charge distributions. The problem of a charge bunch can be tackled in two different methods, represented in Fig. 5.8. The first method considers bunches as the sum of particles travelling at different positions with the same velocity. It leads to discrete distributions of particles,

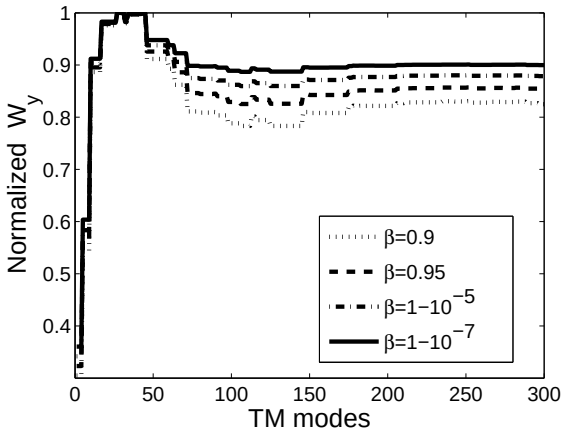

Figure 5.7: Influence of the number of modes used in the solution of the δ-function wake potential (5.17) for a rounded-corner cross-shaped waveguide. The convergence of the wake function series expression is shown for several charge velocities at a fixed distance $s = 5$ mm (the function is normalized for a better display). Note that the number of modes necessary for the convergence of the solution reduces as the velocity increases; an increment in the distance s also produces a similar effect.

whose electromagnetic field can be found as the superposition of single particle fields:

$$\vec{\mathcal{E}}^{(\text{Discrete Bunch})}(\vec{r},t) = \sum_{m=1}^{M} \vec{\mathcal{E}}_m^{(\text{point})}(\vec{r},t) \tag{5.18}$$

$$\vec{\mathcal{H}}^{(\text{Discrete Bunch})}(\vec{r},t) = \sum_{m=1}^{M} \vec{\mathcal{H}}_m^{(\text{point})}(\vec{r},t) \tag{5.19}$$

where M is the number of particles considered in the bunch; $\vec{\mathcal{E}}_m^{(\text{point})}$ and $\vec{\mathcal{H}}_m^{(\text{point})}$ are the electric and magnetic field of a point particle with transverse position (x_m, y_m), shown in (5.15). Hence, the total charge of the bunch is $Q = Mq$. This method is preferable when the number of charges considered M is small, but it losses effectiveness for large populations of particles. Then, it is more convenient to analyze the bunch as a continuous distribution of charge. This second approach to the problem is computationally more effective for large populations. Then, the bunch charge Q is distributed within the beampipe following a given probability density function $f_\rho(\vec{r})$. The results obtained by the first meethod can be seen as particularizations of the continuous distribution method for a certain realization of the population. In the next sections, several continuous distributions of charge are studied. The first case is a generic distribution in the cross-plane, which can be derived directly from the punctual charge problem. In the two following sections, the frequently used Gaussian distribution is analyzed, starting with a distribution on the cross-plane of the beampipe, and then study the case of a 3-dimensional Gaussian bunch.

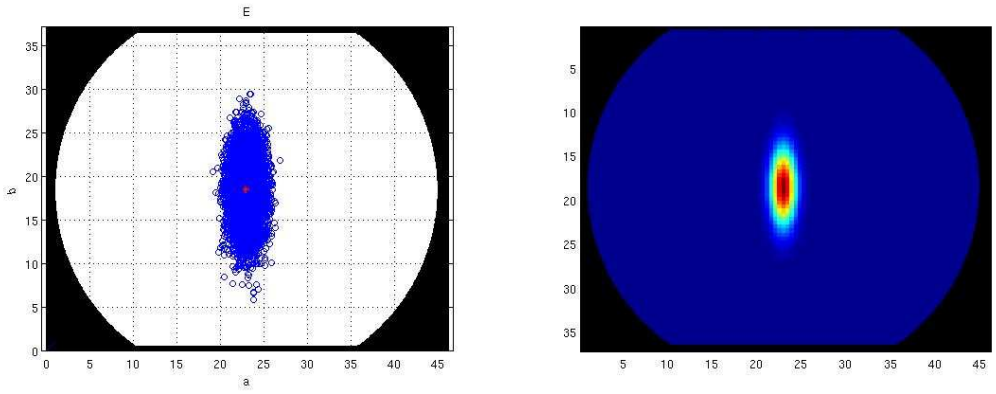

(a) Discrete distribution.

(b) Continuous distribution.

Figure 5.8: 2D-Gaussian distribuion of charge within a beampipe.

5.5.2 2-dimensional continuous distribution of charge

A bunch with total charge Q travels at constant velocity $\vec{v}$ throughout an homogeneous waveguide with cross-section CS. The bunch is supposed to be plane and confined to the cross-plane (2D bunch). Under these conditions, the charge and current densities can be expressed as

$$\rho^{(2\mathrm{D})}(\vec{r}\,',t) \;=\; Q\, f_\rho^{(2\mathrm{D})}(\vec{r}_\perp{}')\,\delta(z'-v\,t) \tag{5.20a}$$

$$\vec{\mathcal{J}}^{(2\mathrm{D})}(\vec{r}\,',t) \;=\; Q\,v\, f_\rho^{(2\mathrm{D})}(\vec{r}_\perp{}')\,\delta(z'-v\,t)\,\hat{z} \tag{5.20b}$$

where $f_\rho^{(2\mathrm{D})}$ indicates the 2-dimensional probability density function of charge. The electromagnetic fields radiated by such charge distribution can be derived following a procedure similar as for the punctual charge case, just substituting the punctual charge density (5.12a) by (5.20a). Hence, the frequency-domain electromagnetic fields are:

$$\vec{E}_\perp^{(2\mathrm{D})}(\vec{r},\omega) \;=\; -\frac{Q\;\; e^{-i\omega\frac{z}{v}}}{v\,\varepsilon_0}\sum_{m=1}^{\infty}\frac{k_{t_m}^2}{k_{z_m}^2-\left(\frac{\omega}{v}\right)^2}\,\vec{e}_{\perp_m}^{TM}(\vec{r}_\perp)\,I_{\perp\perp_m}^{TM} \tag{5.21a}$$

$$\vec{E}_z^{(2\mathrm{D})}(\vec{r},\omega) \;=\; \frac{Q\;\; e^{-i\omega\frac{z}{v}}}{i\,\omega\,\varepsilon_0}\sum_{m=1}^{\infty}\frac{k_{t_m}^4}{k_{z_m}^2-\left(\frac{\omega}{v}\right)^2}\phi_m^{TM}(\vec{r}_\perp)\,I_{\perp\perp_m}^{TM}\,\hat{z} \tag{5.21b}$$

$$\vec{H}_\perp^{(2\mathrm{D})}(\vec{r},\omega) \;=\; -Q\;\; e^{-i\omega\frac{z}{v}}\sum_{m=1}^{\infty}\frac{k_{t_m}^2}{k_{z_m}^2-\left(\frac{\omega}{v}\right)^2}\,\vec{h}_{\perp_m}^{TM}(\vec{r}_\perp)\,I_{\perp\perp_m}^{TM} \tag{5.21c}$$

$$\vec{H}_z^{(2\mathrm{D})}(\vec{r},\omega) \;=\; 0 \tag{5.21d}$$

where the following integral has been defined:

$$I_{\perp\perp_m}^{TM} \;=\; \iint_{CS'} f_\rho^{(2\mathrm{D})}(\vec{r}_\perp{}')\,\phi_m^{TM}(\vec{r}_\perp{}')\,dCS' \tag{5.22}$$

This parameter is a function of the geometry of the waveguide, as well as the charge distribution, so it has to be numerically estimated for non-canonical geometries. Its solution for a punctual charge is $I^{TM}_{\perp\perp_m} = \phi^{TM}_m(x_0, y_0)$, as shown in Appendix C.1. Finally, the fields in the time-domain are:

$$\vec{\mathcal{E}}^{(2\mathrm{D})}_{\perp}(\vec{r}, t) = \frac{Q\,\gamma}{2\,\varepsilon_0} \sum_{m=1}^{\infty} k_{t_m}\, \vec{e}^{TM}_{\perp_m}(\vec{r}_\perp)\, I^{TM}_{\perp\perp_m}\; e^{-v\,\gamma\,k_{t_m}|t-z/v|} \tag{5.23a}$$

$$\vec{\mathcal{E}}^{(2\mathrm{D})}_{z}(\vec{r}, t) = -u(t-z/v)\frac{Q}{2\,\varepsilon_0} \sum_{m=1}^{\infty} k^2_{t_m}\, \phi^{TM}_m(\vec{r}_\perp)\, I^{TM}_{\perp\perp_m}\; e^{-v\,\gamma\,k_{t_m}|t-z/v|}\,\hat{z} \tag{5.23b}$$

$$\vec{\mathcal{H}}^{(2\mathrm{D})}_{\perp}(\vec{r}, t) = \frac{Q\,v\,\gamma}{2} \sum_{m=1}^{\infty} k_{t_m}\, \vec{h}^{TM}_{\perp_m}(\vec{r}_\perp)\, I^{TM}_{\perp\perp_m}\; e^{-v\,\gamma\,k_{t_m}|t-z/v|} \tag{5.23c}$$

$$\vec{\mathcal{H}}^{(2\mathrm{D})}_{z}(\vec{r}) = 0 \tag{5.23d}$$

The field expressions for a 2-dimensional distribution (5.21) and (5.23) are similar to the punctual charge fields (5.14) and (5.15), respectively. These similarities are more evident if we express such fields as the sum of modal fields quantities [45, 46]:

$$\vec{E}(\vec{r}, \omega) = \sum_{m=1}^{\infty} \vec{E}_m(\vec{r}, \omega) \tag{5.24a}$$

$$\vec{H}(\vec{r}, \omega) = \sum_{m=1}^{\infty} \vec{H}_m(\vec{r}, \omega) \tag{5.24b}$$

$$\vec{\mathcal{E}}(\vec{r}, t) = \sum_{m=1}^{\infty} \vec{\mathcal{E}}_m(\vec{r}, t) \tag{5.24c}$$

$$\vec{\mathcal{H}}(\vec{r}, t) = \sum_{m=1}^{\infty} \vec{\mathcal{H}}_m(\vec{r}, t) \tag{5.24d}$$

Hence we can write:

$$\vec{E}^{(2\mathrm{D})}(\vec{r}, \omega) = \sum_{m=1}^{\infty} \vec{E}^{(\mathrm{point})}_m(\vec{r}, \omega)\, \frac{I^{TM}_{\perp\perp_m}}{\phi^{TM}_m(x_0, y_0)} \tag{5.25a}$$

$$\vec{H}^{(2\mathrm{D})}(\vec{r}, \omega) = \sum_{m=1}^{\infty} \vec{H}^{(\mathrm{point})}_m(\vec{r}, \omega)\, \frac{I^{TM}_{\perp\perp_m}}{\phi^{TM}_m(x_0, y_0)} \tag{5.25b}$$

$$\vec{\mathcal{E}}^{(2\mathrm{D})}(\vec{r}, t) = \sum_{m=1}^{\infty} \vec{\mathcal{E}}^{(\mathrm{point})}_m(\vec{r}, t)\, \frac{I^{TM}_{\perp\perp_m}}{\phi^{TM}_m(x_0, y_0)} \tag{5.25c}$$

$$\vec{\mathcal{H}}^{(2\mathrm{D})}(\vec{r}, t) = \sum_{m=1}^{\infty} \vec{\mathcal{H}}^{(\mathrm{point})}_m(\vec{r}, t)\, \frac{I^{TM}_{\perp\perp_m}}{\phi^{TM}_m(x_0, y_0)} \tag{5.25d}$$

5.5.3 2-dimensional Gaussian distribution

In bunched applications, it is common to focus the particles following a Gaussian distribution within the beampipe. For this reason, such distribution deserves a dedicated analysis. In the present

section, the fields radiated by a 2-dimensional Gaussian distribution are derived. A transverse Gaussian disc of charge centered at $\vec{r}_{\perp_0} = (x_0, y_0)$ and with variances σ_x and σ_y is considered. The disc is flat on z. The probability density function of charge is:

$$f_\rho^{(\text{2D-Gauss})}(\vec{r}\,') \;=\; \frac{1}{2\,\pi\,\sigma_x\,\sigma_y}\;\; e^{-\frac{1}{2}\left(\frac{x'-x_0}{\sigma_x}\right)^2}\;\; e^{-\frac{1}{2}\left(\frac{y'-y_0}{\sigma_y}\right)^2}\;\delta(z'-vt) \tag{5.26}$$

Thus the current density will be:

$$\vec{\mathcal{J}}^{(\text{2D-Gauss})}(\vec{r}\,', t) \;=\; \frac{Q\,v}{2\,\pi\,\sigma_x\,\sigma_y}\;\; e^{-\frac{1}{2}\left(\frac{x'-x_0}{\sigma_x}\right)^2}\;\; e^{-\frac{1}{2}\left(\frac{y'-y_0}{\sigma_y}\right)^2}\;\delta(t-z'v)\,\hat{z} \tag{5.27a}$$

$$\vec{J}^{(\text{2D-Gauss})}(\vec{r}\,', \omega) \;=\; \frac{Q}{2\,\pi\,\sigma_x\,\sigma_y}\;\; e^{-\frac{1}{2}\left(\frac{x'-x_0}{\sigma_x}\right)^2}\;\; e^{-\frac{1}{2}\left(\frac{y'-y_0}{\sigma_y}\right)^2}\;\; e^{-i\,\frac{\omega\,z'}{v}}\;\hat{z} \tag{5.27b}$$

Following a similar derivation as for the previous cases, the next expression for the electromagnetic fields in the frequency-domain is found:

$$\vec{E}_\perp^{(\text{2D-Gauss})}(\vec{r}, \omega) \;= \frac{Q}{v\,\varepsilon_0}\;\; e^{-i\,\frac{\omega\,z}{v}}\;\sum_{m=1}^{\infty}\; k_{t_m}^2\;\vec{e}_m^{TM}(\vec{r}_\perp)\,\frac{1}{\left(\frac{\omega}{v}\right)^2 - k_{z_m}^2}\,I_{\perp\perp_m}^{TM}(x_0, y_0) \tag{5.28a}$$

$$\vec{E}_z^{(\text{2D-Gauss})}(\vec{r}, \omega) \;= \frac{Q}{i\,\varepsilon_0}\;\; e^{-i\,\frac{\omega\,z}{v}}\;\sum_{m=1}^{\infty}\; k_{t_m}^4\;\phi_m^{TM}(\vec{r}_t)\,\frac{1}{\left(\frac{\omega}{v}\right)^2 - k_{z_m}^2}\,I_{\perp\perp_m}^{TM}(x_0, y_0)\,\hat{z} \tag{5.28b}$$

$$\vec{H}_\perp^{(\text{2D-Gauss})}(\vec{r}, \omega) \;= \frac{Q\,\gamma}{\varepsilon_0}\;\; e^{-i\,\frac{\omega\,z}{v}}\;\sum_{m=1}^{\infty}\; k_{t_m}^2\;\vec{h}_m^{TM}(\vec{r}_\perp)\,\frac{1}{\left(\frac{\omega}{v}\right)^2 - k_{z_m}^2}\,I_{\perp\perp_m}^{TM}(x_0, y_0) \tag{5.28c}$$

$$\vec{H}_z^{(\text{2D-Gauss})}(\vec{r}, \omega) \;= 0 \tag{5.28d}$$

here $I_{\perp\perp}^{TM}$ represents the integral:

$$I_{\perp\perp}^{TM}(x_0, y_0) \;=\; \frac{1}{2\,\pi\,\sigma_x\,\sigma_y}\iint_{CS'}\phi_m^{TM}(\vec{r}_\perp{}')\;\; e^{-\frac{1}{2}\left(\frac{x'-x_0}{\sigma_x}\right)^2}\;\; e^{-\frac{1}{2}\left(\frac{y'-y_0}{\sigma_y}\right)^2}\;dCS' \tag{5.29}$$

(5.28) gives the exact fields radiated by a 2-dimensional Gaussian bunch, in contrast to the classical Bassetti-Erskine formula [78], which has been widely used to approach this problem. Finally, the time-domain fields are:

$$\vec{\mathcal{E}}_\perp^{(\text{2D-Gauss})}(\vec{r}, t) \;=\; \frac{Q\,\gamma}{2\,\varepsilon_0}\sum_{m=1}^{\infty}\; k_{t_m}\,\vec{e}_m^{TM}(\vec{r}_\perp)\,I_{\perp\perp_m}^{TM}(x_0, y_0)\;\; e^{-k_{t_m}\,\gamma\,|z-vt|} \tag{5.30a}$$

$$\vec{\mathcal{E}}_z^{(\text{2D-Gauss})}(\vec{r}, t) \;=\; \frac{Q}{2\,\varepsilon_0}\,u(z-vt)\sum_{m=1}^{\infty}\; k_{t_m}^2\;\phi_m^{TM}(\vec{r}_\perp)\,I_{\perp\perp_m}^{TM}(x_0, y_0)\;\; e^{-k_{t_m}\,\gamma\,|z-vt|}\,\hat{z} \tag{5.30b}$$

$$\vec{\mathcal{H}}_\perp^{(\text{2D-Gauss})}(\vec{r}, t) \;=\; \frac{Q\,v\,\gamma}{2}\sum_{m=1}^{\infty}\; k_{t_m}\,\vec{h}_m^{TM}(\vec{r}_\perp)\,I_{\perp\perp_m}^{TM}(x_0, y_0)\;\; e^{-k_{t_m}\,\gamma\,|z-vt|} \tag{5.30c}$$

$$\vec{\mathcal{H}}_z^{(\text{2D-Gauss})}(\vec{r}, t) \;=\; 0 \tag{5.30d}$$

5.5.4 3-dimensional Gaussian distribution

The electromagnetic fields radiated by a 3-dimensional Gaussian distribution of charge travelling at constant velocity throughout an homogenenous waveguide are presented in this section. A detailed description of the calculation procedure followed is given in Appendix C.2. The probability density function considered in this case follows a 3-dimensional Gaussian distribution, centered at $\vec{r}_0 = (x_0, y_0, vt)$:

$$f_\rho^{(\text{3D-Gauss})}(\vec{r}\,') \;=\; \frac{1}{(2\,\pi)^{3/2}\,\sigma_x\,\sigma_y\,\sigma_z}\; e^{-\frac{1}{2}\left(\frac{x'-x_0}{\sigma_x}\right)^2}\; e^{-\frac{1}{2}\left(\frac{y'-y_0}{\sigma_y}\right)^2}\; e^{-\frac{1}{2}\left(\frac{z'-vt}{\sigma_z}\right)^2} \tag{5.31}$$

where the last exponent represents the bunch distribution in the longitudinal direction. This term modifies the fields derivation from the 2-dimensional distributions previously studied. The current density will be:

$$\vec{\mathcal{J}}^{(\text{3D-Gauss})}(\vec{r}\,', t) \;=\; \frac{Q\,v}{(2\,\pi)^{3/2}\,\sigma_x\,\sigma_y\,\sigma_z}\; e^{-\frac{1}{2}\left(\frac{x'-x_0}{\sigma_x}\right)^2}\; e^{-\frac{1}{2}\left(\frac{y'-y_0}{\sigma_y}\right)^2}\; e^{-\frac{1}{2}\left(\frac{z'-vt}{\sigma_z}\right)^2}\;\hat{z} \tag{5.32a}$$

$$\vec{J}^{(\text{3D-Gauss})}(\vec{r}\,', \omega) \;=\; \frac{Q}{2\,\pi\,\sigma_x\,\sigma_y}\; e^{-\frac{1}{2}\left(\frac{x'-x_0}{\sigma_x}\right)^2}\; e^{-\frac{1}{2}\left(\frac{y'-y_0}{\sigma_y}\right)^2}\; e^{-\frac{1}{2}\left(\frac{\sigma_z\,\omega}{v}\right)^2}\; e^{-i\,\frac{\omega\,z'}{v}}\;\hat{z} \tag{5.32b}$$

where the Fourier pair (B.3d) has been used to obtain the frequency-domain current density. This current density is similar to the result obtained for the case of a 2-dimensional Gaussian disc of charge (5.27b):

$$\vec{J}^{(\text{3D-Gauss})}(\vec{r}\,', \omega) \;=\; \vec{J}^{(\text{2D-Gauss})}(\vec{r}\,', \omega)\; e^{-\frac{1}{2}\left(\frac{\sigma_z\,\omega}{v}\right)^2} \tag{5.33}$$

Consequently, the frequency-domain electromagnetic fields radiated by a 3-dimensional Gaussian charge distribution are:

$$\vec{E}_\perp^{(\text{3D-Gauss})}(\vec{r}, \omega) \;= \frac{Q}{2\,\pi\,v\,\varepsilon_0\,\sigma_x\,\sigma_y}\; e^{-\frac{1}{2}\left(\frac{\sigma_z\,\omega}{v}\right)^2}\; e^{-i\,\frac{\omega\,z}{v}}\; \sum_{m=1}^{\infty} k_{t_m}^2\; \vec{e}_m^{\,TM}(\vec{r}_\perp)\; \frac{1}{\left(\frac{\omega}{v}\right)^2 - k_{z_m}^2}\; I_{\perp\perp_m}^{TM}(x_0, y_0) \tag{5.34a}$$

$$\vec{E}_z^{(\text{3D-Gauss})}(\vec{r}, \omega) \;= \frac{Q}{i\,2\,\pi\,\varepsilon_0\,\sigma_x\,\sigma_y}\; e^{-\frac{1}{2}\left(\frac{\sigma_z\,\omega}{v}\right)^2}\; e^{-i\,\frac{\omega\,z}{v}}\; \sum_{m=1}^{\infty} k_{t_m}^4\; \phi_m^{TM}(\vec{r}_t)\; \frac{1}{\left(\frac{\omega}{v}\right)^2 - k_{z_m}^2}\; I_{\perp\perp_m}^{TM}(x_0, y_0)\,\hat{z} \tag{5.34b}$$

$$\vec{H}_\perp^{(\text{3D-Gauss})}(\vec{r}, \omega) \;= \frac{Q\,\gamma}{2\,\pi\,\varepsilon_0\,\sigma_x\,\sigma_y}\; e^{-\frac{1}{2}\left(\frac{\sigma_z\,\omega}{v}\right)^2}\; e^{-i\,\frac{\omega\,z}{v}}\; \sum_{m=1}^{\infty} k_{t_m}^2\; \vec{h}_m^{\,TM}(\vec{r}_\perp)\; \frac{1}{\left(\frac{\omega}{v}\right)^2 - k_{z_m}^2}\; I_{\perp\perp_m}^{TM}(x_0, y_0) \tag{5.34c}$$

$$\vec{H}_z^{(\text{3D-Gauss})}(\vec{r}, \omega) \;= 0 \tag{5.34d}$$

The fields in the time-domain are (see Appendix C.2):

$$\vec{\mathcal{E}}_{\perp}^{(\text{3D-Gauss})}(\vec{r},t) = \frac{Q\,\gamma}{8\,\pi\,\sigma_x\,\sigma_y\,\varepsilon_0}\sum_{m=1}^{\infty} k_{t_m}\,\vec{e}_m^{TM}(\vec{r}_\perp)\;e^{\frac{1}{2}(k_{t_m}\,\gamma\,\sigma_z)^2}\,I_m^{TM}(x_0,y_0)$$
$$\left[\;e^{-k_{t_m}\,\gamma(z-vt)}\,erfc\left(\frac{k_{t_m}\,\gamma\,\sigma_z}{\sqrt{2}}-\frac{(z-vt)}{\sqrt{2}\,\sigma_z}\right)+\;e^{k_{t_m}\,\gamma(z-vt)}\,erfc\left(\frac{k_{t_m}\,\gamma\,\sigma_z}{\sqrt{2}}+\frac{(z-vt)}{\sqrt{2}\,\sigma_z}\right)\right] \tag{5.35a}$$

$$\vec{\mathcal{E}}_{z}^{(\text{3D-Gauss})}(\vec{r},t) = \frac{Q}{8\,\pi\,\sigma_x\,\sigma_y\,\varepsilon_0}\sum_{m=1}^{\infty} k_{t_m}^2\,\phi_m^{TM}(\vec{r}_\perp)\;e^{\frac{1}{2}(k_{t_m}\,\gamma\,\sigma_z)^2}\,I_m^{TM}(x_0,y_0)$$
$$\left[\;e^{-k_{t_m}\,\gamma(z-vt)}\,erfc\left(\frac{k_{t_m}\,\gamma\,\sigma_z}{\sqrt{2}}-\frac{(z-vt)}{\sqrt{2}\,\sigma_z}\right)-\;e^{k_{t_m}\,\gamma(z-vt)}\,erfc\left(\frac{k_{t_m}\,\gamma\,\sigma_z}{\sqrt{2}}+\frac{(z-vt)}{\sqrt{2}\,\sigma_z}\right)\right]\hat{z} \tag{5.35b}$$

where the complementary error function $erfc(x)$ has been used [79]:

$$erfc(x) \;=\; \frac{2}{\sqrt{\pi}}\int_{x}^{+\infty} e^{\tau^2}\,d\tau \;=\; 1\;-\;erf(x) \tag{5.36}$$

It is interesting to note that the field expressions for the 3-dimensional Gaussian distribution of charge tend to the 2-dimensional case when the variance in z-direction approaches to zero:

$$\lim_{\sigma_z\to 0^+}\vec{\mathcal{E}}^{(\text{3D-Gauss})} \;=\; \vec{\mathcal{E}}^{(\text{2D-Gauss})} \tag{5.37}$$

The convergence of the series in the field expressions presented for 2D and 3D charge distributions has been satisfactorily demonstrated in both the time and frequency domains. On one hand, it can be demonstrated that the field intensity vanishes for long distances to the source charge ($\lim_{z\to\pm\infty}\vec{\mathcal{E}}=0$); on the other hand, the amplitude of the terms in the modal series of the field expressions decrease with the order of the mode m, as previously shown in Sec. 5.4.1 for the punctual charge case.

5.5.5 Train of bunches

The single bunch analysis of the previous sections is now extended to study a train of bunches. The train is formed by a series of N particle bunches separated in the axial direction by a distance Δ_b, as depicted in Fig. 5.9. The electromagnetic fields are derived from the single-bunch field expressions applying the superposition property of Electromagnetism. The charge probability density function of the train of bunches can be expressed like the superposition of single-bunch functions:

$$f_\rho^{(\text{train})}(\vec{r}) \;=\; \sum_{n=0}^{N-1} f_\rho^{(\text{bunch})}(\vec{r})\,\delta(z-\Delta_b\,n) \tag{5.38}$$

Consequently, the electric field is simply:

$$\vec{\mathcal{E}}^{(\text{train})}(\vec{r}) \;=\; \sum_{n=0}^{N-1} \vec{\mathcal{E}}^{(\text{bunch})}(\vec{r})\,\delta(z-\Delta_b\,n) \tag{5.39}$$

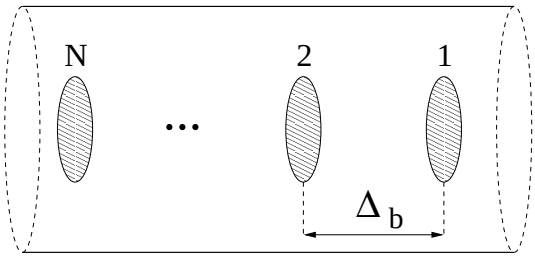

Figure 5.9: Train of N bunches travelling throughout a hollow waveguide. The inter-bunch distance is Δ_b.

, which is the superposition of single-bunch fields shifted in time by Δ_b/v. As an example, the electric field created by a train of 2D-Gaussian bunches is shown next:

$$\vec{\mathcal{E}}_t^{\begin{pmatrix}\text{train}\\ \text{2DGauss}\end{pmatrix}}(\vec{r},t) = \frac{Q\,\gamma}{4\,\pi\,\sigma_x\,\sigma_y\,\varepsilon_0}\sum_{n=0}^{N-1}\sum_{m=1}^{\infty} k_{t_m}\,\vec{e}_m^{TM}(\vec{r}_t)\,I_m^{TM}(\vec{r}_{t0})\;\; e^{-k_{t_m}\gamma\,|z-vt-\Delta_b n|} \tag{5.40a}$$

$$\vec{\mathcal{E}}_z^{\begin{pmatrix}\text{train}\\ \text{2DGauss}\end{pmatrix}}(\vec{r},t) = -\frac{Q}{4\,\pi\,\sigma_x\,\sigma_y\,\varepsilon_0}\sum_{n=0}^{N-1} \left[u\left(t-\frac{z-\Delta_b n}{v}\right)\sum_{m=1}^{\infty} k_{t_m}^2\,\phi_m^{TM}(\vec{r}_t)\,I_m^{TM}(\vec{r}_{t0})\;\; e^{-k_{t_m}\gamma\,|z-vt-\Delta_b n|}\right]\vec{z} \tag{5.40b}$$

5.6 Numerical results

The formulation given in Sec. 5.4.1 for punctual charges will be applied now to the analysis of wakefields within structures of arbitrary geometry, thus proving the capabilities of this method. In a first example, a cross-shaped waveguide has been chosen for discussing the effect of rounding the corners of the inner waveguide walls. In the second example, several geometries are compared to a waveguide similar to the CERN Large Hadron Collider (LHC) beampipe.

5.6.1 Rounded-corner cross-shaped waveguides

It is well known that the electromagnetic fields within a waveguide are particularly strong near convex wedges. The power focusing in these areas gives rise to undesirable consequences, like the heating of walls and the attraction of free particles. The accumulation of charged particles in a small region of the beampipe will produce changes in the resistivity of the component and multipactoring effects, both causing losses and defocusing in the beam. For this reason, sharp wedges are avoided in the design of accelerating structures as far as possible.

With the aim of studying the influence of corners in the geometry of a beampipe, an homogeneous cross-shaped waveguide with rounded corners (see Fig. 5.10) has been analysed. Three different radii

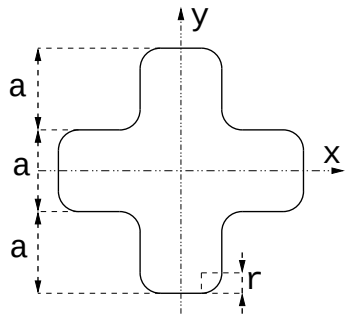

Figure 5.10: Cross-section of a rounded-corner cross-shaped waveguide.

of curvature r for the corners of the waveguide are considered for comparison. The size of the arms of the cross has been selected to $a = 3$ mm. The wakefields for two different trajectories of a source particle are compared.

For the calculation of the modal expansion of the waveguide, the two-dimensional BI-RME method seen in Sec. 5.3 was used. The BI-RME method [45, 75] has been revealed as a robust and high computational efficient modal technique for the characterization of arbitrary waveguides, whose accuracy is discussed in[74, 75]. A total of 450 electric TM-modal vectors were generated by a BI-RME based tool [74] and used to evaluate the δ-function wake potential at any point.

Fig. 5.11-5.12 show the wake-potential distribution in the XY-plane at $s = 5$ μm behind the source. In Fig. 5.11 the source particle is on the center of the waveguide and the normalized velocity is $\beta = 1 - 10^{-7}$; on the other hand, in Fig. 5.12 the source is within one of the arms of the waveguide, and the normalized velocity is $\beta = 1 - 10^{-6}$. The CPU time used for the computation of a unique point is 42 seconds in a standard PC at 3.2 GHz.

Cuts along the y-axis of preceding pictures are found in Fig. 5.13 and 5.14, where w_x has been omitted (this component is null on the y-axis because of the symmetry of the problem). The maximum value for w_z varies with the radius of curvature, but obviously coincides with the source location, as can be seen in 5.13(b) and 5.14(b). The behavior of the transverse wake potential is different. From Fig. 5.13(a) it is observed that, when the source is at the center, the maximum magnitude for w_y lays at a point within the interval $\pm\,(a/2, a/2 + r)$; this interval coincides with the narrowing of the waveguide at the beginning of one arm of the cross. On the other hand, when the source is shifted from the center (Fig. 5.14(a)), the transverse wake potential has an offset related to the deviation of the leading charge.

The different scales for the wake potential intensity shown in both trajectories can be explained by the difference in velocity. Note that the electric field distribution is contracted into a disk perpendicular to the direction of motion with a narrow angular spread of the order of $1/\gamma$, as reported in [68]. In Fig. 5.15, the wake potential is plotted for a testing and a trial charge depending on the velocity. It is shown that the intensity of the longitudinal wake potential decreases with the velocity as a consequence of the electric field contraction.

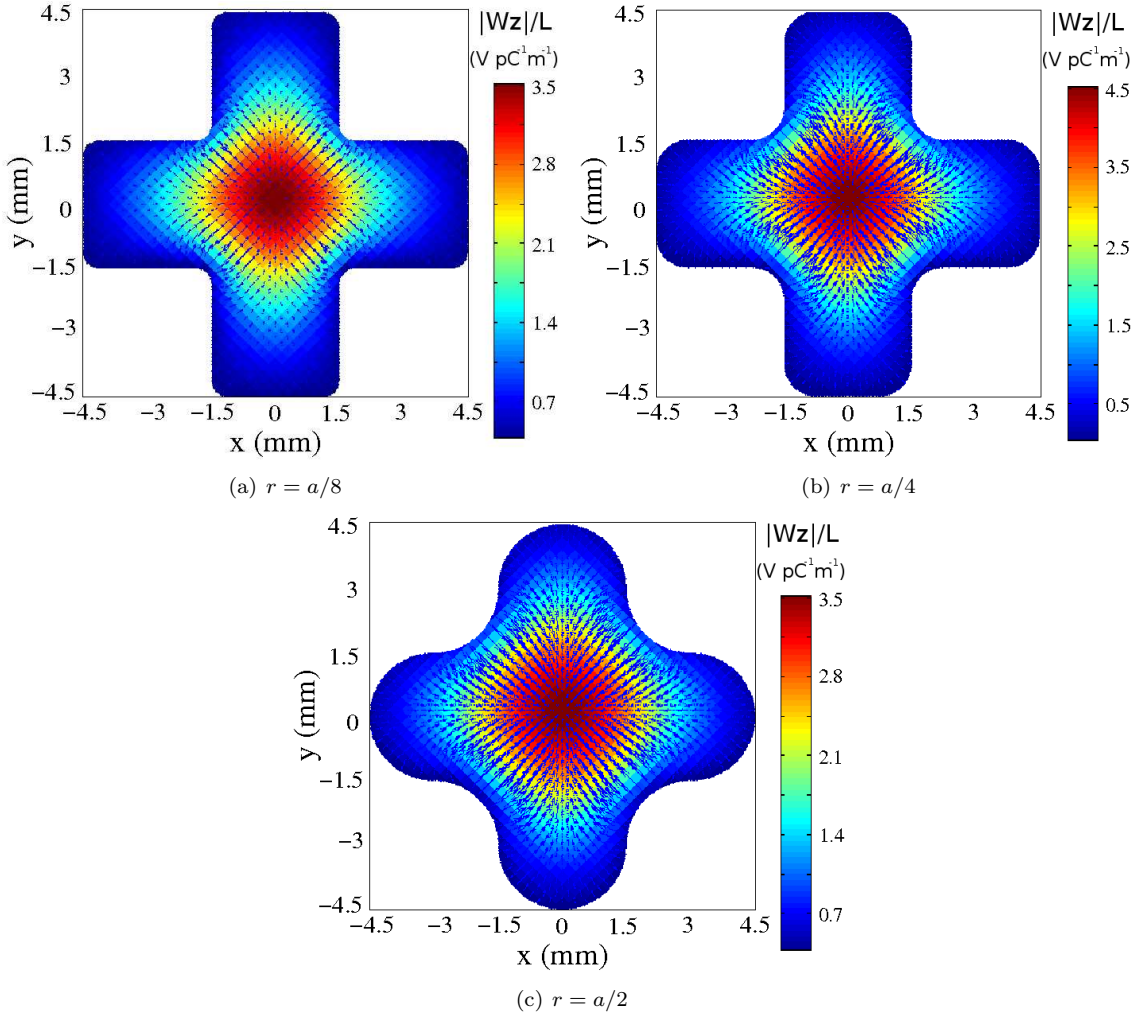

(a) $r = a/8$

(b) $r = a/4$

(c) $r = a/2$

Figure 5.11: δ-function wake potential for cross-shaped waveguides with different radius of curvature. Picture of the transverse plane at a distance $s = 5$ μm behind the source charge. $\vec{r}_\perp{}' = (0, 0)$, $\beta = 1 - 10^{-7}$. The colorbar stands for $|w_z|/L$ $(V\,pC^{-1}\,m^{-1})$ and the arrows point to the direction of $\vec{w}_\perp$.

5.6.2 A comparative study of the wake potentials for different waveguide geometries

An homogeneous waveguide with a cross-section similar to the beampipe used in the CERN LHC Laboratory [80, 81] has been modelled by means of a BI-RME based tool. The wake potential in this structure is compared for several waveguides, which have different cross-sections. A total of four waveguide geometries are considered. In order to obtain comparable structures, the dimensions of

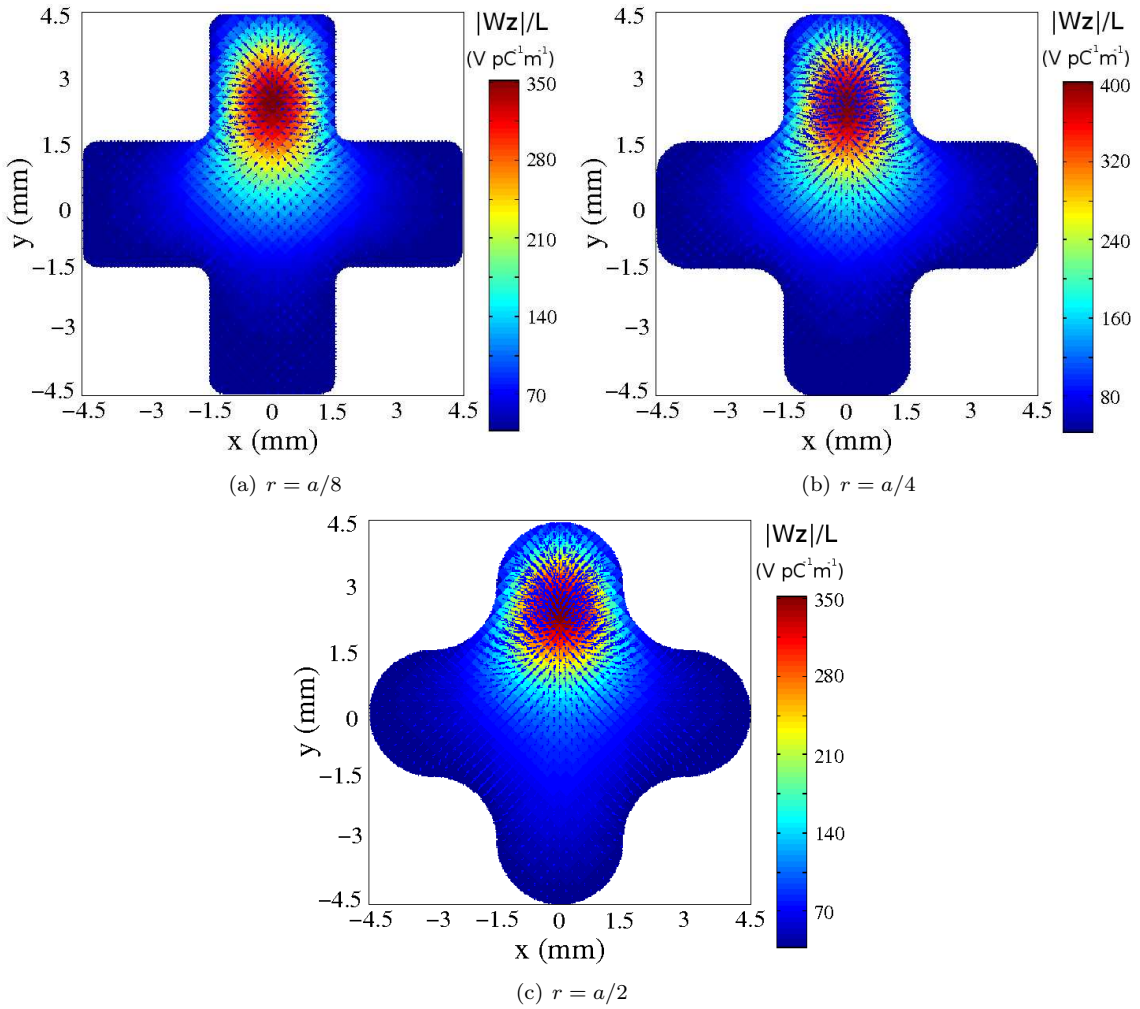

(a) $r = a/8$

(b) $r = a/4$

(c) $r = a/2$

Figure 5.12: δ-function wake potential for cross-shaped waveguides with different radius of curvature. Picture of the transverse plane at a distance $s = 5$ μm behind the source charge. $\vec{r}_\perp{}' = (0, 2.3)\, mm$, $\beta = 1 - 10^{-6}$. The colorbar stands for $|w_z|/L$ $(V\, pC^{-1}\, m^{-1})$ and the arrows point to the direction of $\vec{w}_\perp$.

the guides are such that the cut-off frequencies of the two first propagative modes are close enough to that of the original beampipe. In Fig. 5.16 there is a picture of the different geometries analysed, whose dimensions and cut-off frequencies are related in Table 5.1. Hence, the original LHC beampipe is shown in Fig. 5.16(a), and is denoted as waveguide A in the aforementioned table. Note that in most of the geometries cut-off frequencies cannot be tuned independently, so the achieved results are not so close for the second mode.

Next, the wakefield of a point charge is analysed for the proposed waveguides. The potentials have

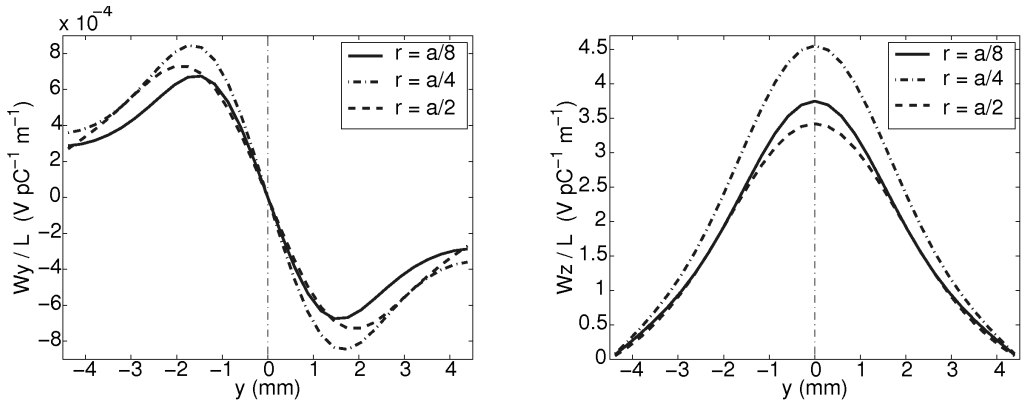

(a) w_y (b) w_z

Figure 5.13: Dependence of the δ-function wake potential on the transverse position of a trailing charge along the y-axis for cross-shaped waveguides. The leading charge is located at the center of the waveguide (vertical dashed line), $s = 5$ μm and $\beta = 1 - 10^{-7}$.

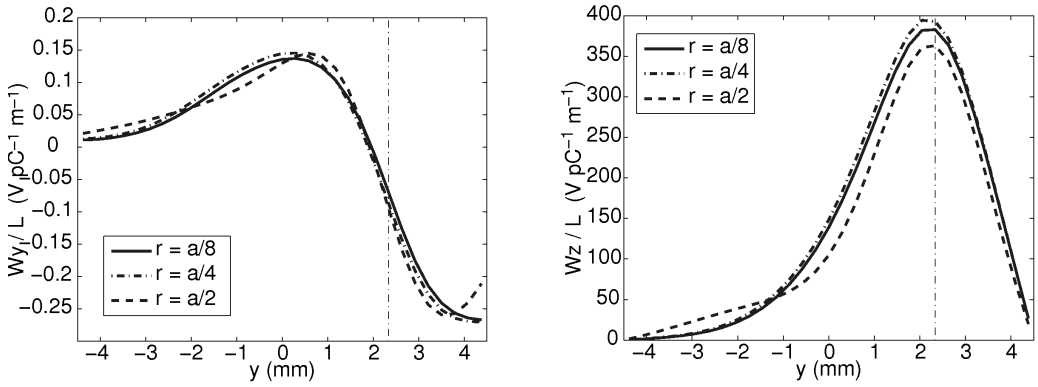

(a) w_y (b) w_z

Figure 5.14: Dependence of the δ-function wake potential on the transverse position of a trailing charge along the y-axis for cross-shaped waveguides. The leading charge is located at the point $(x, y) = (0, 2.3)$ mm (vertical dashed line), $s = 5$ μm and $\beta = 1 - 10^{-6}$.

been computed using 1800 TM-modal vectors, previously obtained by a BI-RME simulation tool. The source charge moves along the z-direction at the center of the waveguides. In Fig. 5.17-5.19, the wake potential is evaluated on the cross axes for several velocities. Only the positive semi-axes are considered because of symmetry. Despite results are similar for all the geometries, some conclusions can be extracted from these plots. The lengthwise force w_z induced on a trailing charge is smaller in rounded-corner rectangular waveguides, whereas the response is worse in a circular waveguide; the same happens for w_x, but it is not the case for w_y. It is also worthwhile to mention that the wakefields

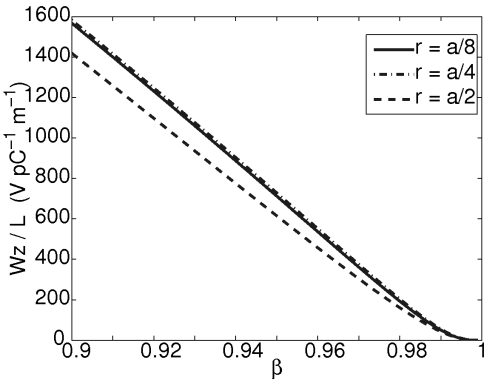

Figure 5.15: Dependence of w_z on the velocity of the charges. Both charges travel on the center of the waveguide and $s = 1$ mm.

WG	Figure	Dimensions (mm)	f_{c_1} (GHz)	f_{c_2} (GHz)
A	5.16(a)	$a_1 = 44$, $b_1 = 36$, $r_1 = 22$	3.84	4.49
B	5.16(b)	$a_2 = 39$, $b_2 = 34$, $r_2 = 3$	3.86	4.43
C	5.16(b)	$a_2 = 44$, $b_2 = 36$, $r_2 = 15.3$	3.80	4.56
D	5.16(c)	$a_3 = 46$, $b_3 = 32$, $h = 34$	3.82	5.22
E	5.16(d)	$r_4 = 22$	3.99	5.21

Table 5.1: Waveguides used in section 5.6.2 and cut-off frequencies for the first two modes.

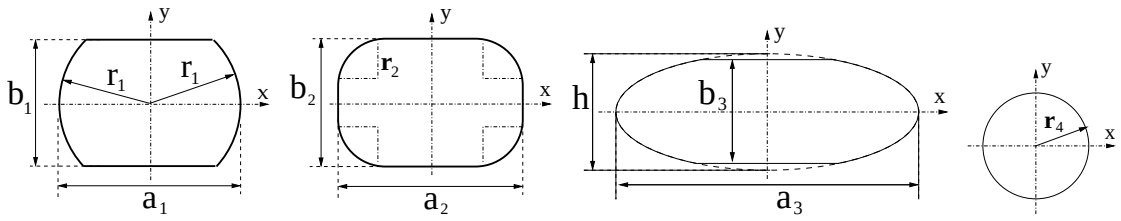

(a) LHC beampipe (b) Rounded-corner rectangular waveguide (c) LHC beampipe modified with elliptical side walls (d) Circular waveguide

Figure 5.16: Cross-section of the waveguides studied in section 5.6.2.

produced in the waveguides A and D are very close.

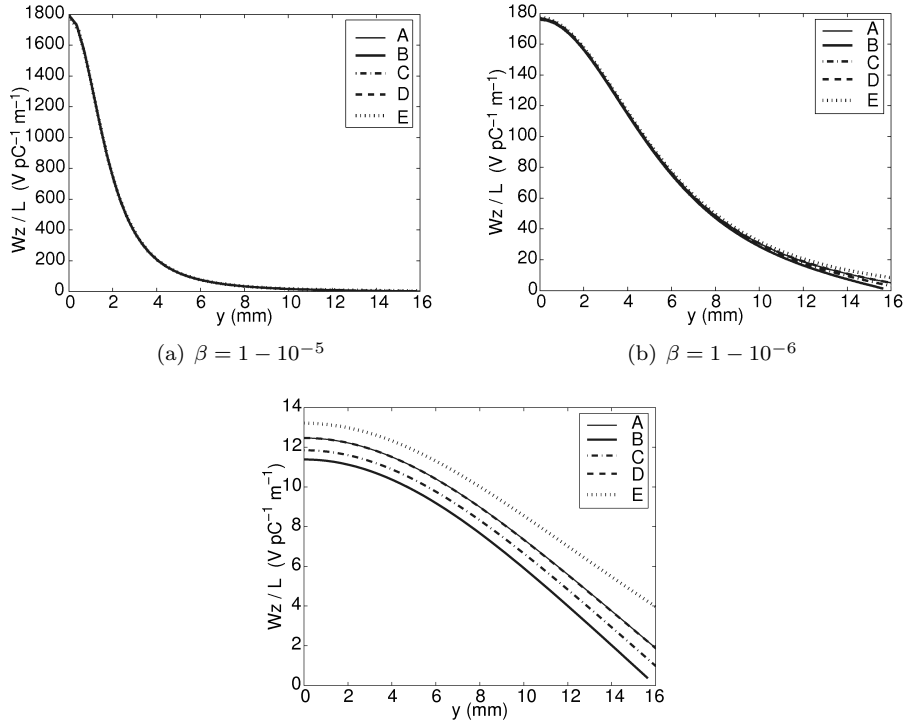

(a) $\beta = 1 - 10^{-5}$ (b) $\beta = 1 - 10^{-6}$

(c) $\beta = 1 - 10^{-7}$

Figure 5.17: w_z/L on the positive y-semiaxis for different particle velocities. The source charge is located at the center of the waveguide; $s = 10$ μm.

Finally, the dependence of the wake potential on the velocity of the particles is shown in Fig. 5.20.

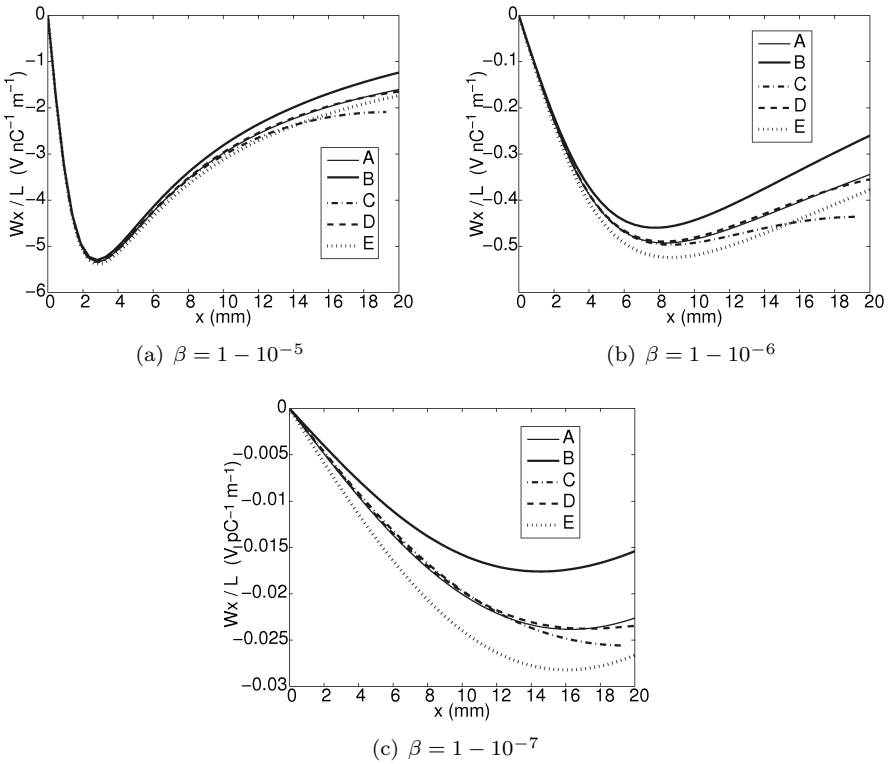

(a) $\beta = 1 - 10^{-5}$

(b) $\beta = 1 - 10^{-6}$

(c) $\beta = 1 - 10^{-7}$

Figure 5.18: w_x/L on the positive x-semiaxis for different particle velocities. The source charge is located at the center of the waveguide; $s = 10$ μm.

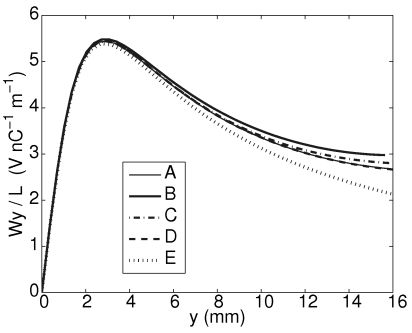

(a) $\beta = 1 - 10^{-5}$

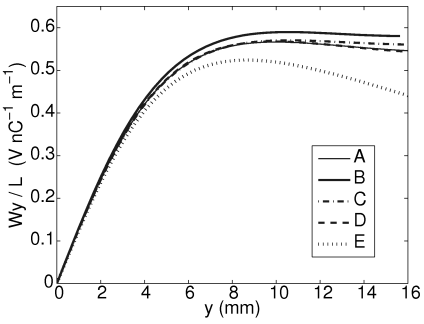

(b) $\beta = 1 - 10^{-6}$

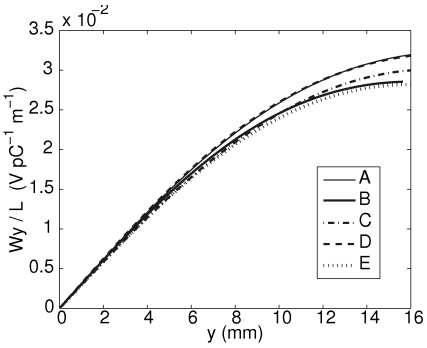

(c) $\beta = 1 - 10^{-7}$

Figure 5.19: w_y/L on the positive y-semiaxis for different particle velocities. The source charge is located at the center of the waveguide; $s = 10$ μm.

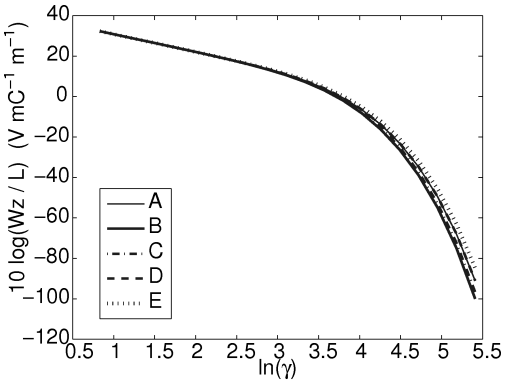

Figure 5.20: Dependence of w_z on the velocity. The leading charge travels along the center of the waveguide; $s = 1$ mm. A logarithmic scale has been chosen to emphasize differences at high velocities.

Chapter 6

Conclusions and Future Lines

The 3-dimensional Dyadic Green's function as formulated in Chapter 2 has demonstrated to be a powerful mathematical tool which can be applied to different problems of electromagnetic radiation, such as the simulation of the power spectrum of a multipactor discharge in an RF component and the study of the wakefields generated by a charge distribution within a particle accelerator.

A multimode network for multipactor discharges in waveguides has been proposed and used to compute the electromagnetic radiation of a multipactor event occurring within a realistic component. Moreover, the power spectrum of a multipactor discharge induced within a WR-75 transformer has been experimentally measured and compared to the results provided by the present model, obtaining good agreement. The experiments also suggest that multipactor detection by means of the intermediate harmonics proposed here is a valid technique which should not be ignored in those cases where classical techniques like the third harmonic detection system cannot be implemented. In this sense, it would be interesting to improve this technique by introducing in the test-bed an RF carrier at the harmonic frequency with a suitable power level to be read by SAs.

The calculation of the wakefields is a primary task in the evaluation of the suitability of a beampipe. In this sense, the use of δ-function wake potentials is a good strategy for predicting the response of a waveguide to real bunches of particles. In this Thesis, a method for the calculation of the wake potential for point charges in uniform waveguides with arbitrarily shaped cross-section has been presented. An expression for the wake potentials as a function of the vector modal functions of the waveguide has been proposed. The method consists of deriving the electromagnetic fields radiated by a point charge through the three-dimensional dyadic Green's functions of the waveguide; the wake potential is further extracted from the time-domain expression of the fields. A few examples have been included to show the capabilities of the presented method. The modal analysis of the geometries in the examples has been accomplished by a BI-RME based tool. The flexibility and efficiency of the BI-RME method makes possible an accurate computation of the modes of arbitrary waveguides. Like every numerical methods, the BI-RME technique presents the computation time drawback. The computation time increases in quadratic fashion with the number of segments required for meshing the structure. In this sense, the use of adaptive meshing and numerical integration techniques for the calculation of the modal vectors of a waveguide would allow to accomplish more accurate analysis of non-canonical structures and different charge distributions. In this Thesis only the constant velocity case is presented. Several different cases have been also analyzed, like the uniform acceleration motion. The formulation derived in such cases is mainly numerical and requires fine meshing in order to obtain

accurate results.

Appendix A

Modal characterization of networks

Some parameters of the classical theory of microwave networks are reviewed in this appendix. Single-mode networks are analysed first; after that, some significant parameters of multimode networks are presented.

A.1 Single-mode networks

In the frame of the transmission lines formalism, the transmission of an RF signal on a waveguide component can be described by electric circuits [45, 46, 47, 48]. The electric voltage and current in the circuit are directly related with the electric and magnetic fields in the microwave component. In this section, we revise basic concepts of the single-mode analysis of such networks. Fig. A.1 shows a simple circuit, where a single-mode, passive, lossless quadrupole is excited by a time-harmonic voltage source of amplitude V_g. The ports of the quadrupole are loaded with the characteristic impedance of the line Z_0. The equivalent voltage and current at the input-port of the quadrupole are named V_1 and I_1, respectively; V_2 and I_2 for the output-port. The power in the circuit is supplied by a voltage source, whose amplitude V_g can be expressed as

$$V_g \;=\; I_1 Z_0 + V_1 \tag{A.1}$$

The law of conservation of energy states that the power supplied by the source (P_g) must equal the sum of the power reflected from the passive, lossless quadrupole (P_r) and the power transmitted through and dissipated at the load (P_t). Hence,

$$P_g \;=\; P_r + P_t \tag{A.2}$$

These powers are defined as

$$P_g \;=\; \frac{1}{2}\; Re\left\{V_g I_1^*\right\} \tag{A.3a}$$

$$P_r \;=\; \frac{1}{2} Z_0 \left|-I_1\right|^2 \tag{A.3b}$$

$$P_t \;=\; \frac{1}{2} Z_0 \left|-I_2\right|^2 \tag{A.3c}$$

$$\tag{A.3d}$$

On the other hand, it is well known that equivalent voltages and currents can be expressed as the sum of an incident and a reflected waves:

$$V = V^+ + V^- \tag{A.4a}$$
$$I = I^+ - I^- \tag{A.4b}$$

The characteristic impedance being

$$Z_0 = \frac{V^+}{I^+} = \frac{V^-}{I^-} \tag{A.5}$$

It allows to rewrite the powers of the circuit as a function of incident and reflected waves:

$$P_g = \frac{1}{2} V_g \; Re\left\{ I_1^{+*} - I_1^{-*} \right\} \tag{A.6a}$$
$$P_r = \frac{1}{2} Y_0 \left| V_1^+ - V_1^- \right|^2 \tag{A.6b}$$
$$P_t = \frac{1}{2} Y_0 \left| V_2^+ - V_2^- \right|^2 \tag{A.6c}$$

In the circuit shown in Fig. A.1, the load at the output-port prevents power reflections. Therefore, in this case we can write:

$$V_2^- = I_2^- = 0 \tag{A.7}$$

At this point, we introduce the scattering parameters S, which measure the ratio of power reflected at the different ports of a network [46, 47]. The S-parameters describe the response of a network to voltage signals at each port. A possible definition for a quadrupole would be:

$$|S_{11}|^2 = \left| \frac{V_1^-}{V_1^+} \right|^2 \tag{A.8a}$$
$$|S_{21}|^2 = \left| \frac{V_2^-}{V_1^+} \right|^2 \tag{A.8b}$$
$$|S_{12}|^2 = \left| \frac{V_1^-}{V_2^+} \right|^2 \tag{A.8c}$$
$$|S_{22}|^2 = \left| \frac{V_2^-}{V_2^+} \right|^2 \tag{A.8d}$$

A common technique for obtaining the scattering parameters of a network consists in the successive excitation of each port, keeping all the other ports matched. In this sense, the circuit configuration shown in Fig. A.1 is used to calculate S_{11} and S_{21}, because the load Z_0 at the output-port prevents from the incidence of power at such port. On the other hand, in order to obtain S_{12} and S_{22} is necessary to change the position of the voltage source to the output-port. Using (A.6) and (A.8), we can deduce some interesting expressions. Firstly, the power at the ports of the quadrupole can now be expressed as:

$$P_r = \frac{1}{2} Y_0 \left| V_1^+ \right|^2 \left| 1 - S_{11} \right|^2 \tag{A.9a}$$
$$P_t = \frac{1}{2} Y_0 \left| V_2^+ \right|^2 \left| S_{21} \right|^2 \tag{A.9b}$$

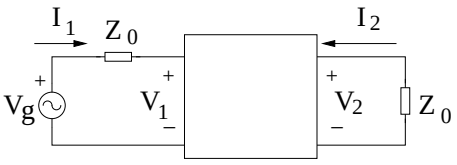

Figure A.1: Single-mode network with a passive, lossless quadrupole.

and the amplitude of the voltage source can be simplified to

$$V_g \;=\; 2V_1^+ \tag{A.10}$$

meanwhile the following expression is deduced for the power supplied by the generator:

$$P_g \;=\; Re\left\{Y_0\left(|V_1^+|^2 - V_1^{+*}V_1^-\right)\right\} \tag{A.11}$$

Finally, it is worth to mention that the application of (A.9) and (A.11) to (A.2) leads to the well-known formula for passive, lossless quadrupoles:

$$|S_{11}|^2 + |S_{21}|^2 \;=\; 1 \tag{A.12}$$

A.2 Multimode networks

The transmission of electromagnetic fields in bounded regions is better analysed under the modal approach [45, 46, 47, 48]. Modal analysis assumes that, in a bounded region, the field intensity transverse to the direction of propagation can be divided into an infinite number of modes, the transmission pattern of each one being determined by the geometry of the region. Thus, the transverse electric $\vec{E}_\perp$ and magnetic $\vec{H}_\perp$ fields can be expressed as:

$$\vec{E}_\perp \;=\; \sum_{k=1}^{\infty} V_k\,\vec{e}_k \tag{A.13a}$$

$$\vec{H}_\perp \;=\; \sum_{k=1}^{\infty} I_k\,\vec{h}_k \tag{A.13b}$$

where $\vec{e}$ and $\vec{h}$ are the electric and magnetic transverse modal vectors, respectively, which are dependent of the bounding geometry. On the other hand, V and I stand for the modal amplitudes, which quantify the portion of the electromagnetic field carried on each mode. In the transmission lines analogy, these modal amplitudes are the equivalent voltage V and current I of the circuit that represents the microwave system. The single-mode analysis of such systems, as seen in the preceeding section, is only valid for those cases where all (or the most part of) the energy is transmitted on one mode. This fact depends on the geometry as well as the relative size of bounds and signal wavelength. In most cases, the modes can be sorted as a function of the carried power. It allows to truncate

the expansion (A.13) to a reasonable number of modes N, according to computation restrictions and accuracy required:

$$\vec{E}_\perp \approx \sum_{k=1}^{N} V_k \, \vec{e}_k \tag{A.14a}$$

$$\vec{H}_\perp \approx \sum_{k=1}^{N} I_k \, \vec{h}_k \tag{A.14b}$$

The multimode analysis of RF systems can be a complicated task because of the large number of variables. In this sense, the separate characterization of subsystems or components as multimodal matrices simplifies the problem. A multimodal matrix of an RF subsystem is a matricial representation of the structure which gives the outputs of the system at certain electric stimuli. In this way the component can be treated as a black-box with a set of modal ports, being only necessary to know the behavior of the box at the ports. There are several types of matrices, which can be chosen for each case depending on the parameter they represent. Examples of these matrices are the scattering matrix $[S]$, the impedance matrix $[Z]$ and the transmission matrix $[T]$; the algebraical operations that allows to change from one to another matrix representation have been well established [48]. Linking matrices of successive RF subsystem makes easy to analyze a complete system and to focus on the points of interest [45], as shown in Sec. 4.5 for the characterization of multipactor discharges within passive components.

An example of a multimode network is shown in Fig. A.2(a). It is a two-ports, N-modes network. The pair $(V_1^{(k)}, I_1^{(k)})$ represents the voltage and current of the kth-mode at the input-port; the pair $(V_2^{(k)}, I_2^{(k)})$ stands for the output-port. A possible writting for the scattering matrix of this network would be:

$$[S] = \begin{pmatrix} S_{\substack{11\\11}} & S_{\substack{12\\11}} & \cdots & S_{\substack{1N\\11}} & S_{\substack{11\\12}} & S_{\substack{12\\12}} & \cdots & S_{\substack{1N\\12}} \\ S_{\substack{21\\11}} & S_{\substack{22\\11}} & \cdots & S_{\substack{2N\\11}} & S_{\substack{21\\12}} & S_{\substack{22\\12}} & \cdots & S_{\substack{2N\\12}} \\ \vdots & \vdots & \ddots & \vdots & \vdots & \vdots & \ddots & \vdots \\ S_{\substack{N1\\11}} & S_{\substack{N2\\11}} & \cdots & S_{\substack{NN\\11}} & S_{\substack{N1\\12}} & S_{\substack{N2\\12}} & \cdots & S_{\substack{NN\\12}} \\ S_{\substack{11\\21}} & S_{\substack{12\\21}} & \cdots & S_{\substack{1N\\21}} & S_{\substack{11\\22}} & S_{\substack{12\\22}} & \cdots & S_{\substack{1N\\22}} \\ S_{\substack{21\\21}} & S_{\substack{22\\21}} & \cdots & S_{\substack{2N\\21}} & S_{\substack{21\\22}} & S_{\substack{22\\22}} & \cdots & S_{\substack{2N\\22}} \\ \vdots & \vdots & \ddots & \vdots & \vdots & \vdots & \ddots & \vdots \\ S_{\substack{N1\\21}} & S_{\substack{N2\\21}} & \cdots & S_{\substack{NN\\21}} & S_{\substack{N1\\22}} & S_{\substack{N2\\22}} & \cdots & S_{\substack{NN\\22}} \end{pmatrix} \tag{A.15}$$

where the term $S_{\substack{ab\\cd}}$ indicates the power ratio between the outgoing wave on the ath-mode at the port c under an incident signal on the bth-mode at the port d. Sometimes is useful to subdivide this matrix into four submatrices, according to the ports of the incident and outgoing waves:

$$[S] = \begin{pmatrix} [S]_{11} & [S]_{12} \\ [S]_{21} & [S]_{22} \end{pmatrix} \tag{A.16}$$

Hence, the submatrix $[S]_{21}$ is an $N \times N$ matrix listing all the modal power ratios between outgoing waves at the output-port under incident waves at the input-port; and similarly for the rest of subma-

trices in (A.16). A similar notation has been followed for the multimode impedance matrix $[Z]$ in Sec. 4.5.

A procedure for the computation of the $[S]$ matrix terms is shown in Fig. A.2. This is an extension of the technique outlined in Sec. A.1 for single-mode networks. The procedure is to load all the modal ports with their corresponding characteristic impedance Z_0^k and switch a voltage source on at each modal port in successive steps. In such situation, the source will excite the network with a single-mode incident wave, meanwhile the matched impedances prevent from the incidence of more waves due to reflections. Hence, we can compute the $2N$ scattering terms for a given incident positition. This technique is repeated for all the modal ports (it is $2N$ times) until complete the scattering matrix $[S]$. 3 of these steps are shown in Fig. A.2.

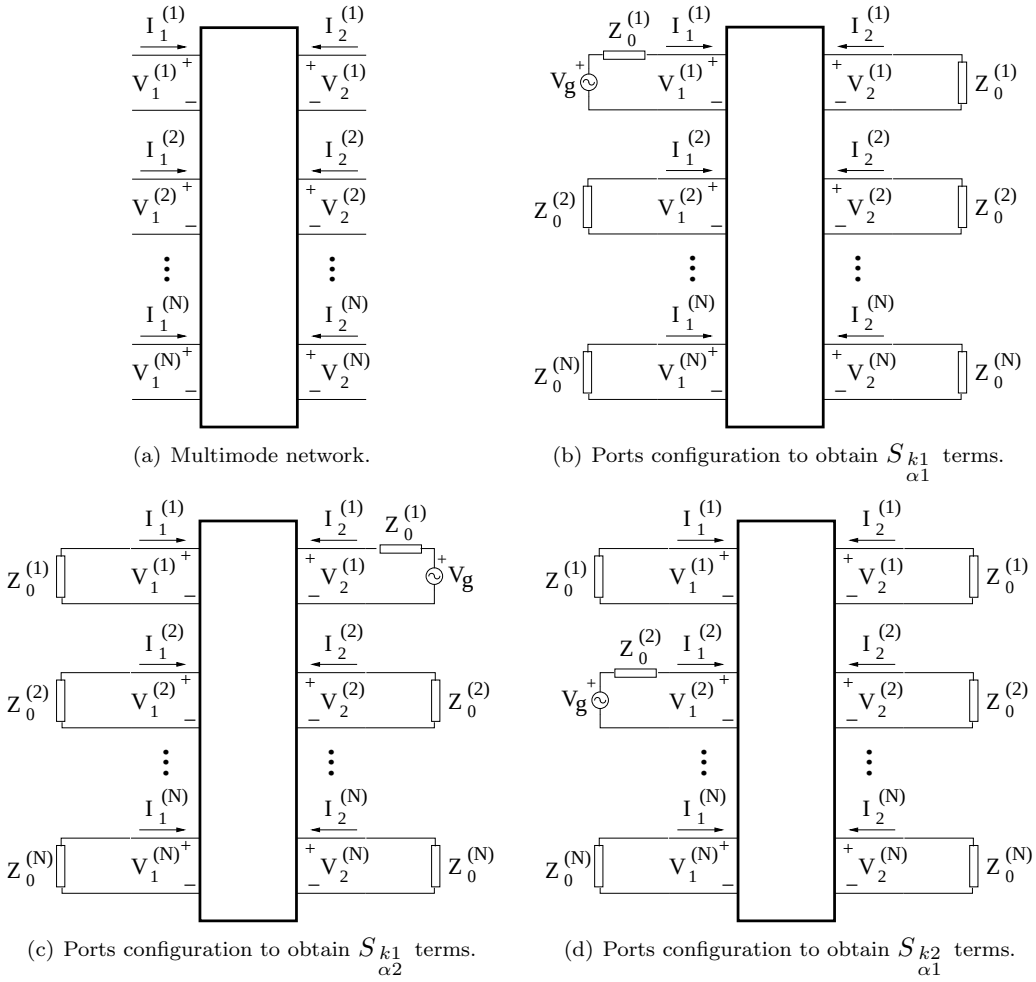

(a) Multimode network.

(b) Ports configuration to obtain $S_{\substack{k1\\ \alpha 1}}$ terms.

(c) Ports configuration to obtain $S_{\substack{k1\\ \alpha 2}}$ terms.

(d) Ports configuration to obtain $S_{\substack{k2\\ \alpha 1}}$ terms.

Figure A.2: Configuration of the ports of a multimode network to obtain the terms of the generalized scattering matrix. The voltage source should be alternately placed at the different modal ports of the network in order to obtain all the terms of the scattering matrix ($2N$ terms per position). In the captions, k indicates the mode ($k = 1 \ldots N$); $\alpha = \{1, 2\}$, where $\alpha = 1$ means input-port and $\alpha = 2$ stands for output-port.

Appendix B

Calculation details for Fourier Analysis

B.1 Fourier Transform

Fourier analysis is the subject area of Mathematics devoted to the study of general functions as sum of trigonometric functions. The procedure by which the original function is decomposed into a sum of trigonometric functions is called Fourier transform. In Physics and Engineering, Fourier transform is used to find the spectrum representation $F(\omega)$ of a time-domain function $f(t)$. Both functions are said to form a Fourier pair. There are several common conventions for defining this operation, which differ in the constant term of the transform kernel. The definition followed in this Thesis is:

$$\mathcal{FT}\{f(t)\} = \quad F(\omega) = \int_{-\infty}^{\infty} f(t)\ e^{-i\,\omega\,t}\,dt \qquad \text{(Direct transform)} \tag{B.1a}$$

$$\mathcal{FT}^{(-1)}\{F(\omega)\} = \quad f(t) = \tfrac{1}{2\,\pi} \int_{-\infty}^{\infty} F(\omega)\ e^{i\,\omega\,t}\,d\omega \qquad \text{(Inverse transform)} \tag{B.1b}$$

From this definition, some important properties of Fourier transforms are derived:

$$\mathcal{FT}\{c_1 f_1(t) + c_2 f_2(t)\} = \quad c_1 F_1(\omega) + c_2 F_2(\omega) \qquad \text{(Linearity)} \tag{B.2a}$$

$$\mathcal{FT}\left\{\int_{-\infty}^{t} f(\tau)\,d\tau\right\} = \quad \tfrac{1}{i\omega} F(\omega) \qquad \text{(Integration)} \tag{B.2b}$$

$$\mathcal{FT}\left\{\frac{d^n f(t)}{d\,t^n}\right\} = \quad (i\omega)^n F(\omega) \qquad \text{(Derivation)} \tag{B.2c}$$

$$\mathcal{FT}\{f(t) \otimes g(t)\} = \quad F(\omega) \cdot G(\omega) \qquad \text{(Convolution)} \tag{B.2d}$$

$$\mathcal{FT}\{f(t-T)\} = \quad F(\omega)\ e^{-i\,\omega\,T} \qquad \text{(Shifting)} \tag{B.2e}$$

$$\mathcal{FT}\{a f(t)\} = \quad \tfrac{1}{|a|} F\left(\tfrac{\omega}{a}\right) \qquad \text{(Scaling)} \tag{B.2f}$$

$$\mathcal{FT}\{F(t)\} = \quad f(-\omega) \qquad \text{(Duality)} \tag{B.2g}$$

where $F(\omega)$, $F_1(\omega)$, $F_2(\omega)$ and $G(\omega)$ denote the Fourier transforms of $f(t)$, $f_1(t)$, $f_2(t)$ and $g(t)$, respectively; a, c_1 and c_2 are complex numbers; T is real, and n is an integer. The Fourier transform of a generic function can be found applying the preceeding properties. Next, we present the Fourier pairs [82, 83] used in the calculations of Chapter 5:

$$\mathcal{FT}\{\delta(t)\} = 1 \tag{B.3a}$$

$$\mathcal{FT}\{\theta(t)\} = \frac{1}{i\,\omega} \tag{B.3b}$$

$$\mathcal{FT}\left\{ e^{-a\,|t|}\right\} = \frac{2\,a}{\omega^2 + a^2} \tag{B.3c}$$

$$\mathcal{FT}\left\{ e^{-a\,t^2}\right\} = \sqrt{\frac{\pi}{a}}\; e^{-\frac{\omega^2}{4\,a}} \tag{B.3d}$$

Note that (B.3b) is derived after applying (B.2b) to (B.3a).

B.2 Dirac delta, Heaviside step and Sign functions

The Dirac delta function δ is a mathematical instrument on the real number line that is zero everywhere except at zero, where it is infinite, and with an integral of one over the entire real line. It can be defined by the following expressions:

$$\delta(x) = \begin{cases} \infty & x = 0 \\ 0 & x \neq 0 \end{cases} \tag{B.4}$$

$$\int_{-\infty}^{+\infty} \delta(x)dx = 1 \tag{B.5}$$

The Dirac delta cannot be considered a function in a rigurous sense because of its properties. It is a mathematical abstraction useful for representing limits and idealized impulses. In this sense, the following definition of δ as the limit of a Gaussian impulse is also very extended:

$$\delta(x) = \lim_{\epsilon \to 0} \frac{1}{\epsilon\sqrt{\pi}}\; e^{-\frac{x^2}{\epsilon^2}} \tag{B.6}$$

Sometimes, it is more preferable to deal with the Dirac delta as a distribution or a measure. From a practical point of view, the Dirac delta only makes sense when it appears inside an integral. It is then when the basic properties of this function can be derived. The properties of the Dirac delta function that have been used in this document are:

$$\delta(ax) = \tfrac{1}{|a|}\delta(x) \quad \text{(Scaling)} \tag{B.7a}$$

$$\delta(x) = \delta(-x) \quad \text{(symmetry)} \tag{B.7b}$$

$$\int_{-\infty}^{+\infty} f(x-a)\delta(x)dx = f(a) \quad \text{(Shifting)} \tag{B.7c}$$

$$\delta(f(x)) = \sum_n \frac{\delta(x-x_n)}{|f'(x_n)|} \quad \text{(Composition)} \tag{B.7d}$$

where a is real number different from zero and $f(x)$ is a function with roots at x_n. The Fourier transform of the Dirac delta function (see (B.3a)) can be found by (B.7c):

$$\mathcal{FT}\left\{\delta(t)\right\} \;=\; \int_{-\infty}^{+\infty} \delta(t)\;\, e^{-i\,\omega\,t} dt \;=\; \left. e^{-i\,\omega\,t}\right|_{t=0} \;=\; 1$$

The analog of the Dirac delta function on the integer number line is called the Kronecker delta:

$$\delta_{mn} \;=\; \begin{cases} 1 & m = n \\ 0 & m \neq n \end{cases} \tag{B.8}$$

The Kronecker delta has similar properties like the Dirac delta. It is also useful to represent discrete distributions, becuase the total sum of this function over the integer number line equals 1:

$$\sum_{n=-\infty}^{\infty} \delta_{mn} = 1 \tag{B.9}$$

Below, we present two functions closely related with the Dirac delta: the Heaviside step and the sign functions. The Heaviside step function $\theta(x)$ is a discontinuous function of the real numbers, which is zero for negative argument and one for non-negative argument:

$$\theta(x) \;=\; \begin{cases} 1 & x \geq 0 \\ 0 & x < 0 \end{cases} \tag{B.10}$$

The Heaviside step function is the integral of the Dirac delta:

$$\theta(x) \;=\; \int_{-\infty}^{x} \delta(\tau)\, d\tau \tag{B.11}$$

The properties of this function significant for this work are:

$$\theta(|a|\, x) \;=\; \theta(x) \tag{B.12a}$$

$$\delta(x-a)\,\theta(x) \;=\; \delta(x-a)\,\theta(a) \tag{B.12b}$$

a being a real number. (B.12a) can be demonstrated using (B.7a):

$$\theta(|a|\, x) \;=\; \int_{-\infty}^{|a|\,x} \delta(\tau)\, d\tau \;=\; |a| \int_{-\infty}^{x} \delta(|a|\tau)\, d\tau \;=\; \frac{|a|}{|a|} \int_{-\infty}^{x} \delta(\tau)\, d\tau \;=\; \theta(x)$$

The sign function $u(x)$ extracts the sign of a real number:

$$u(x) \;=\; \begin{cases} 1 & x > 0 \\ 0 & x = 0 \\ -1 & x < 0 \end{cases} \tag{B.13}$$

The properties of the sign function used in this work are listed now:

$$\frac{d\,|x|}{d\,x} = u(x) \tag{B.14a}$$

$$u(x) = 2\theta(x) - 1 \tag{B.14b}$$

$$\frac{d\,u(x)}{d\,x} = 2\delta(x) \tag{B.14c}$$

$$u(x) = \theta(x) - \theta(-x) \tag{B.14d}$$

Appendix C

Derivation of the electromagnetic fields radiated by charges distributions within waveguides

C.1 Electromagnetic fields radiated by a point charge travelling at constant velocity

The calculation of the electromagnetic fields in the frequency-domain (5.14) and in the time-domain (5.15), as well as the δ-wake function (5.17) is detailed in this section. The analysis starts from the current density given in (5.13), here rewritten for convenience:

$$\vec{J}(\vec{r}\,',\omega) \;=\; q\,\delta(x'-x_0)\,\delta(y'-y_0)\,e^{-i\omega\,z'/v}\,\widehat{z} \tag{C.1}$$

As seen in Sec. 2.4, Green's function connects fields with their sources by the expression

$$\vec{E}(\vec{r},\omega) \;=\; \int\limits_{V'} \overline{\overline{G}}_e(\vec{r},\vec{r}\,',\omega)\cdot\vec{J}(\vec{r}\,',\omega)\,dV' \tag{C.2a}$$

$$\vec{H}(\vec{r},\omega) \;=\; \int\limits_{V'} \overline{\overline{G}}_h(\vec{r},\vec{r}\,',\omega)\cdot\vec{J}(\vec{r}\,',\omega)\,dV' \tag{C.2b}$$

The cartesian components of the electric fields will be derived next. The derivation procedure for the magnetic field is similar and it has been omitted here. Lets start with the transverse electric field:

$$\vec{E}_\perp(\vec{r},\omega) \;=\; \int_{V'} \overline{\overline{G}}_{e_{\perp z}}(\vec{r},\vec{r}\,',\omega)\cdot\vec{J}(\vec{r}\,',\omega)\,dV' \tag{C.3}$$

where $\overline{\overline{G}}_{e_{\perp z}}$ is the longitudinal-source to transverse-field component of the Green's function (2.41), which is

$$\overline{\overline{G}}_{e_{\perp z}}(\vec{r},\vec{r}\,',\omega) \;=\; \frac{1}{i\,2\,\omega\,\varepsilon_0}\,u(z-z')\,\sum_{m=1}^{\infty} k_{t_m}^2\;\vec{e}_{\perp_m}^{TM}(\vec{r}_\perp)\,\phi_m^{TM}(\vec{r}_\perp{}')\;\;e^{-i\,k_{z_m}\,|z-z'|}\,\hat{z} \tag{C.4}$$

Combining (C.1), (C.3) and (C.4), we have

$$\vec{E}_\perp(\vec{r},\omega) \;=\; \frac{q}{i\,2\,\omega\,\varepsilon_0}\sum_{m=1}^{\infty} k_{t_m}^2\;\vec{e}_{\perp m}^{TM}(\vec{r}_\perp)\iint\limits_{CS'}\delta(x'-x_0)\delta(y'-y_0)\phi_m^{TM}(\vec{r}_\perp{}')\,dS' \int\limits_{-\infty}^{+\infty} u(z-z')\;e^{-i\,k_{z_m}\,|z-z'|}\;e^{-i\frac{\omega\,z'}{v}}\,dz' \tag{C.5}$$

At this point, it is preferable to solve separately the integrals in the right brace of the last equation:

$$\vec{E}_\perp(\vec{r},\omega) \;=\; \frac{q}{i\,2\,\omega\,\varepsilon_0}\sum_{m=1}^{\infty} k_{t_m}^2\;\vec{e}_{\perp m}^{TM}(\vec{r}_\perp)\,I_{\perp\perp_m}^{TM}(x_0,y_0)\,I_{\perp z_m}(z,\omega) \tag{C.6}$$

where we define

$$I_{\perp\perp_m}^{TM}(x_0,y_0) \;=\; \iint\limits_{CS'}\delta(x'-x_0)\delta(y'-y_0)\phi_m^{TM}(\vec{r}_\perp{}')\,dS' \tag{C.7a}$$

$$I_{\perp z_m}(z,\omega) \;=\; \int\limits_{-\infty}^{+\infty} u(z-z')\;e^{-i\,k_{z_m}\,|z-z'|}\;e^{-i\frac{\omega\,z'}{v}}\,dz' \tag{C.7b}$$

The solution of the first integral is simply

$$I_{\perp\perp_m}^{TM}(x_0,y_0) \;=\; \phi_m^{TM}(x_0,y_0) \tag{C.8}$$

where the shifting property (B.7c) of the Dirac delta has been used. At this point, the time-domain transverse electric field can be expressed as:

$$\vec{\mathcal{E}}_\perp(\vec{r},t) \;=\; \frac{q}{2\,\varepsilon_0}\sum_{m=1}^{\infty} k_{t_m}^2\;\vec{e}_{\perp m}^{TM}(\vec{r}_\perp)\,\phi_m^{TM}(x_0,y_0)\,\mathcal{FT}^{(-1)}\left\{\frac{1}{i\,\omega}\,I_{\perp z_m}(z,\omega)\right\} \tag{C.9}$$

It seems that this equation can be directly solved by means of the integration property of Fouier transform (B.2b). Unfortunately, the propagation factor k_{z_m} in $I_{\perp z_m}$ is frequency dependent, what forces to solve (C.7b) before tackle (C.9). The first step in the solution of $I_{\perp z_m}$ is to use the equality (B.14d) into (C.7b):

$$I_{\perp z_m}(z,\omega) \;=\; \int\limits_{-\infty}^{+\infty}\theta(z-z')\;e^{-i\,k_{z_m}(z-z')}\;e^{-i\frac{\omega\,z'}{v}}\,dz' - \int\limits_{-\infty}^{+\infty}\theta(z'-z)\;e^{-i\,k_{z_m}(z'-z)}\;e^{-i\frac{\omega\,z'}{v}}\,dz' \tag{C.10}$$

Then, the substitutions $t'=z-z'$ in the first integral and $t'=z'-z$ in the second integral give:

$$I_{\perp z_m}(z,\omega) \;=\; \int\limits_{-\infty}^{+\infty}\theta(t')\;e^{-i\,k_{z_m}t'}\;e^{-i(z-t')\frac{\omega}{v}}\,dt' - \int\limits_{-\infty}^{+\infty}\theta(t')\;e^{-i\,k_{z_m}t'}\;e^{-i(t'-z)\frac{\omega}{v}}\,dt' \tag{C.11}$$

and after common factoring:

$$I_{\perp z_m}(z,\omega) \;=\; e^{-i\omega\frac{z}{v}}\left[\int_{-\infty}^{+\infty}\theta(t')\;e^{-i\left(k_{z_m}-\frac{\omega}{v}\right)t'}\,dt' - \int_{-\infty}^{+\infty}\theta(t')\;e^{-i\left(k_{z_m}+\frac{\omega}{v}\right)t'}\,dt'\right] \tag{C.12}$$

The integrals in the previous equation can be treated as Fourier integrals of transformed domains $\omega' = k_{z_m} - \frac{\omega}{v}$ and $\omega' = k_{z_m} + \frac{\omega}{v}$, respectively. Thus, knowing (B.3b) we obtain:

$$I_{\perp z_m}(z,\omega) \;=\; e^{-i\omega\frac{z}{v}}\left[\frac{1}{i\left(k_{z_m}-\frac{\omega}{v}\right)} - \frac{1}{i\left(k_{z_m}+\frac{\omega}{v}\right)}\right] \tag{C.13}$$

and therefore

$$I_{\perp z_m}(z,\omega) \;=\; \frac{2\left(\frac{\omega}{v}\right)}{i\left(k_{z_m}^2-\left(\frac{\omega}{v}\right)^2\right)}\;e^{-i\omega\frac{z}{v}} \tag{C.14}$$

Hence, the tansverse electric field in the frequency-domain from (C.6) is:

$$\vec{E}_\perp(\vec{r},\omega) \;=\; -\frac{q\;e^{-i\omega\frac{z}{v}}}{v\,\varepsilon_0}\sum_{m=1}^{\infty}\frac{k_{t_m}^2}{k_{z_m}^2-\left(\frac{\omega}{v}\right)^2}\,\vec{e}_{\perp m}^{\,TM}(\vec{r}_\perp)\,\phi_m^{TM}(x_0,y_0) \tag{C.15}$$

Now, the derivation of the time-domain transverse electric field is accomplished, starting from

$$\vec{\mathcal{E}}_\perp(\vec{r},t) \;=\; -\frac{q}{v\,\varepsilon_0}\sum_{m=1}^{\infty}k_{t_m}^2\,\vec{e}_{\perp m}^{\,TM}(\vec{r}_\perp)\,\phi_m^{TM}(x_0,y_0)\,\mathcal{FT}^{(-1)}\left\{\frac{1}{k_{z_m}^2-\left(\frac{\omega}{v}\right)^2}\;e^{-i\omega\frac{z}{v}}\right\} \tag{C.16}$$

It is necessary to solve

$$I_{\perp z_m}^{(-1)}(z,t) \;=\; \mathcal{FT}^{(-1)}\left\{\frac{1}{k_{z_m}^2-\left(\frac{\omega}{v}\right)^2}\;e^{-i\omega\frac{z}{v}}\right\} \tag{C.17}$$

At this point, the dependence on the frequency of k_{z_m} should be clearly stated:

$$I_{\perp z_m}^{(-1)}(z,t) \;=\; \mathcal{FT}^{(-1)}\left\{\frac{1}{\left(\frac{\omega}{c}\right)^2-k_{t_m}^2-\left(\frac{\omega}{v}\right)^2}\;e^{-i\omega\frac{z}{v}}\right\} \;=\; \mathcal{FT}^{(-1)}\left\{\frac{1}{\omega^2\left(\frac{1}{c^2}-\frac{1}{v^2}\right)-k_{t_m}^2}\;e^{-i\omega\frac{z}{v}}\right\} \tag{C.18}$$

and from the definition of the relativistic factor γ:

$$I_{\perp z_m}^{(-1)}(z,t) \;=\; \mathcal{FT}^{(-1)}\left\{-\frac{(v\,\gamma)^2}{\omega^2+(v\,\gamma\,k_{t_m})^2}\;e^{-i\omega\frac{z}{v}}\right\} \tag{C.19}$$

Using (B.3c) and (B.2e), we have

$$I_{\perp z_m}^{(-1)}(z,t) \;=\; -\frac{v\,\gamma}{2\,k_{t_m}}\,\mathcal{FT}^{(-1)}\left\{\frac{2\,(v\,\gamma\,k_{t_m})}{\omega^2+(v\,\gamma\,k_{t_m})^2}\;e^{-i\omega\frac{z}{v}}\right\} \;=\; -\frac{v\,\gamma}{2\,k_{t_m}}\;e^{-v\,\gamma\,k_{t_m}|t-z/v|} \tag{C.20}$$

Consequently, the tansverse electric field in the time-domain is:

$$\vec{\mathcal{E}}_\perp(\vec{r},t) \;=\; \frac{q\,\gamma}{2\,\varepsilon_0}\sum_{m=1}^{\infty} k_{t_m}\,\vec{e}^{TM}_{\perp_m}(\vec{r}_\perp)\,\phi_m^{TM}(x_0,y_0)\;\; e^{-v\,\gamma\,k_{t_m}|t-z/v|} \tag{C.21}$$

The longitudinal electric field is analysed next. The Green's function states that the longitudinal electric field radiated by a charge density moving in the z-direction is

$$\vec{E}_z(\vec{r},\omega) \;=\; \int_{V'} \overline{\overline{G}}_{e_{zz}}(\vec{r},\vec{r}\,',\omega)\cdot\vec{J}(\vec{r}\,',\omega)\,dV' \tag{C.22}$$

where $\overline{\overline{G}}_{e_{zz}}$ is the zz-component of the electric field Green's function (2.41), which is

$$\overline{\overline{G}}_{e_{zz}}(\vec{r},\vec{r}\,',\omega) \;=\; -\frac{1}{2\,\omega\,\varepsilon_0}\sum_{m=1}^{\infty}\frac{k_{t_m}^4}{k_{z_m}}\phi_m^{TM}(\vec{r}_\perp)\,\phi_m^{TM}(\vec{r}_\perp{}')\;\; e^{-i\,k_{z_m}\,|z-z'|}\,\hat{z}\,\hat{z} \tag{C.23}$$

Thus, we can write

$$\vec{E}_z(\vec{r},\omega) \;=\; \frac{q}{2\,\omega\,\varepsilon_0}\sum_{m=1}^{\infty}\frac{k_{t_m}^4}{k_{z_m}}\phi_m^{TM}(\vec{r}_\perp)\,\phi_m^{TM}(x_0,y_0)\,I_{zz_m}(z,\omega)\,\hat{z} \tag{C.24}$$

where the following parameter has been defined:

$$I_{zz_m}(z,\omega) \;=\; \int_{-\infty}^{+\infty} e^{-i\,k_{z_m}\,|z-z'|}\;\; e^{-i\frac{\omega\,z'}{v}}\,dz' \tag{C.25}$$

The parameter I_{zz_m} can be solved following a similar procedure as shown for $I_{\perp z_m}$:

$$I_{zz_m}(z,\omega) \;=\; \int_{-\infty}^{+\infty}\theta(\psi)\;\; e^{-i\,k_{z_m}\psi}\;\; e^{-i(z-\psi)\frac{\omega}{v}}\,d\psi + \int_{-\infty}^{+\infty}\theta(\psi)\;\; e^{-i\,k_{z_m}\psi}\;\; e^{-i(\psi-z)\frac{\omega}{v}}\,d\psi \tag{C.26}$$

$$I_{zz_m}(z,\omega) \;=\; \;\; e^{-i\omega\frac{z}{v}}\left[\frac{1}{i\left(k_{z_m}-\frac{\omega}{v}\right)}+\frac{1}{i\left(k_{z_m}+\frac{\omega}{v}\right)}\right] \tag{C.27}$$

And simplifying

$$I_{zz_m}(z,\omega) \;=\; \frac{2\,k_{z_m}}{i\left(k_{z_m}^2-\left(\frac{\omega}{v}\right)^2\right)}\;\; e^{-i\omega\frac{z}{v}} \tag{C.28}$$

Thus, the longitudinal electric field in the frequency-domain is:

$$\vec{E}_z(\vec{r},\omega) \;=\; \frac{q}{i\,\omega\,\varepsilon_0}\sum_{m=1}^{\infty}\frac{k_{t_m}^4}{k_{z_m}^2-\left(\frac{\omega}{v}\right)^2}\phi_m^{TM}(\vec{r}_\perp)\,\phi_m^{TM}(x_0,y_0)\;\; e^{-i\omega\frac{z}{v}}\,\hat{z} \tag{C.29}$$

The calculation of the time-domain longitudinal electric field is calculated through the inverse Fourier transformation of the previous equation:

$$\vec{\mathcal{E}}_z(\vec{r},t) \;=\; \frac{q}{\varepsilon_0}\sum_{m=1}^{\infty} k_{t_m}^4\;\phi_m^{TM}(\vec{r}_\perp)\,\phi_m^{TM}(x_0,y_0)\mathcal{FT}^{(-1)}\left\{\frac{1}{i\,\omega}\;\frac{1}{k_{z_m}^2-\left(\frac{\omega}{v}\right)^2}\;\; e^{-i\omega\frac{z}{v}}\right\}\hat{z} \tag{C.30}$$

It is necessary to solve

$$I_{zz_m}^{(-1)}(z,t) \;=\; \mathcal{FT}^{(-1)}\left\{\frac{1}{i\,\omega}\,\frac{1}{k_{z_m}^2-\left(\frac{\omega}{v}\right)^2}\;e^{-i\omega\frac{z}{v}}\right\} \tag{C.31}$$

Note that $I_{zz_m}^{(-1)}$ is the primitive integral of $I_{\perp z_m}^{(-1)}$, so it can be solved applying the integrative property of Fourier Transforms (B.2b):

$$I_{zz_m}^{(-1)}(z,t) \;=\; \int_{-\infty}^{t} I_{\perp z_m}^{(-1)}(z,\tau)\,d\tau \;=\; -u(t-z/v)\,\frac{1}{2\,k_{t_m}^2}\;e^{-v\,\gamma\,k_{t_m}|t-z/v|} \tag{C.32}$$

where the expression (B.14a) has been used. Thus, we have:

$$\vec{\mathcal{E}}_z(\vec{r},t) \;=\; -u(t-z/v)\frac{q}{2\,\varepsilon_0}\sum_{m=1}^{\infty}k_{t_m}^2\;\phi_m^{TM}(\vec{r}_\perp)\,\phi_m^{TM}(x_0,y_0)\;\;e^{-v\,\gamma\,k_{t_m}|t-z/v|}\,\hat{z} \tag{C.33}$$

The derivation of the δ-function wake potential (5.17) from the definition given in (5.1) is detailed now. First of all, the time-domain field expression (5.15) is used in (5.1):

$$\begin{aligned}\vec{w}_\perp(\vec{r},\vec{r}',s) \;&=\; \frac{\gamma}{2\;\varepsilon_0}\sum_m k_{t_m}\vec{e}_m^{TM}(\vec{r}_\perp)\phi_m^{TM}(x_0,y_0)\,I_m^{(1)}\\ &\quad+\frac{v^2\;\gamma\;\mu_0}{2}\sum_m k_{t_m}\phi_m^{TM}(x_0,y_0)\Big(\hat{z}\times\vec{h}_m^{TM}(\vec{r}_\perp)\Big)\,I_m^{(1)}\end{aligned} \tag{C.34a}$$

$$w_z(\vec{r},\vec{r}',s) \;=\; \frac{1}{2\varepsilon_0}\sum_m k_{t_m}^2\phi_m^{TM}(\vec{r}_\perp)\phi_m^{TM}(x_0,y_0)\,I_m^{(2)} \tag{C.34b}$$

where the following integrals have been introduced:

$$I_m^{(1)} \;\equiv\; \int_0^L \;e^{-k_{t_m}\gamma|vt-z|}\Big|_{t=\frac{z+s}{v}}\;dz \tag{C.35a}$$

$$I_m^{(2)} \;\equiv\; \int_0^L u\left(t-\frac{z}{v}\right)\;e^{-k_{t_m}\gamma|vt-z|}\Big|_{t=\frac{z+s}{v}}\;dz \tag{C.35b}$$

The solution of these integrals is:

$$I_m^{(1)} \;=L\;e^{-k_{t_m}\gamma|s|} \tag{C.36a}$$

$$I_m^{(2)} \;=L\,u\left(\frac{s}{v}\right)\;e^{-k_{t_m}\gamma|s|} \tag{C.36b}$$

On the other hand, knowing that $\hat{z}\times\vec{h}_m=-\vec{e}_m$ and $v^2\gamma\mu_0/2=\gamma/(2\varepsilon_0)-1/(2\gamma\varepsilon_0)$, the transverse component (C.34a) can be simplified as

$$\vec{w}_\perp(\vec{r},\vec{r}',s) \;=\; \frac{1}{2\;\gamma\;\varepsilon_0}\sum_m k_{t_m}\vec{e}_m^{TM}(\vec{r}_\perp)\phi_m^{TM}(x_0,y_0)\,I_m^{(1)} \tag{C.37}$$

Finally, assuming positive distance s, the previous expressions derive into the equation (5.17).

C.2 Electromagnetic fields radiated by a 3-dimensional Gaussian distribution travelling at constant velocity

The derivation of the time-domain electric fields given in Sec. 5.5.4 is detailed in this section of the present appendix. The analysis followed is similar for the magnetic field derivation. We start the analysis from the frequency-domain fields (5.34). The transverse electric field is:

$$\vec{E}_{\perp}^{(\text{3D-Gauss})}(\vec{r},\omega) \;=\; \frac{Q}{2\,\pi\,v\,\varepsilon_0\,\sigma_x\,\sigma_y}\;\; e^{-\frac{1}{2}\left(\frac{\sigma_z\,\omega}{v}\right)^2}\;\; e^{-i\,\frac{\omega\,z}{v}}\;\sum_{m=1}^{\infty}\; k_{t_m}^2\;\vec{e}_m^{\,TM}(\vec{r}_{\perp})\;\frac{1}{\left(\frac{\omega}{v}\right)^2-k_{z_m}^2}\;I_{\perp\perp_m}^{TM}(x_0,y_0) \tag{C.38}$$

The transformation to the time-domain of the last expression involves the solution of the following inverse Fourier transformation:

$$T_{\perp} \;=\; \mathcal{FT}^{(-1)}\left\{\frac{e^{-\frac{1}{2}\left(\frac{\sigma_z\,\omega}{v}\right)^2}\;\; e^{-i\,\frac{\omega\,z}{v}}}{\left(\frac{\omega}{v}\right)^2-k_{z_m}^2}\right\} \tag{C.39}$$

which can be solved applying the convolution property of Fourier Transforms (B.2d). In this case:

$$T_{\perp} \;=\; FT^{(-1)}\left\{F_{\perp}(\omega)\,G(\omega)\;\; e^{-i\,\frac{\omega\,z}{v}}\right\} \tag{C.40}$$

where the functions $F_{\perp}(\omega)$ and $G(\omega)$ are defined as

$$F_{\perp}(\omega) \;=\; \frac{1}{\left(\frac{\omega}{v}\right)^2-k_{z_m}^2} \tag{C.41a}$$

$$G(\omega) \;=\; e^{-\frac{1}{2}\left(\frac{\sigma_z\,\omega}{v}\right)^2} \tag{C.41b}$$

The exponential term in (C.40) will be omitted during the convolution process, to finally be applied as a time shifting. The inverse Fourier transform of $F_{\perp}(\omega)$ has been previously solved for the punctual charge case (see (C.17)). Its solution is:

$$\mathcal{FT}^{(-1)}\left\{F_{\perp}(\omega)\right\} \;=\; \frac{v\,\gamma}{2\,k_{t_m}}\;\; e^{-k_{t_m}\,\gamma\,v\,|t|} \tag{C.42}$$

On the other hand, the inverse Fourier transform of $G(\omega)$ can be found applying (B.3d):

$$FT^{(-1)}\left\{G(\omega)\right\} \;=\; \frac{v}{\sqrt{2\,\pi}\,\sigma_z}\;\; e^{-\frac{1}{2}\left(\frac{v\,t}{\sigma_z}\right)^2} \tag{C.43}$$

Thus, omitting the shifting term, $T_{\perp}$ can be expressed as

$$T_{\perp} \;=\; K\,\left(\;\; e^{-M\,|t|}\right)\;\otimes\;\left(\;\; e^{-\frac{1}{2}\left(\frac{t}{N}\right)^2}\right) \tag{C.44}$$

where the following auxiliar parameters have been introduced:

$$K \;=\; \frac{\gamma\,v^2}{2\,\sqrt{2\,\pi}\,\sigma_z\,k_{t_m}} \tag{C.45a}$$

$$M \;=\; k_{t_m}\,\gamma\,v \tag{C.45b}$$

$$N \;=\; \frac{\sigma_z}{v} \tag{C.45c}$$

The resulting convolution has been solved thanks to the software tool *Mathematica8.0*[84]:

$$T_\perp \;=\; K\,N\sqrt{\frac{\pi}{2}}\;\; e^{\frac{1}{2}(M\,N)^2}\;\left[\;\; e^{M\,t}\,erfc\left(\frac{M\,N}{\sqrt{2}}+\frac{t}{\sqrt{2}\,N}\right)+\;\; e^{-M\,t}\,erfc\left(\frac{M\,N}{\sqrt{2}}-\frac{t}{\sqrt{2}\,N}\right)\right] \tag{C.46}$$

The time-shifting term is applied now, leading to:

$$T_\perp = K\,N\sqrt{\frac{\pi}{2}}\;\; e^{\frac{1}{2}(M\,N)^2}\;\left[\;\; e^{M\,(t-\frac{z}{v})}\,erfc\left(\frac{M\,N}{\sqrt{2}}+\frac{(t-\frac{z}{v})}{\sqrt{2}\,N}\right)+\;\; e^{-M\,(t-\frac{z}{v})}\,erfc\left(\frac{M\,N}{\sqrt{2}}-\frac{(t-\frac{z}{v})}{\sqrt{2}\,N}\right)\right] \tag{C.47}$$

And substituying the parameters K, M and N:

$$\begin{aligned} T_\perp \;=& \frac{\gamma\,v}{4\,k_{t_m}}\;\; e^{\frac{1}{2}(k_{t_m}\,\gamma\,\sigma_z)^2} \\ & \left[\;\; e^{-k_{t_m}\,\gamma(z-vt)}\,erfc\left(\frac{k_{t_m}\,\gamma\,\sigma_z}{\sqrt{2}}-\frac{(z-vt)}{\sqrt{2}\,\sigma_z}\right)+\;\; e^{k_{t_m}\,\gamma(z-vt)}\,erfc\left(\frac{k_{t_m}\,\gamma\,\sigma_z}{\sqrt{2}}+\frac{(z-vt)}{\sqrt{2}\,\sigma_z}\right)\right] \end{aligned} \tag{C.48}$$

Hence, the transverse electric field in the time-domain is:

$$\begin{aligned} \vec{\mathcal{E}}_\perp^{(\text{3D-Gauss})}(\vec{r},t) \;=\; \frac{Q\,\gamma}{8\,\pi\,\sigma_x\,\sigma_y\,\varepsilon_0}\;\sum_{m=1}^{\infty}\; k_{t_m}\,\vec{e}_m^{TM}(\vec{r}_\perp)\;\; e^{\frac{1}{2}(k_{t_m}\,\gamma\,\sigma_z)^2}\,I_m^{TM}(x_0,y_0) \\ \left[\;\; e^{-k_{t_m}\,\gamma(z-vt)}\,erfc\left(\frac{k_{t_m}\,\gamma\,\sigma_z}{\sqrt{2}}-\frac{(z-vt)}{\sqrt{2}\,\sigma_z}\right)\right. \\ \left.+\;\; e^{k_{t_m}\,\gamma(z-vt)}\,erfc\left(\frac{k_{t_m}\,\gamma\,\sigma_z}{\sqrt{2}}+\frac{(z-vt)}{\sqrt{2}\,\sigma_z}\right)\right] \end{aligned} \tag{C.49}$$

The analysis of the longitudinal component of the electric field is accomplished now. Starting from the frequency-domain expression:

$$\vec{E}_z^{(\text{3D-Gauss})}(\vec{r},\omega) \;=\; \frac{Q}{i\,2\,\pi\,\varepsilon_0\,\sigma_x\,\sigma_y}\;\; e^{-\frac{1}{2}\left(\frac{\sigma_z\,\omega}{v}\right)^2}\;\; e^{-i\,\frac{\omega\,z}{v}}\;\sum_{m=1}^{\infty}\; k_{t_m}^4\,\phi_m^{TM}(\vec{r}_t)\,\frac{1}{\left(\frac{\omega}{v}\right)^2-k_{z_m}^2}\,I_{\perp\perp_m}^{TM}(x_0,y_0)\,\hat{z} \tag{C.50}$$

For this case, is necessary to solve the next inverse Fourier transform:

$$T_z \;=\; \mathcal{FT}^{(-1)}\left\{\frac{1}{i\,\omega}\,\frac{e^{-\frac{1}{2}\left(\frac{\sigma_z\,\omega}{v}\right)^2}}{\left(\frac{\omega}{v}\right)^2-k_{z_m}^2}\;\; e^{-i\,\frac{\omega\,z}{v}}\right\} \tag{C.51}$$

This transform can be solved following the same procedure as for $T_\perp$. This time we have:

$$T_z \;=\; FT^{(-1)}\left\{F_z(\omega)\,G(\omega)\;\; e^{-i\,\frac{\omega\,z}{v}}\right\} \tag{C.52}$$

where the function F_z is

$$F_z(\omega) \;=\; \frac{1}{i\,\omega}\,\frac{1}{\left(\frac{\omega}{v}\right)^2-k_{z_m}^2} \tag{C.53}$$

This function is the Fourier transform of $I^{(-1)}_{zz_m}$, as can be seen in (C.31). Thus, its inverse transform is:

$$FT^{(-1)}\left\{F_z(\omega)\right\} \;=\; -\frac{1}{2\,k_{t_m}^2}\,u(t)\;\; e^{-k_{t_m}\,\gamma\,v\,|t|} \tag{C.54}$$

At this point, omitting the shift $(t - z/v)$, the function $T_\perp$ can be expressed as

$$T_z \;=\; K'\left(u(t)\;\; e^{-M\,|t|}\right) \otimes \left(\;\; e^{-\frac{1}{2}\left(\frac{t}{N}\right)^2}\right) \tag{C.55}$$

where the parameter K' is

$$K' \;=\; -\frac{v}{2\,\sqrt{2\,\pi}\,\sigma_z\,k_{t_m}^2} \tag{C.56}$$

Now, the convolution can be solved using *Mathematica8.0*[84], obtaining:

$$T_z \;=\; -K\,N\,\sqrt{\frac{\pi}{2}}\;\; e^{\frac{1}{2}(M\,N)^2}\;\left[\;\; e^{M\,t}\,erfc\left(\frac{M\,N}{\sqrt{2}}+\frac{t}{\sqrt{2}\,N}\right) -\;\; e^{-M\,t}\,erfc\left(\frac{M\,N}{\sqrt{2}}-\frac{t}{\sqrt{2}\,N}\right)\right] \tag{C.57}$$

and after the time-shifting is applied:

$$T_z = -K\,N\,\sqrt{\frac{\pi}{2}}\;\; e^{\frac{1}{2}(M\,N)^2}\;\left[\;\; e^{M\,(t-\frac{z}{v})}\,erfc\left(\frac{M\,N}{\sqrt{2}}+\frac{(t-\frac{z}{v})}{\sqrt{2}\,N}\right) -\;\; e^{-M\,(t-\frac{z}{v})}\,erfc\left(\frac{M\,N}{\sqrt{2}}-\frac{(t-\frac{z}{v})}{\sqrt{2}\,N}\right)\right] \tag{C.58}$$

The next step is the substitution of the auxiliar parameters K', M and N:

$$\begin{aligned} T_z \;=& \frac{1}{4\,k_{t_m}^2}\;\; e^{\frac{1}{2}(k_{t_m}\,\gamma\,\sigma_z)^2} \\ & \left[\;\; e^{-k_{t_m}\,\gamma(z-vt)}\,erfc\left(\frac{k_{t_m}\,\gamma\,\sigma_z}{\sqrt{2}}-\frac{(z-vt)}{\sqrt{2}\,\sigma_z}\right) -\;\; e^{k_{t_m}\,\gamma(z-vt)}\,erfc\left(\frac{k_{t_m}\,\gamma\,\sigma_z}{\sqrt{2}}+\frac{(z-vt)}{\sqrt{2}\,\sigma_z}\right)\right] \end{aligned} \tag{C.59}$$

And finally, we obtain the time-domain longitudinal component of the electric field radiated by a 3-dimensional Gaussian bunch:

$$\begin{aligned} \vec{\mathcal{E}}_z^{\text{(3D-Gauss)}}(\vec{r},t) \;=\; & \frac{Q}{8\,\pi\,\sigma_x\,\sigma_y\,\varepsilon_0}\sum_{m=1}^{\infty} k_{t_m}^2\,\phi_m^{TM}(\vec{r}_\perp)\;\; e^{\frac{1}{2}(k_{t_m}\,\gamma\,\sigma_z)^2}\,I_m^{TM}(x_0,y_0) \\ & \left[\;\; e^{-k_{t_m}\,\gamma(z-vt)}\,erfc\left(\frac{k_{t_m}\,\gamma\,\sigma_z}{\sqrt{2}}-\frac{(z-vt)}{\sqrt{2}\,\sigma_z}\right)\right. \\ & \left. -\;\; e^{k_{t_m}\,\gamma(z-vt)}\,erfc\left(\frac{k_{t_m}\,\gamma\,\sigma_z}{\sqrt{2}}+\frac{(z-vt)}{\sqrt{2}\,\sigma_z}\right)\right]\,\hat{z} \end{aligned} \tag{C.60}$$

Appendix D

Publications

An up-to-date summary of technical publications in which the PhD candidate has contributed is given in the present appendix. The list spans the complete doctoral period, and therefore some research topics not treated in this Thesis are here included.

- M. F. J. Nogales, J. P. Garcia, J. Hinojosa, and A. A. Melcon, "Genetic algorithms applied to microwave filters optimization and design," in *Progress in Electromagnetic Research Symposium, PIERS Proceedings*, (Cambridge, MA, USA), pp. 99–103, July 2008

  This paper presents improvements in genetic algorithms for the optimization of microwave circuits. It is a continuation of the Final Year Project developed by the PhD candidate for his M. S. degree. In this paper, several novel fitness functions for the optimization process are studied and implemented. They allow to quantify the importance of the specifications and of the solution approach with respect to the ideal circuit performance for a bandpass filter. The performance of the optimization method with different fitness functions is compared for the design of a Ku-band two-pole rectangular iris coupled waveguide bandpass filter.

- F. J. P. Soler, S. Anza, M. Mattes, C. Miquel, F. Quesada, M. Jiménez, J. Gil, C. Vicente, J. R. Mosig, D. Raboso, V. E. Boria, B. Gimeno, and A. Alvarez-Melcon, "Rigorous investigation of RF breakdown effects in high power microstrip passive circuits," in *IEEE International Microwave Symposium, Proceedings of the IEEE, MTT-S*, (Boston, MA, USA), pp. 833–836, June 2009. DOI 10.1109/MWSYM.2009.5165826

  This work presents a new rigorous investigation of corona effects in microstrip components. To carry out the investigation, a new software tool has been developed. The new tool first calculates the electromagnetic fields in complex microstrip structures using a Volume Integral Equation (VIE) formulation. Novel numerical techniques have been incorporated in the VIE to increase the accuracy during the computation of the electromagnetic fields. This includes novel techniques introduced to treat the singularities of the free space Green's functions. Once the electromagnetic fields are computed accurately, corona effects in the relevant structures are investigated. For this, a numerical solution of the free electron density continuity equation has been implemented. The new software developed has been used, for the first time, in the study of corona effects in the neighborhood of coaxial to microstrip transitions, containing flat ribbons.

Numerical results are validated through measurements, showing the accuracy of the developed models.

- J. P. Soler, M. J. Nogales, F. Q. Pereira, and A. A. Melcon, "A novel approach for the evaluation of electromagnetic fields using rigorous wire antenna models," in *IEEE International Symposium on Antennas and Propagation, Proceedings of the IEEE, AP-S*, (Charleston, SC, USA), pp. 1–4, June 2009. DOI 10.1109/APS.2009.5172023

  Wire antennas are a useful approach for studying small cylindrical elements using Integral Equation formulations. For an accurate application of these models in the Method of Moments, some techniques must be derived in order to properly deal with the singularity of the kernel term, which is related to the behavior of the elliptic integral functions. In previous works exact expressions are obtained for the integration of the kernel along wire cells, but as a major drawback they are expressed in terms of infinite summations, which are slowly convergent near the singular condition of the observation point. In this work, an alternative technique is proposed, using a decomposition of the singular elliptic function in terms of a polynomial expansion. This method isolates the real singular term of the elliptic integral in a simple expression that can be performed analytically. The rest of the derived terms are regular, and numerical integration can be employed. Using this semianalytical approach, the different integrals involved in the evaluation of the electromagnetic fields can be evaluated with higher accuracy.

- M. Jiménez, B. Gimeno, C. Miquel-Espanya, D. Raboso, S. Anza, C. Vicente, J. Gil, F. Quesada, A. Alvarez, M. Taroncher, M. Reglero, and V. E. Boria, "Analysis of the electromagnetic radiation generated by a multipactor discharge occurring within a microwave passive component," *Phys. D: Appl. Phys*, vol. 43, p. 395501, 2010. DOI 10.1088/0022-3727/43/39/395501

  Multipactoring is a non-linear phenomenon that appears in high-power microwave equipments operating under vacuum conditions and causes several undesirable effects. In this manuscript, a theoretical and experimental study of the RF spectrum radiated by a multipactor discharge, occurring within a realistic microwave component based on rectangular waveguides, is reported. The electromagnetic coupling of a multipactor current to the fundamental propagative mode of a uniform waveguide has been analyzed in the context of the microwave network theory. The discharge produced under a single-carrier RF voltage regime has been modelled as a shunt current source exciting such a mode in a transmission-line gap-region. By means of a simple equivalent circuit, this model allows predicting the harmonics generated by the discharge occurring in a realistic passive waveguide component. Power spectrum radiated by a third order multipactor discharge has been measured in an E-plane silver-plated waveguide transformer, thus validating qualitatively the presented theory to simulate the noise generated by a single-carrier multipactor discharge.

- B. Gimeno, S. Anza, F. P. Soler, C. Vicente, J. Gil, V. Boria, F. Quesada, M. Jiménez, A. A. Melcon, M. Mattes, J. Mosig, D. Raboso, and C. M. Espana, "Estudio del efecto multipactor en componentes pasivos de microondas para aplicaciones en comunicaciones espaciales," in *VII Encuentro Iberico de Electromagnetismo Computacional*, (Caceres, Spain), May 2010

  In this communication, the authors review the state-of-the-art in the study of the multipactor effect, putting special emphasis on the research activities developed by them to date. Results on multipactor power threshold based on experimental measurements carried out at ESTEC laboratories are used to validate a novel software tool for multipactor simulation and prediction.

- M. Jiménez, B. Gimeno, S. Anza, C. Vicente, J. Gil, A. A. Melcon, F. Quesada, M. Taroncher, M. Reglero, and D. Raboso, "Computation of a multipactor discharge occuring within a realistic passive microwave component," in *7th International Workshop on Multipaction, Corona and Passive Intermodulation in Space RF Hardware, European Space Agency, MULCOPIM'11*, (Valencia, Spain), September 2011

  In this work, the aim of the authors is to study the propagation of the electromagnetic energy radiated by a multipactor discharge inside a passive microwave waveguide component. The radiation of a multipactor current, occurring within a uniform waveguide, is treated as the problem of a time-harmonic current density exciting the waveguide. The harmonic condition of the current density allows one to expand it into a modal series. We have developed an equivalent network for the modes of the current, in order to connect it to a multimodal transmission-lines circuit of the passive component. Thus, the energy radiated by the multipactor event is coupled to the microwave structure. This article is an extension of a previous work of the authors, where a single-mode, first approach to the problem was presented. The actual multimodal processing makes possible to perform more accurate simulations and to study more complex structures. Experimental results are also included for validation. A multipactor test on a silver-plated WR-75 E-plane rectangular waveguide transformer has been carried out. The power spectrum of the fields radiated by a third-order multipactor discharge has been detected and compared with the theoretical results provided by the proposed model, thus demonstrating the capability of the theory to predict qualitatively the distortion generated by a multipactor event. The simulation of the discharge has been computed by a realistic model that follows the evolution in the time of a multipactor discharge. This model takes into account, amongst other effects, the rise and the saturation in the population of electrons, the space charge force, and the spread in the conditions of particles launching.

- M. Jiménez, S. Marini, B. Gimeno, A. A. Melcon, F. Quesada, V. Boria, P. Soto, S. Cogollos, and D. Raboso, "Computation of wakefields in arbitrarily cross-shaped waveguide for particle accelerator applications," in *7th International Workshop on Multipaction, Corona and Passive Intermodulation in Space RF Hardware, European Space Agency, MULCOPIM'11*, (Valencia, Spain), September 2011

  We propose a technique for the calculation of the electromagnetic fields radiated by charges in motion within waveguides. The fields are evaluated from the waveguide geometry and the equation of motion of the charges, by means of the classical Green's function method. In this work we analyze homogeneous cross-section arbitrarily-shaped waveguides. The electric and magnetic 3D-dyadic Green's functions of such waveguides are formulated in modal expansion and numerically solved for non-standard waveguides using the Integral Equation based method BI-RME. The convolution of the Green's function and the charges in motion, yields the electromagnetic field. In order to avoid the complex computation of the convolution operation, the original time-domain problem is transformed into the frequency-domain by means of a Fourier analysis. Finally, the fields are expressed back to the time- domain. This technique allows to study cases like a charge in constant velocity traveling through a uniform waveguide. This problem is of particular interest for accelerating structures and is analyzed in this work.

- M. J. Nogales, B. Gimeno, D. Raboso, S. Anza, A. Alvarez-Melcon, F. Quesada, V. Boria, C. Vicente, and J. Gil, "Multimodal characterization of the multipactor effect in microwave

waveguide components," *IEEE Microwave and Wireless Components Letters*, vol. 22, pp. 61–63, Feb 2012

Multipactor effect is a resonant avalanche of secondary electrons induced by an RF electromagnetic field, which endangers high-power payloads on satellites and particle accelerator structures. The main goal of this letter is to present a multimodal network characterization of a multipactor discharge occurring in a bounded waveguide region. This will allow to perform a rigorous analysis of a complete passive component considering the presence of a discharge. In order to verify the present formulation, we have measured the power spectrum generated by a multipactor event excited in a simple microwave circuit based on rectangular waveguides, which has been compared with the theoretical results, obtaining good agreement.

- M. J. Nogales, S. Marini, B. Gimeno, A. Alvarez-Melcon, V. Boria, P. S. Pacheco, S. Cogollos, and D. Raboso, "Evaluation of time-domain electromagnetic fields radiated by charged particles within an arbitrarily-shaped cross-section waveguide using frequency-domain Green's functions," *Radio Science*, 2012 (Pending publication)

  A technique for the accurate computation of the time-domain electromagnetic fields radiated by a charged distribution moving within an arbitrarily-shaped waveguide region is presented. Based on the transformation (by means of the standard Fourier analysis) of the time-varying current density of the analyzed problem to the frequency-domain, the resulting equivalent current is further convolutioned with the dyadic electric and magnetic Green's functions. Finally, frequency-domain electric and magnetic fields are transformed back to the time-domain, just obtaining the total fields radiated by the charged distribution. Furthermore, we present a method for the computation of the wakefields of arbitrary cross-section uniform waveguides from the resulting field expressions. Several examples of charged particles moving in the axial direction of such waveguides are included.

Bibliography

[1] W. Salah and J.-M. Dolique, "Wake field of electron beam accelerated in a RF-gun of free electron laser ELSA," *Nuclear Instr. Methods Phys. Res. A*, vol. 431, pp. 27–37, 1999. DOI 10.1016/S0168-9002(99)00255-7.

[2] W. Salah, "Analytical and numerical investigations of the evolution of wake fields of accelerated electron beams encountering cavity discontinuities in laser-driven RF-free electron laser photoinjector," *Nuclear Instr. Methods Phys. Res. A*, vol. 533, pp. 248–257, 2004. DOI 10.1016/j.nima.2004.05.129.

[3] P. B. Wilson, "Introduction to wakefields and wake potentials," in *Physics of Particle Accelerators*, 1989. DOI 10.1063/1.38045.

[4] H. Figueroa, W. Gai, R. Konecny, J. Norem, A. Ruggiero, P. Schoessow, and J. Simpson, "Direct measurement of beam-induced fields in accelerating structures," *Phys. Rev. Lett.*, vol. 60, pp. 2144–2147, 1988. DOI 10.1103/PhysRevLett.60.2144.

[5] K.-Y. Ng, "Wake fields in a dielectric-lined waveguide," *Phys. Rev. D*, vol. 42, pp. 1819–1828, 1990. DOI 10.1103/PhysRevD.42.1819.

[6] M. Rosing and W. Gai, "Longitudinal- and transverse-wake-field effects in dielectric structures," *Phys. Rev. D*, vol. 42, pp. 1829–1834, 1990. DOI 10.1103/PhysRevD.42.1829.

[7] S. H. Kim, K. W. Chen, and J. S. Yang, "Modal analysis of wake fields and its application to elliptical pillbox cavity with finite aperture," *J. Appl. Phys.*, vol. 68, pp. 4942–4952, 1990. DOI 10.1063/1.347079.

[8] W. Gai, A. Kanareykin, A. L. Kustov, and J. Simpson, "Numerical simulations of intense charged-particle beam propagation in a dielectric wake-field accelerator," *Phys. Rev. E*, vol. 55, pp. 3481–3488, 1997. DOI 10.1103/PhysRevE.55.3481.

[9] A. Burov and V. Danilov, "Suppression of transverse bunch instabilities by asymmetries in the chamber geometry," *Phys. Rev. Lett.*, vol. 82, pp. 2286–2289, 1999. DOI 10.1103/PhysRevLett.82.2286.

[10] V. Danilov, "Extended definitions of wake fields and their influence on beam dynamics," *Phys. Rev. Special Topics - Accel. Beams*, vol. 3, p. 014201, 2000. DOI 10.1103/PhysRevSTAB.3.014201.

[11] L. Xiao, W. Gai, and X. Sun, "Field analysis of a dielectric-loaded rectangular waveguide accelerating structure," *Phys. Rev. E*, vol. 65, p. 016505, 2001. DOI 10.1103/PhysRevE.65.016505.

[12] C. Jing, W. Liu, L. Xiao, W. Gai, and P. Schoessow, "Dipole-mode wakefields in dielectric-loaded rectangular waveguide accelerating structures," *Phys. Rev. E*, vol. 68, p. 016502, 2003. DOI 10.1103/PhysRevE.68.016502.

[13] M. Hess, C. S. Park, and D. Bolton, "Greens function based space-charge field solver for electron source simulations," *Phys. Rev. Special Topics - Accel. Beams*, vol. 10, p. 054201, 2007. DOI 10.1103/PhysRevSTAB.10.054201.

[14] G. Stupakov, K. L. F. Bane, and I. Zagorodnov, "Optical approximation in the theory of geometric impedance," *Phys. Rev. Special Topics - Accel. Beams*, vol. 10, p. 054401, 2007. DOI 10.1103/PhysRevSTAB.10.054401.

[15] A. J. Hatch and H. B. Williams, "Multipacting modes in high-frequency gaseous breakdown," *Phys. Rev.*, vol. 25, p. 417, 1954. DOI 10.1103/PhysRev.112.681.

[16] J. R. M. Vaughan, "Multipactor," *IEEE Trans. Electron Devices*, vol. 35, p. 1172, 1988. DOI 10.1063/1.3602080.

[17] S. Riyopoulos, "Multipactor saturation due to space-charge-induced debunching," *Phys. Plasmas*, vol. 4, p. 1448, 1997. DOI 10.1063/1.872319.

[18] R. Udiljak, D. Anderson, P. Ingvarson, U. Jordan, U. Jostell, L. Lapierre, G. Li, M. Lisak, J. Puech, and J. Sombrin, "New method for detection of multipaction," *IEEE Trans. Plasma Science*, vol. 31, p. 396, 2003. DOI 10.1109/TPS.2003.811646.

[19] C. Vicente, M. Mattes, D. Wolk, H. L. Hartnagel, J. R. Mosig, and D. Raboso, "Multipactor breakdown prediction in rectangular waveguide based components," in *Microw. Symp. Digest, 2005 IEEE MTT-S Int.*, vol. 2, p. 1055, Long Beach, California, USA, edited by Institute of Electrical and Electronics Engineers, IEEE, New-York, Jun. 12-17 2005. DOI 10.1109/MWSYM.2005.1516852.

[20] J. de Lara, F. Pérez, M. Alfonseca, L. Galán, I. Montero, E. Román, and D. Raboso, "Multipactor prediction for on-board spacecraft RF equipment with the MEST software tool," *IEEE Trans. Plasma Science*, vol. 34, p. 476, 2006. DOI 10.1109/TPS.2006.872450.

[21] G. Torregrosa, A. Coves, C. P. Vicente, A. M. Pérez, B. Gimeno, and V. E. Boria, "Time evolution of an electron discharge in a parallel-plate dielectric-loaded waveguide," *IEEE Electron Device Lett.*, vol. 27, p. 619, 2006. DOI 10.1109/LED.2006.877284.

[22] R. Udiljak, D. Anderson, M. Lisak, V. E. Semenov, and J. Puech, "Multipactor in a coaxial transmission line. I. analytical study," *Phys. Plasmas*, vol. 14, p. 033508, 2007. DOI 10.1063/1.2710464.

[23] V. E. Semenov, N. Zharova, R. Udiljak, D. Anderson, M. Lisak, and J. Puech, "Multipactor in rectangular waveguides," *Phys. Plasmas*, vol. 14, p. 033509, 2007. DOI 10.1063/1.2480678.

[24] S. Anza, C. Vicente, B. Gimeno, V. E. Boria, and J. Armendáriz, "Long-term multipactor discharge in multicarrier systems," *Phys. Plasmas*, vol. 14, p. 082112, 2007. DOI 10.1063/1.2768019.

[25] R. Udiljak, D. Anderson, M. Lisak, J. Puech, and V. E. Semenov, "Multipactor in a waveguide iris," *IEEE Trans. Plasma Science*, vol. 35, p. 388, 2007. DOI 10.1109/TPS.2007.892737.

[26] F. Zimmermann, "A Simulation Study of Electron-Cloud Instability and Beam-Induced Multipacting in the LHC. LHC Project Report 95," tech. rep., European Organization for Nuclear Research., 1997.

[27] O. Grobner, "Beam induced multipacting," in *Particle Accelerator Conference*, 1997. DOI 10.1109/PAC.1997.753283.

[28] R. Burton, M. Jong, and L. Funk, "Vacuum and multipactor performance of the hadron electron ring accelerator 52 MHz cavities," *Journal Vacuum Science Tech.*, vol. 9, p. 2081, 1991. DOI 10.1116/1.577417.

[29] S. Yamaguchi, "Trajectory simulation of multipactoring electrons in an S-band pillbox RF window," *IEEE Trans. Nuclear Sci.*, vol. 39, p. 278, 1992. DOI 10.1109/23.277497.

[30] R. Kishek and Y. Lau, "Interaction of multipactor discharge and RF circuit," *Phys. Rev. Lett.*, vol. 75, p. 1218, 1995. DOI 10.1103/PhysRevLett.75.1218.

[31] K. Primdahl, R. Kustom, and J. Maj, "Reduction of multipactor in RF ceramic windows using a simple titanium-vapor deposition system," in *Proc. Particle Acceler. Conf.*, vol. 3, (Dallas, TX, USA), p. 1687, IEEE, May 1996. DOI 10.1109/PAC.1995.505328.

[32] L.-K. Ang, Y. Y. Lau, R. A. Kishek, and R. M. Gilgenbach, "Power deposited on a dielectric by multipactor," *IEEE Trans. Plasma Science*, vol. 26, p. 290, 1998. DOI 10.1109/27.700756.

[33] R. Kishek, Y. Y. Lau, L. K. Ang, A. Valfells, and R. M. Gilgenbach, "Multipactor discharge on metals and dielectrics: Historical review and recent theories," *Phys. Plasmas*, vol. 5, p. 2120, 1998. DOI 10.1063/1.872883.

[34] R. L. Geng and H. S. Padamsee, "Exploring multipacting characteristics of a rectangular waveguide," in *Proc. Particle Accel. Conf.*, vol. 1, (New York, USA), p. 429, IEEE, Mar. 1999. DOI 10.1109/PAC.1999.795724.

[35] A. Neuber, D. Hemmert, H. Krompholz, L. Hatfield, and M. Kristiansen, "Initiation of high power microwave dielectric interface breakdown," *Journal Appl. Phys.*, vol. 86, p. 1724, 1999. DOI 10.1063/1.370953.

[36] E. Chojnacki, "Simulations of a multipactor-inhibited waveguide geometry," *Phys. Rev. Spec. Topics - Accel. Beams*, vol. 3, p. 032001, 2000. DOI 10.1103/PhysRevSTAB.3.032001.

[37] R. Cimino, I. R. Collins, M. A. Furman, M. Pivi, F. Ruggiero, G. Rumolo, and F. Zimmermann, "Can low-energy electrons affect high-energy physics accelerators?," *Phys. Rev. Letters*, vol. 39, p. 014801, 2004. DOI 10.1103/PhysRevLett.93.014801.

[38] T. Abe, T. Kageyama, K. Akai, K. Ebihara, H. Sakai, and Y. Takeuchi, "Multipactoring zone map of an RF input coupler and its application to high beam current storage rings," *Phys. Rev. Spec. Topics - Accel. Beams*, vol. 9, p. 062002, 2006. DOI 10.1103/PhysRevSTAB.9.062002.

[39] M. D. Deshpande, "Analysis of Discontinuities in a Rectangular Waveguide Using Dyadic Green's Function Approach in Conjunction With Method of Moments. NASA CR-201692," tech. rep., National Aeronautics and Space Administration, 1997.

[40] P. M. Slobodzian, A. A. Melcón, T. M. Grzegorczyk, and F. E. Gardiol, "Green's functions for vertical current sources embedded in uniform waveguide or cavities filled with multilayered media," *Microwave and Optical Technologies Letters*, vol. 33, pp. 186–191, 2002. DOI 10.1002/mop.10272.

[41] Y. Rahmat-Samii, "On the question of computation of the dyadic Green's function at the source region in waveguides and cavities," *IEEE. Trans. on Microwave Theory and Techniques*, vol. 23, pp. 762–765, 1975. DOI 10.1109/TMTT.1975.1128671.

[42] C.-T. Tai, *Dyadic Green Functions in Electromagnetic Theory.* IEEE Press, 1993. ISBN 978-0780304499.

[43] R. E. Jogerson and R. Mittra, "Efficient calculation of the free-space periodic Green's function," *IEEE Trans. Antennas and Propagation*, vol. 38, pp. 633–642, 1990. DOI 10.1109/8.53491.

[44] A. A. Melcon and J. R. Mosig, "Two techniques for the efficient numerical calculation of the Green's functions for planar shielded circuits and antennas," *IEEE Transactions on Microwave Theory and Techniques*, vol. 48, pp. 1492–1504, September 2000. DOI 10.1109/22.869000.

[45] G. Conciauro, M. Guglielmi, and R. Sorrentino, *Advanced Modal Analysis - CAD Techniques for Waveguide Components and Filters.* John Wiley & Sons, Ltd., 2000. ISBN 0-471-97069-7.

[46] N. M. Leopold B. Felsen, *Radiation and Scattering of Waves.* IEEE Press, 1994. ISBN 978-0780310889.

[47] R. E. Collin, *Field Theory of Guided Waves.* IEEE Press, 1991. ISBN 978-0879422370.

[48] D. M. Pozar, *Microwave Engineering.* John Wiley & Sons, Ltd., 2005. ISBN 978-0470631553.

[49] R. F. Harrington, *Time-harmonic electromagnetic fields.* McGraw-Hill Book Company, Inc., 1961. ISBN 978-0471208068.

[50] G. W. Hanson and A. B. Yakovlev, *Operator theory for electromagnetics.* Springer-Verlag New York, Inc., 2002. ISBN 978-0387952789.

[51] R. Woo and A. Ishumaru, "A Similarity Principle for Multipacting Discharges," *Applied Physics*, vol. 38, pp. 5240–5244, 1967. 10.1063/1.1709307.

[52] A. Woode and J. Petit, "Diagnostic Investigations into the Multipactor Effect, Susceptibility Zone Measurements and Parameters affecting a Discharge. ESTEC Working Paper No. 1556," tech. rep., ESA/ESTEC, Noordwijk (Netherlands), 1989.

[53] A. J. Hatch and H. B. Williams, "The secondary electron resonance mechanism of low-pressure high-frequency gas breakdown," *Applied Physics*, vol. 112, p. 681, 1958. DOI 10.1063/1.1721656.

[54] A. R. Nyaiesh, E. L. Garwin, F. K. King, and R. E. Kirby, "Properties of thin antimultipactor TiN and Cr2O3 coatings for klystron windows," *Vacuum Sc. and Tech. A*, vol. 4, p. 2356, 1986. DOI 10.1116/1.574076.

[55] N. Diaz, S.Castaneda, J. M. Ripalda, I. Montero, L. Galan, S. Feltham, D.Raboso, and F.Rueda, "Materials of low secondary electron emission to prevent the multipactor effect in high-power RF devices in space," in *6th Spacecraft Charging Technology Conference*, September 2000.

[56] J. Sombrin, "Effect Multipactor. Technical Report No.83/DRT/TIT/HY/119/T," tech. rep., CNES, Toulouse (France), 1983.

[57] A. Kryazhev, M. Buyanova, V. Semenov, D. Anderson, M. Lisak, J. Puech, L. Lapierre, and J. Sombrin, "Hybrid resonant modes of two-sided multipactor and transition to the polyphase regime," *Phys. Plasmas*, vol. 9, p. 4736, 2002. DOI 10.1063/1.1514969.

[58] "ECSS-E-20-01A. multipaction design and test. ECSS sectretariat, ESA-ESTEC, requirements & standards division." Website. `http://www.ecss.nl/`.

[59] E. Sorolla, S. Anza, B. Gimeno, A. M. Pérez, C. Vicente, J. Gil, F. J. Pérez-Soler, F. D. Quesada, A. Álvarez, and V. E. Boria, "An analyitical model to evaluate the radiated power spectrum of a multipactor discharge in a parallel-plate region," *IEEE Trans. Electron Devices*, vol. 55, p. 2252, 2008. DOI 10.1109/TED.2008.926271.

[60] C. Phillips, A. Woode, and P. Woodhouse, "A multipactor investigation program at C-band. ESTEC Working Paper No. 1412," tech. rep., ESA/ESTEC, Noordwijk (Netherlands), 1985.

[61] M. A. Kasha, *The ionosphere and its interaction with satellites*. New York: Gordon and Breach, Science Publishers, 1969. ISBN 978-0677020907.

[62] D. Raboso, A. Allstaff, C. Miquel-Espanya, and B. Gimeno, "Photoemission from UV sources: An alternative multipactor trigger for ground testing," in *6th International Workshop on Multipactor, Corona and Passive Intermodulation in Space RF Hardware*, September 2008.

[63] S. Anza, C. Vicente, D. Raboso, J. Gil, B. Gimeno, and V. E. Boria, "Enhanced Prediction of Multipaction Breakdown in Passive Waveguide Components including Space Charge Effects," in *Microw. Symp. Digest, 2008 IEEE MTT-S Int.*, vol. 2, p. 1095, Atlanta, Georgia, USA, edited by Institute of Electrical and Electronics Engineers, IEEE, New-York, Jun. 15-20 2008. DOI 10.1109/MWSYM.2008.4633247.

[64] M. Jiménez, B. Gimeno, C. Miquel-Espanya, D. Raboso, S. Anza, C. Vicente, J. Gil, F. Quesada, A. Alvarez, M. Taroncher, M. Reglero, and V. E. Boria, "Analysis of the electromagnetic radiation generated by a multipactor discharge occurring within a microwave passive component," *Phys. D: Appl. Phys*, vol. 43, p. 395501, 2010. DOI 10.1088/0022-3727/43/39/395501.

[65] R. Sorrentino and G. Bianchi, *Microwave and RF Engineering*. John Wiley & Sons, Ltd., 2010. ISBN 978-0470758625.

[66] P. Eskelinen, *Introduction to RF Equipment and System Design*. Artech House, Inc., 2004. ISBN 978-1580536653.

[67] "FEST3D software." Website. `http://www.fest3d.com/`, provided by `http://www.aurorasat.es/`.

[68] T. P. Wangler, *RF Linear Accelerators*. Wiley-VCH, 2008. ISBN 978-0471168140.

[69] M. Reiser, *Theory and Design of Charged Particle Beams*. Wiley-VCH, 2004. ISBN 978-0471306160.

[70] B. W. Zotter and S. A. Kheifets, *Impedances and wakes in high-energy particle accelerators*. World Scientific, 1998. ISBN 978-9810226268.

[71] K. Yokoya, "Resistive wall impedance of beam pipes of general cross section," *Physics Journal at Particle Accelerators*, vol. 41, pp. 221–248, 1993.

[72] D. J. Griffiths, *Introduction to Electrodynamics*. Prentice Hall, 1999. ISBN 978-0138053260.

[73] J. D. Jackson, *Classical electrodynamics*. John Wiley and Sons, Inc., 1999. ISBN 978-0471309321.

[74] S. Cogollos, S. Marini, V. E. Boria, P. Soto, A. Vidal, H. Esteban, J. V. Morro, and B. Gimeno, "Efficient modal analysis of arbitrarily shaped waveguides composed of linear, circular, and elliptical arcs using the BI-RME method," *IEEE Trans. Microwave Theory Tech.*, vol. 51, p. 2378, 2003. DOI 10.1109/TMTT.2003.819776.

[75] G. Conciauro, M. Bressan, and C. Zuffada, "Waveguide modes via an integral equation leading to a linear matrix eigenvalue problem," *IEEE Trans. Microwave Theory Tech.*, vol. 32, p. 1495, 1984. DOI 10.1109/TMTT.1985.1133143.

[76] R. F. Harrington, *Field Computation by Moment Methods*. IEEE/OUP Press Series on Electromagnetic Waves, IEEE Press: Oxford University Press, 1993. ISBN 978-0780310148.

[77] A. Lutman, R. Vescoso, and P. Craievich, "Electromagnetic field and short-range wake function in a beam pipe of elliptical cross-section," *Phys. Rev. Spec. Topics - Accel. Beams*, vol. 11, p. 074401, 2008. DOI 10.1103/PhysRevSTAB.11.074401.

[78] M. Bassetti and G. A. Erskine, "Closed expression for the electrical field of a two-dimensional Gaussian charge," 1980. DOI 10.1.1.39.5863.

[79] M. Abramowitz and I. Stegun, *Handbook of Mathematical functions with Formulas, Graphs, and Mathematical Tables*. Dover Publications, 1970. ISBN 978-0486612720.

[80] U. Iriso-Ariz, F. Caspers, and A. Mostacci, "Evaluation of the horizontal to vertical transverse impedance ratio for LHC beam screen using a 2D electrostatic code," *Proc. Particle Acceler. Conf.*, p. 3480, 2003. DOI 10.1109/PAC.2003.1289954.

[81] T. K. F. Caspers, "Waveguide mode reflectometry for obstacle detection in the LHC beam pipe including signal attenuation," in *Proc. Particle Acceler. Conf.*, IEEE, 2003. DOI 10.1109/PAC.2003.1289235.

[82] I. S. Gradshteyn and I. M. Ryzhik, *Table of Integrals, Series, and Products*. Academic Press, 1980.

[83] P. Young, "Singular Fourier transforms and the integral representation of the Dirac delta function," tech. rep., University of California Santa Cruz, 1997.

[84] "Mathematica 8." Website. `http://www.wolfram.com/mathematica/`, provided by `http://www.wolfram.com/`.

[85] M. F. J. Nogales, J. P. Garcia, J. Hinojosa, and A. A. Melcon, "Genetic algorithms applied to microwave filters optimization and design," in *Progress in Electromagnetic Research Symposium, PIERS Proceedings*, (Cambridge, MA, USA), pp. 99–103, July 2008.

[86] F. J. P. Soler, S. Anza, M. Mattes, C. Miquel, F. Quesada, M. Jiménez, J. Gil, C. Vicente, J. R. Mosig, D. Raboso, V. E. Boria, B. Gimeno, and A. Alvarez-Melcon, "Rigorous investigation of RF breakdown effects in high power microstrip passive circuits," in *IEEE International Microwave Symposium, Proceedings of the IEEE, MTT-S*, (Boston, MA, USA), pp. 833–836, June 2009. DOI 10.1109/MWSYM.2009.5165826.

[87] J. P. Soler, M. J. Nogales, F. Q. Pereira, and A. A. Melcon, "A novel approach for the evaluation of electromagnetic fields using rigorous wire antenna models," in *IEEE International Symposium on Antennas and Propagation, Proceedings of the IEEE, AP-S*, (Charleston, SC, USA), pp. 1–4, June 2009. DOI 10.1109/APS.2009.5172023.

[88] B. Gimeno, S. Anza, F. P. Soler, C. Vicente, J. Gil, V. Boria, F. Quesada, M. Jiménez, A. A. Melcon, M. Mattes, J. Mosig, D. Raboso, and C. M. Espana, "Estudio del efecto multipactor en componentes pasivos de microondas para aplicaciones en comunicaciones espaciales," in *VII Encuentro Iberico de Electromagnetismo Computacional*, (Caceres, Spain), May 2010.

[89] M. Jiménez, B. Gimeno, S. Anza, C. Vicente, J. Gil, A. A. Melcon, F. Quesada, M. Taroncher, M. Reglero, and D. Raboso, "Computation of a multipactor discharge occuring within a realistic passive microwave component," in *7th International Workshop on Multipaction, Corona and Passive Intermodulation in Space RF Hardware, European Space Agency, MULCOPIM'11*, (Valencia, Spain), September 2011.

[90] M. Jiménez, S. Marini, B. Gimeno, A. A. Melcon, F. Quesada, V. Boria, P. Soto, S. Cogollos, and D. Raboso, "Computation of wakefields in arbitrarily cross-shaped waveguide for particle accelerator applications," in *7th International Workshop on Multipaction, Corona and Passive Intermodulation in Space RF Hardware, European Space Agency, MULCOPIM'11*, (Valencia, Spain), September 2011.

[91] M. J. Nogales, B. Gimeno, D. Raboso, S. Anza, A. Alvarez-Melcon, F. Quesada, V. Boria, C. Vicente, and J. Gil, "Multimodal characterization of the multipactor effect in microwave waveguide components," *IEEE Microwave and Wireless Components Letters*, vol. 22, pp. 61–63, Feb 2012.

[92] M. J. Nogales, S. Marini, B. Gimeno, A. Alvarez-Melcon, V. Boria, P. S. Pacheco, S. Cogollos, and D. Raboso, "Evaluation of time-domain electromagnetic fields radiated by charged particles within an arbitrarily-shaped cross-section waveguide using frequency-domain Green's functions," *Radio Science*, 2012.